Templated self-assembly of siloxane block copolymers for nanofabrication

by

Yeon Sik Jung

B.S., Materials Science and Engineering, 1999
M.S., Materials Science and Engineering, 2001
Korea Advanced Institute of Science and Technology, Daejeon, Korea

Submitted to the DEPARTMENT OF MATERIALS SCIENCE AND ENGINEERING
in Partial Fulfillment of the Requirements for the Degree of

DOCTOR OF PHILOSOPHY IN MATERIALS SCIENCE AND ENGINEERING
at the
MASSACHUSETTS INSTITUTE OF TECHNOLOGY
June 2009

Signature of Author : ....
Department of Materials Science and Engineering
May 5th, 2009

Certified by :...
Caroline A. Ross
Toyota Professor of Materials Science and Engineering
Thesis Advisor

Approved by :...
Christine Ortiz
Chair, Departmental Committee on Graduate Students

Self-assembled block copolymers for nanofabrication

By Yeon Sik Jung

Submitted to the Department of Materials Science and Engineering
on May 5, 2009 in Partial Fulfillment of the Requirements for the
Degree of Doctor of Philosophy in Materials Science and Engineering

Abstract

Monolayer patterns of block copolymer (BCP) microdomains have been pursued for applications in below sub-30 nm nanolithography. BCP self-assembly processing is scalable and low cost, and is well-suited for integration with existing semiconductor fabrication techniques. The two critical issues are how to obtain reliable long-range ordering of features with minimum defect densities and how to successfully transfer the patterns into other functional materials.

Exceptionally well-ordered and robust nanoscale patterns can be made from poly(styrene-b-dimethylsiloxane) (PS-PDMS) BCPs, which have a very large Flory-Huggins interaction parameter between the blocks compared to other commonly used BCPs. Cylinder- or sphere-forming BCP films were spin-coated over silicon substrates patterned with shallow steps using optical lithography or nanoscale posts made by electron-beam lithography, and solvent-annealed to induce ordering. This generates patterns with a correlation length of at least several micrometers. The annealed film was treated with plasma to obtain oxidized PDMS patterns with a lateral dimension of 14 - 18 nm. These can be used as an etch mask or an easily removable template for patterning functional materials.

Solvent vapor treatments can tune the pattern dimension and morphology. Different degrees of solvent uptake in BCP films during solvent-annealing can manipulate the interfacial interaction between the two blocks, and a mixed solvent vapor can change the effective volume fraction of each block. The self-assembled patterns can be transferred into various kinds of functional materials. For example, arrays of parallel lines were used as a mask to pattern poly(3,4-ethylenedioxythiophene):poly(styrenesulfonate) (PEDOT:PSS) conducting polymer thin films. The resulting PEDOT:PSS nanowire array was used as an chemiresistive-type ethanol-sensing device. Metallic films such as Ti, Pt, Ta, W, and magnetic Co and Ni were structured using a pattern-reversal process. Coercivity enhancements were observed for the fabricated ferromagnetic nanostructures such as wires, rings, and antidots. These functional nanostructures can be utilized for a variety of devices such as high-density and high performance sensor or memory devices.

Thesis Supervisor: Caroline A. Ross
Title: Toyota Professor of Materials Science and Engineering

Table of Contents

Abstract 2
Table of Contents 3
List of Figure Captions 5
Acknowledgements 10

Chapter 1 Introduction

1.1 Overview and contents 12
1.2 Nonconventional nanofabrication techniques 16
    1.2.1 Imprinting techniques 17
    1.2.2 Scanning-probe-based nanolithography 19
1.3 Self-assembly of block copolymers 21
    1.3.1 Introduction 21
    1.3.2 Phase behavior of block copolymers 22
    1.3.3 Block copolymer micelles 26
1.4 Magnetic nanostructures and devices 28
1.5 Chemical sensors 32

Chapter 2 Self-assembled pattern-generation of lines using a cylindrical block copolymer

2.1 Introduction 38
2.2 Experimental 41
2.3 Thin film structure of a PS-PDMS block copolymer and two-step reactive ion etching 42
2.4 Effect of brush treatments on morphology 43
2.5 Effects of solvent-annealing conditions and template patterns 45
2.6 Summary 50

Chapter 3 Solvent vapor induced tunability of self-assembled block copolymer patterns

3.1 Introduction 54
3.2 Experimental 56
3.3 Effect of solvent vapor pressure 57
3.4 Effects of mixed solvent vapors 62
3.5 Summary 70

Chapter 4 Conductive polymer nanowires for gas sensor applications

4.1 Introduction 74
4.2 Experimental 75

4.3 Patterning polymers using block copolymer etch masks 78
4.4 Ethanol vapor sensor measurement 84
4.5 Summary 88

Chapter 5 Formation of concentric ring patterns by circular confinement

5.1 Introduction 94
5.2 Experimental 95
5.3 Formation of ring patterns induced by circular confinement 97
5.4 Analyses and modeling on concentric ring patterns 100
5.5 Summary 109

Chapter 6 Self-assembled pattern-generation of dots using a spherical block copolymer

6.1 Introduction 114
6.2 Experimental 115
6.3 1D templates to guide 0D self-assembling patterns 117
6.4 Sparse 0D templates to guide 0D self-assembling patterns 118
6.5 Effects of commensurability on the orientation 122
6.6 Analyses on the orientational relationship 125
6.7 Summary 128

Chapter 7 Fabrication of metallic nanostructures and characterizations

7.1 Introduction 133
7.2 Experimental 136
7.3 Fabrication of metallic nanowires and characterization 137
7.4 Fabrication of nanoporous metallic films and characterization 142
7.5 Fabrication of magnetic ring patterns and characterization 150
7.6 Summary 155

Chapter 8 Conclusions and future works

8.1 Conclusions 160
8.2 Future work 162
    8.2.1 Cross-point memory devices 162
    8.2.2 Nanochannel structures 163
    8.2.3 Metal oxide nanowire sensors 164
    8.2.4 Patterned magnetic media 164
    8.2.5 Remaining challenges in block copolymer pattern formation 165

Publications 170

List of Figure Captions

Figure 1-1 Possible configuration of (a) thermal and (b) UV nanoimprinting. (c) structures patterned by nanoimprinting lithography. (d) Schematic of mold fabrication and pattern multiplication. 19

Figure 1-1 Schematics of (a) local oxidation nanolithography by an AFM tip and (b) dip-pen nanolithography. 20

Figure 1-3 Microphase separation of block copolymers. 22

Figure 1-4 Phase-diagrams of diblock copolymers (a) predicted by self - consistent mean field theory and (b) obtained experimentally. 23

Figure 1-5 Various morphologies of diblock copolymers with a different minority volume fractions. 24

Figure 1-6 Structures and orientations of block copolymer thin films with different thicknesses. The cases of (a) large and (b) little asymmetries in interfacial energy. 26

Figure 1-7 Schematics of block copolymer micelles: (i) direct micelles, (ii) vesicles, and (iii) other morphologies: (iiia) inverse micelles, (iiib) lamellar structures, and (iiic) cylindrical or tubular micelles. 28

Figure 1-8 8 Schematic diagrams of the magnetization states in ferromagnetic thin film rings. (a) Saturated state, (b) onion-state, and (c) vortex-state. 31

Figure 1-9 Band bending of nanostructured oxide materials by adsorption of oxidizing and reducing gases. (Left) A summary of a few of the electronic, chemical, and optical processes occurring on metal oxides. (Right) 32

Figure 2-1 Comparison of Flory-Huggins χ-parameters for common diblock copolymers. 39

Figure 2-2 Schematic cross-section diagram of a film of PS-PDMS on a PDMS-brush-treated silica surface. A layer of PDMS is present at the air-film interface, and below it a layer of parallel cylinders. 42

Figure 2-3 SEM images of PS-PDMS thin film after (a) exposure to an O2 plasma for 1 min; (b) exposure to a CF4 plasma (5 sec) followed by an O2 plasma (1 min.). 43

Figure 2-4 SEM images of PS-PDMS on trench substrates (a) without a brush, (b) with a PS-brush, and (c) with a PDMS brush. The samples were solvent-annealed for 15 hrs. 44

Figure 2-5 Arrangement of cylinders as a function of mesa/trench width ratio and solvent vapor pressure for (a) t_{anneal} = 4 hours and (b) t_{anneal} = 15 hours. For condition Cβ in (b), both perpendicular and mixed orientations were observed. 46

Figure 2-6 SEM images of (a), (b), (c) parallel cylinders on trench substrates with narrow mesas (W_{mesa}=125nm and W_{trench}=875nm) under a high vapor pressure of toluene (condition Eα from Figure 2-5) and (d) perpendicular cylinders in a wide-mesa pattern (W_{mesa}=270 nm and W_{trench}=730 nm) at a lower vapor pressure (condition Bβ). The annealing time was 15 hours. 48

Figure 2-7 SEM images of cylinders guided by 7μm-wide trenches. 49

Figure 2-8 Grazing incidence small-angle X-ray scattering patterns of cylinders. 50

Figure 3-1 Scanning electron micrographs of the cylinder-forming PS-PDMS block copolymer after solvent-annealing and reactive ion etching to remove PS. Linear patterns with various period and linewidth were obtained with different toluene vapor pressure conditions. The solvent vapor pressure was varied by changing the ratio of solvent surface area (S) to the annealing chamber volume (V). The S/V ratios are (b) 0.571, (c) 0.601, (d) 0.619, and (e) 0.968 cm^{-1}, respectively. 58
Figure 3-2 Measured period, fill factor, and linewidth of each pattern as a function of S/V. 59
Figure 3-3 Calculated free energy curves with different χ parameters. The inset shows the change of equilibrium domain spacing with χ. 61
Figure 3-4 Evolution of morphologies obtained depending on the toluene (T) and heptane (H) ratio. The T/H volume ratios are (a) 6, (b) 3, (c) 2.5, (d) 2, (e) 1.5, (f) 1.35, (g) 1.25, and (h) 1. 64
Figure 3-5 Measured period, fill factor, and linewidth of patterns obtained with different toluene (T) and heptane (H) mixing ratios. The volume fraction of toluene was calculated as T/(T+H). 65
Figure 3-6 A phase diagram of morphologies obtained with various solvent mixing ratios and vapor pressure. A perforated lamellar structure was obtained at T/H = 2. 66
Figure 3-7 Perforated lamellar morphologies annealed at various vapor pressures. The S/V ratios are (a) 0.571, (b) 0.585, (c) 0.601, (d) 0.619, (e) 0.704, and (f) 0.968, respectively. The insets show fast Fourier transforms. The best ordering was obtained with S/V = 0.585 ~ 0.601 cm^{-1}. 68
Figure 3-8 A lower magnification image of perforated lamellar morphology at S/V = 0.585. 69
Figure 3-9 Histograms of pore diameters (31.7 ± 2.1 nm) and periodicity (44.8 ± 3.1). 70

Figure 4-1 Procedure for polymer nanowire fabrication. An aqueous PEDOT:PSS solution was spin-coated on a substrate patterned with a 1.3 μm period grating, then coated with a thin SiO_2 layer and a PDMS homopolymer brush. A PS-PDMS block copolymer thin film was then spin-coated and solvent-annealed. The self-assembled block copolymer patterns were transferred into the underlying PEDOT:PSS film through a series of reactive ion etching steps employing CF_4 and O_2 plasmas. 79
Figure 4-2 2 (a) Self-assembled cylinders on a BarLi® film. (After removing PS) (b), (c), and (d) after O_2 reactive ion etching using the cylinders as an etch mask. 81
Figure 4-3 Self-assembled cylinders on a PEDOT:PSS film. (After removing PS) The scale bars are 200 nm. 82
Figure 4-4 PEDOT:PSS nanowires after 30 sec, 50W, O_2/He reactive ion etching, using the self-assembled PDMS patterns as an etch mask. The remaining PDMS and thin oxide interlayer were removed with an additional CF_4 plasma treatment. 83
Figure 4-5 Schematic (not to scale) of a chemiresistor for ethanol vapor detector based on PEDOT:PSS nanowires. 50 nm thick Au electrodes, 1 mm apart, are formed perpendicular to the nanowires. The linear current-voltage relationship is also demonstrated. 84
Figure 4-6 (a) The resistance change of the polymer nanowires upon exposure to ethanol vapor. (b) Comparison of the response ($\Delta R/R_o$) of the nanowire array compared to that of thin films of three different thicknesses (14, 19, and 37 nm). 86

Figure 4-7 (a) Thermodynamic and (b) kinetic models to explain the enhancement of sensitivity as a function of surface-to-volume ratio 88

Figure 5-1 Circular trench patterns fabricated by interference lithography. 96
Figure 5-2 Morphology of the self-assembled PS-PDMS block copolymer after exposure to a CF_4 plasma (5 s) followed by an O_2 plasma (30 s). Scanning electron micrograph of concentric PDMS ring patterns (light contrast) in an array of 250 nm (top) and 170 nm (bottom) diameter circular pits. 99
Figure 5-3 Concentric ring patterns in templates with various confinement diameters C. The ratio C/L_{eq} was varied from 1.7 to 10. For some diameters, the innermost feature is a PDMS sphere (light contrast) and for others a smaller PS sphere (dark) is formed. The scale bar represents 100 nm. 101
Figure 5-4 The number of concentric rings in a template as a function of its diameter, C. Stars indicate patterns with a central PDMS sphere while solid circles indicate patterns with a central PS sphere. 102
Figure 5-5 The definition of the period P_n and outer diameter D_n of the concentric ring patterns. Here $P_n = [D_n-D_{n-1}]/2$ or for the inner spheres, $P_0=D_0/2$. 103
Figure 5-6 The outer diameter D_n of each PDMS ring as a function of confinement diameter C. 103
Figure 5-7 (a) The spacing P_n of each ring as a function of confinement diameter C. For the inner sphere, the radius is plotted. (b) The amplitude of variation ($P_{max}(n)$-$P_{min}(n)$) and the average P_n for each circular ring. 104
Figure 5-8 Free energy curves based on eq. (1). Bending energy is not considered here. 106
Figure 5-9 Bending energy and total energy as a function of the radius of curvature (R_c). 108
Figure 5-10 Calculated equilibrium spacing λ_{eq} normalized by its value at large R_c, and measured ring spacing normalized by L_{eq}, as a function of R_c. 109

Figure 6-1 SEM images of self-assembled block copolymer patterns after reactive ion etching. The oxygen plasma selectively removes the PS matrix block and oxidizes the PDMS spheres. The upper inset shows the fast Fourier transform (FFT) of (b). 118
Figure 6-2 Scanning-electron micrograph (SEM) of a disordered monolayer of BCP spherical domains formed on a flat surface, i.e. without templating. The boundaries between different grain orientations are indicated with dashed lines. The inset is a two-dimensional (2D) Fourier transform of the domain positions which shows the absence of long range order. 119
Figure 6-3 Schematic of the 0D post arrays to guide block copolymer spheres. 120
Figure 6-4 HSQ post arrays patterned with electron beam lithography. 121
Figure 6-5 SEM images of ordered BCP spheres formed within a sparse 2D lattice of HSQ posts (brighter dots). The substrate and post surfaces were functionalized with a PDMS brush layer (left), which corresponds to the schematic in Figure 6-3, and with a PS brush layer (right). The insets show the 2D Fourier transforms in which the high frequency components originate from the post lattice. 122

Figure 6-6 Plan-view SEM images of all the commensurate configurations for the L_{post}/L_o ratio range of 1.65 to 4.6. The white arrows show the orientation angle between the BCP microdomain lattice and the post lattice and are 120-nm long. The brighter dots are the oxidized HSQ posts, while the darker dots correspond to oxidized PDMS spherical domains. The blue and red arrows indicate the basis vectors of the BCP microdomain lattice, and sum to one horizontal basis vector of the post lattice. 124
Figure 6-7 Calculated orientations at which the BCP microdomain lattice is commensurate with the post lattice, as a function of L_{post}/L_o. The BCP lattice is commensurate with the post lattice when the post lattice basis vectors of length L_{post} can be represented as integer multiples, $<ij>$, of the BCP lattice basis vectors of length L_o. Due to the 6-fold symmetry of the BCP lattice, the angular span of 0 to 30° is sufficient to represent all possible non-degenerate orientations. 125
Figure 6-8 (A) Calculated curves of free energy per BCP chain vs L_{post}/L_0 for each commensurate configuration. Free energy minima occur at L_{post}/L_0 values where the commensurate condition is satisfied without straining the BCP microdomain array. (B) Experimental results showing the area fraction of each $\langle i\,j \rangle$ lattice vs L_{post}/L_0. Each filled circle is a data point obtained by image processing of an SEM image of a 1.3 cm by 1.3 cm square area of the templated region. This plot was generated from data collected from over 200 images of different post lattices on the same substrate. The solid lines connect the average values of the data points for a given L_{post}/L_0. 128

Figure 7-1 A pattern-reversal process to fabricate metallic nanowires. (A) Self-assembly of a cylinder-forming block copolymer, (B) two-step reactive ion etching to reveal oxidized PDMS line patterns, (C) metal deposition by sputtering, (D) CF_4 plasma etching, and (E) metallic nanowires with the reverse image of the original PDMS patterns. 137
Figure 7-2 An example of metal patterning. SEM images of (a), (b) W deposited on the oxidized PDMS patterns, (c) smoothened W surface by CF_4 plasma etching, and (d) W nanowires. 139
Figure 7-3 Various metallic nanowires fabricated with the pattern-reversal technique. 140
Figure 7-4 Grazing incidence small-angle X-ray scattering patterns of Pt nanowires. 141
Figure 7-5 Magnetic hysteresys curves of a flat Ni film and Ni nanowires. 142
Figure 7-6 Schematic representation of the fabrication process. (a) The chemical structure of the PS-PDMS block copolymer, (b) a lithographically-patterned trench, (c) a spin-coated block copolymer film in the trench, (d) well-ordered block copolymer microdomain array after solvent-annealing, (e) an array of oxidized PDMS dots after CF_4 and O_2 reactive ion etching processes, (f) a metal film deposited on the dot array, and (g) a porous metallic film after a high power CF_4 plasma etching. The porous film can be used for Ni dot fabrication by employing a second pattern-reversal step. (h) Ni film deposition and (g) a high power CF_4 plasma etching reveals the Ni dot array. 143

Figure 7-7 SEM images of (a), (b) a Pt thin film sputter-deposited on oxidized PDMS spheres, (c) smoothed surface of the Pt after a high power CF_4 plasma treatment, (d) various metallic thin films with nanopores after the selective removal of the PDMS template, (e) Ti nanowire patterns, (f) a nanoporous Ni film on SiO_2, (g) patterned SiO_2 via CF_4 reactive ion etching and Ni wet-etching, and (h) a Ni dot array. 144
Figure 7-8 The magnetic hysteresis loops of a Co antidot pattern. 146
Figure 7-9 SEM images of (a) a nanoporous Ni film on SiO2 and (b) patterned SiO2 via CF4 reactive ion etching and Ni wet-etching. 147
Figure 7-10 (a) An SEM image and (b) the magnetic hysteresis loops of Ni dots. 148
Figure 7-11 Size histograms of PDMS dots, pores formed in Ti and SiO_2, and Ni dots. 149
Figure 7-12 Cobalt double ring fabrication process (a) Fabrication of circular trench templates using interference lithography. (b) Self-assembly of ring patterns in the trenches and reactive ion etching to generate oxidized PDMS ring arrays. (c Sputter deposition of a Co thin film (thickness = 70nm). (d) Dry etching with 450W CF4 plasma. Initially the Co film is sputter-etched slowly by incident CF_x^+ ions, then the exposed oxidized PDMS patterns are rapidly removed through a chemical etching process. Consequently, the Co ring features form a reverse image of the original PDMS patterns. 151
Figure 7-13 Pattern transfer into a ferromagnetic film. (a) SEM image of an array of Co double rings. (b) measured and (c) simulated normalized magnetic hysteresis loops (M/Ms) of the double rings. The two rings in each structure are magnetostatically coupled, and the slanted plateau results from the formation of a distorted 'vortex' state. 152
Figure 7-14 Micromagnetic simulation results for double ring and two separate single rings with different sizes. The rings in the right, middle, and left correspond to three different magnetization states achieved by varying the magnetic field from +0.5 kOe to -0.5 kOe. Asymmetric vortex states (illustrated by the rings in the middle) are formed as intermediate states between the onion and reverse onion states. 154

Figure 8-1 An imaginary circuit layout composed of self-assembled BCP patterns. 167

Acknowledgement

More than twenty years ago, I was a quiet boy with a dream to be a writer. As expected, one of my enjoyments was to read every page of newspapers. One day, I could not take my eyes off a picture of a building with a white dome since it looked amazingly beautiful to me. That was the first moment of my meeting with MIT, even though, at that time, I was not even aware of what it stood for, and just thought it is was somewhere nice. Two decades later, I somehow became an engineering student of the school and wrote my PhD thesis, and this page is a piece of it. This memory is one reason that sometimes makes me believe in destiny.

The great majority of what I have accomplished, experienced, and learned throughout my PhD study have benefited from invaluable contributions by my wonderful supporters. Thanks to their help and support, I could spend four years of amazingly sweet time full of excitement and enthusiasm here at MIT.

First of all, I am deeply grateful to my supervisor, Professor Caroline Ross. What she has done for me has reminded me of The Giving Tree. Her encouraging and personal guidance and care made me develop and grow to be a more mature and independent researcher. She always respected my ideas – even insignificant ones, which gave me more confidence and energy to work. I believe we were a very nice team.

I would like to express my deep and sincere gratitude to my thesis committee, Prof. Ned Thomas, Prof. Harry Tuller, and Prof. Karl Berggren. Before coming to MIT, it was my dream to receive guidance from such world-renowned scholars. I had unusual opportunities to work closely together with all of them.

I also had excellent collaborators. I warmly thank Joel Yang for our productive collaboration and friendship. I am thankful to Woochul Jung and Dr. Eric Verploegen for their support for measurements.

I am grateful to Filip Ilievski and Vivian Chuang, who helped me start my research by letting me know important lab techniques. I owe my gratitude to Dr. Wonjoon Jung for being a great mentor and teaching me about magnetic devices. I also would like to show my appreciation to other Ross group members –Chunghee Nam, David Otero, Carlos Garcia, Lei Bi, Mark Mascaro, and Ms. Gabrielle Joseph.

This thesis might not have been possible without utilizing the excellent facilities of the NanoStructures Laboratory. Every day, I could conveniently process and image my samples, which significantly accelerated my progress. I thank Mr. Jim Daley and the other staff members for their help and support.

I would also like to give my thanks to my friends at MIT and in the Boston area, although I cannot name them one by one. I have unforgettable memories of time here with them.

I am grateful to my former advisor Prof. Duk Young Jeon at KAIST for his sincere support, guidance, and advice for my studies and career development. I also appreciate the support from Dr. Won-Kook Choi at KIST, who upgraded my ability as a researcher and helped me apply for PhD programs.

I would like to express my respect, love, and thanks to my family – grandparents, parents, and my brother Sung Sik. Finally, last but foremost, I thank my cute and lovely wife, Eun Hee for her understanding and encouragements.

"This thesis is dedicated to my family."
May 4th, 2009
Yeon Sik Jung

Chapter 1

Introduction

1.1 Overview and contents

Mother Nature uses a process called "self-assembly" to create extremely complex and diverse living systems such as human beings. The number of basic building blocks is surprisingly small and limited, considering the complexity and diversity of a system. For example, proteins are typically composed of 20 standard amino acids, and bones are combinations of some mineral salts and a protein (collagen). Thus, it can be said that a life is formed through hierarchical self-assembly of those basic units. Today, we live with splendid technological developments. However, even the state-of-the-art technologies of humans cannot build the simplest form of living organisms, which implies that self-assembly can excellently perform high-tech jobs that cannot easily be done with current human abilities. Therefore, studying self-assembly may be a starting point of another technological revolution in the development of human history.

Nanoscale features with high precision are fundamental building blocks for a variety of applications including highly integrated nanodevices. The rising demand for nanoscale fabrication methods, combined with the inherent feature-size limitations of optical lithography and the low throughput of electron-beam lithography, have motivated a search for cost-effective nanoscale fabrication technologies, including nanoimprint lithography,[1] dip-pen nanolithography,[2] and self-assembled block copolymer lithography.[3-7]

There are several general requirements that need to be satisfied for a volume nanomanufacturing process to be practical.[8]

- The method should be able to pattern high-resolution features (<20 nm).
- Long-range ordering of the patterns should be achieved in a simple manner.
- Large-area (> 4 in) patterning should be possible.
- The process should provide patterns with arbitrary structures.
- The throughput should be reasonably high.
- Cost effectiveness should be guaranteed.
- Defect density should be low enough.

This thesis focuses on introducing novel nanofabrication processes based on the self-assembly of siloxane block copolymers. One of the major achievements of this study is the formation of defect-free and robust nanoscale line patterns from poly(styrene-*b*-dimethylsiloxane) (PS-PDMS), which can be considered as a promising alternative for nanolithography. Although PS-PDMS has been studied in the bulk and used as a compatibilizer for polymer blends, this may be the first report about its thin film templating behavior and its applications in nanolithography. Chapter 2 introduces the uniform formation of self-assembled patterns over a large area, which is confirmed by characterization techniques. The degree of long-range ordering (>several microns) of PS-PDMS is exceptional among block copolymer-based self-assemblies. We can control the orientation of the templated patterns to give arrays of parallel nanowires of PDMS either parallel or perpendicular to the template edge. Conditions that yield these different orientations are systematically presented. This level of control will be critical in making self-assembled nanoscale devices, for example cross-point architectures.

Chapter 3 deals with the systematic tunability of patterns by solvent vapors. Vapor pressure can manipulate the incompatibility and consequently the domain spacing of block copolymers. The results show that the morphology of a thin film of a cylinder-forming PS-PDMS block copolymer can be changed from an array of parallel lines to an array of close-packed holes. Moreover, the line period and the linewidth can be varied independently over a certain range. This result and methodology is important because it is generally assumed that the period and geometry of a block copolymer film are fixed by the block lengths and volume fractions, i.e. a certain block copolymer will generate a fixed pattern. By understanding the effects of both a selective solvent (heptane) and a partially selective solvent (toluene), the results described can be generalized to other block copolymer systems.

In chapter 4, the large-area and uniform fabrication of 15 nm wide poly(3,4-ethylenedioxythiophene):poly(styrenesulfonate) (PEDOT: PSS) conducting polymer nanowires is reported. The nanowires were obtained through reactive ion etching processes using self-assembled PS-PDMS block copolymer patterns as an etch mask. This technique may be versatile because the same process can be simply extended to the patterning of other organic materials. These PEDOT:PSS nanowires have the highest pattern density (2.85×10^5 cm^{-1}) reported for conducting polymer nanowires. Moreover, the nanowires are perfectly ordered in a large-area substrate, which can be readily scaled up to much larger substrates since every processing technique used here was a parallel process. The chapter also demonstrates the capability of the patterned structures to operate as an ethanol vapor sensor, confirming the preservation of the electronic properties of the PEDOT:PSS during the patterning processes. The sensitivity ($\Delta R/R_0$) of the nanowire array is compared with those of thin films, and the effect of surface-to-volume ratio on the sensitivity was discussed. These well organized conductive polymer nanowire arrays may be useful for nanoscale organic device components such as interconnect lines or nanoelectrodes for high-density and high-performance nanodevices.

Chapter 5 presents the uniform formation of concentric ring patterns self-assembled inside shallow circular templates. Self-organizing ring patterns were generated in approximately a few billion templates, which are defined on silicon substrates by UV laser interference lithography. This is a demonstration of extended shape-tunability by a rational choice of template design and a macroscopic realization of uniform self-assembly. Besides linear patterns or dots which can be used for interconnect lines or active elements, these nanoscale ring patterns can be potentially applied to magnetic memory elements, which are presented in chapter 7, or biological sensor devices. The confinement diameter was extensively varied, and its effects on the fluctuation of outer diameter and pattern period of the rings were carefully analyzed. The repeat period for frustrated block copolymers under cylindrical confinement has been inconsistent among reports. This chapter also reports noticeable and consistent decreases in the pattern period for the well-defined rings compared to linear patterns. A free energy model composed of interfacial, strain, and bending energy was employed to explain the smaller periods and more sensitive period variation of inner rings with smaller radii of curvature.

Chapter 6 describes the self-assembly of dot patterns using a sphere-forming PS-PDMS block copolymer and lithographically-defined templates. As will be shown in chapter 2, long-range ordering of spherical block copolymers is commonly induced by linear templates patterned, for example, with interference lithography. This is a very simple and scalable approach since those templates can be readily fabricated with conventional optical lithography techniques. Alternatively, a novel graphoepitaxy technique, which utilizes sparsely-arranged post arrays as guiding templates, is also introduced. This approach can achieve seamless nanostructures over a large area since the lithographically-defined posts are practically indistinguishable from the self-assembly patterns due to the similarity in chemical compositions. The effects of commensurability between the patterned posts and block copolymer spacing on the orientational relationship between the two lattices will be discussed.

Chapter 7 presents generation of ordered arrays of nanoscale line, rings, and holes in various metallic thin films by using templates made from cylindrical and spherical morphology block copolymers. A novel pattern-reversal technique is introduced. A CF_4 plasma etching process mechanically etches the metal films and chemically etches the block copolymer dots, leaving well-defined metallic nanostructures with the reverse image of the original block copolymer templates. Examples of Ti, Pt, Ta, W, silica and magnetic Co and Ni patterns and their characterization results are presented. A double pattern reversal process was used to form Ni dot arrays. This methodology is important because this simple process can be applied to a wide range of materials, and may be used to make a diverse range of nanoporous films, which can be useful in applications including via formation in integrated circuits, filters, plasmonic and photonic bandgap structures, catalysts, templates, sensors, and solar cells.

1.2 Nonconventional nanofabrication techniques

Electron beam technologies have been employed for decades to produce the masks for optical lithography. Since the wavelength of electrons in such tools is typically less than 0.1 nm, the resolution limit of conventional optical lithography, which is caused by diffraction, can be solved. Thus, sub-10 nm pattern generations have been demonstrated for many years.[9] The chief disadvantage of this technique is extremely small throughput compared to optical lithography since most e-beam tools make patterns by scanning the area serially.

This section introduces a few promising and alternative nanofabrication techniques, which may be compared with block copolymer self-assembly. Conventional lithography tools may include photo-lithography and maskless scanning-beam-based techniques such as electron beam lithography or focused ion beam lithography. The resolution of optical lithography is limited by diffraction, and the drawbacks of the scanning beam techniques may include high cost and long exposure time. These limitations have motivated researchers in academia and industries to explore unconventional approaches. Although those unconventional methods may have their own limitations, they are continuously evolving and competing with the conventional approaches. Table 1-1 shows the comparative performances of nanofabrication techniques. Block copolymer techniques have advantages of high resolution, high throughput, and low cost. Although overlay issues have not been systematically studied yet, a template generation process by optical or electron-beam lithography may resolve the problem since the position and orientation of block copolymer patterns are determined by the template patterns. The detailed pattern formation mechanism of block copolymers is described in section 1.3.

Table 1-1 Comparison of nanofabrication techniques (O: Good, **Δ: Moderate, X: Poor)**

Techniques	*Resolution*	*Throughput*	*Cost*	*Defect*	*Overlay*
Optical	Δ	O	X-Δ	O	O
E-beam	O	X	X	O	O
AFM	O	X	Δ	O	O
Imprinting	O	O	Δ	Δ ~O	Δ
BCP	O	O	O	Δ	X~ Δ

1.2.1 Imprinting techniques

The principle of nanoimprinting lithography is very straightforward. First, nanoscale relief structures are made on a stiff mold using other lithography techniques such as e-beam lithography.[10] A proper range of mechanical stiffness of the mold patterns and mechanical flexibility of the substrates are important for high quality pattern replication over a large area since secure and uniform contact should be made. Then, the mold is pressed onto a soft material (e.g. a polymer above its glass transition temperature) with proper pressure, temperature, and pressing time. The resultant topography on the polymer is an inverse image of the original mold. Molding inevitably leaves a residual layer, which needs to be removed through a dry etching process. Nanoimprinting lithography innately provides a high-throughput process owing to parallel printing and etching processes. Moreover, this tool can produce ultrahighresolution replicas without much difficulty. Figure 1-1c shows arrays of pillars and holes with diameter of 10 nm.[10] However, the high viscosity of the polymers limits the range of pattern density due to the constraint of flow distance. More recently, UV nanoimprint lithography utilizing an UV-curable resist and an UV-transparent mold has attracted much interest due to the processability at room temperature and higher throughput.[11, 12] Moreover, the technique can avoid incomplete mold filling by using a low-viscosity fluid. However, defect level, throughput, and mask fabrication issues do not meet the strict requirements of semiconductor manufacturing.[10]

Alternatively, soft and flexible stamps can be made by coating a liquid polymer precursor on topographically patterned substrates.[13] Subsequent replica molding can fabricate multiple copies with the same topography as the patterned substrate. The replicas can be inked by immersion in an inking solution (e.g., thiol-terminated molecules in alcohols) and the inked replicas can be stamped on a substrate.[13] As a result, a patterned monolayer of functionalized molecules is obtained on the substrate. This method is very inexpensive and is well-suited for biotechnologies and flexible electronics.

However, flexible replicas often show issues in mechanical stability such as sagging or shrinking of patterns.

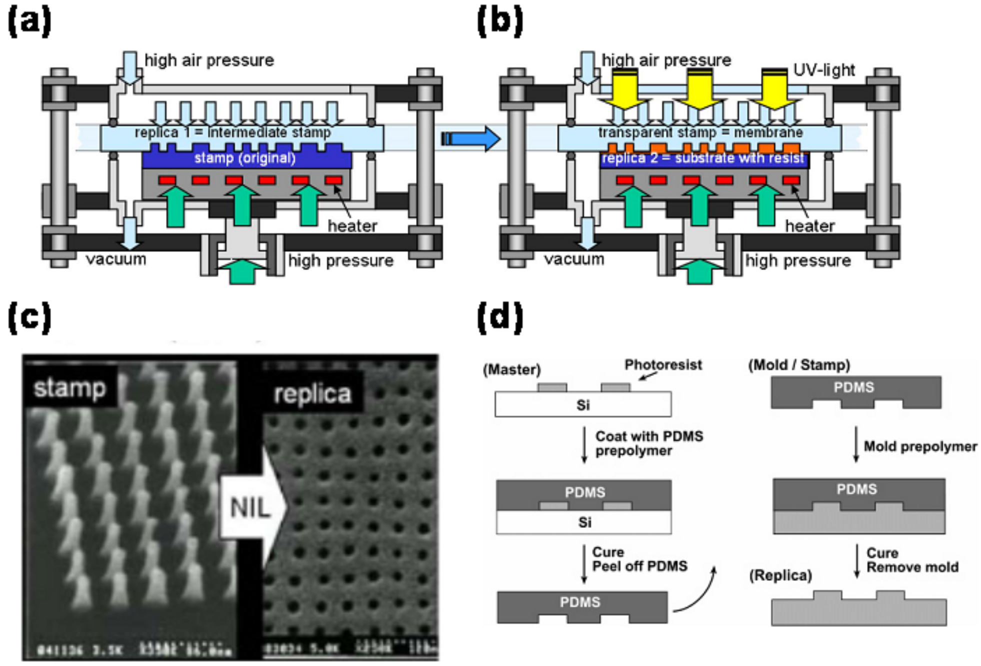

Fig. 1-1 Possible configuration of (a) thermal and (b) UV nanoimprinting. (c) 10-nm-scale structures patterned by nanoimprinting lithography. (d) Schematic of mold fabrication and pattern multiplication.[10, 13]

1.2.2 Scanning-probe-based nanolithography

Scanning probe microscopes such as atomic force microscopes (AFM) are widely used due to their capability to observe atomic scale objects. They can be used for investigating the surfaces of various kinds of materials such as biological molecules, inorganic crystals, or even fluids. More-or-less simple structures and excellent controllability of these tools have facilitated the studies on the local modifications based on electrostatic, electrochemical, or thermal interactions between the sharp cantilever tips and various kinds of surfaces.[14] The reactions are spatially confined in a small spot defined by the geometry of probe tip. Local oxidation nanolithography as schematically shown in Fig. 1-2 is an example. The AFM tip is used as a cathode and the water meniscus is the electrolyte for the reaction.[14] The half-cell reaction at the anode is

$$M + nH_2O \rightarrow MO_n + 2nH^+ + 2ne^-$$

The fabricated oxides can serve as masks for etching, templates, or dielectric barriers. The same technique can also be used for patterning self-assembled monolayers (SAM).[14] On top of SAM, local oxidation can be done to remove the SAM on the area where the tip passes. Then, another functionalization can be performed with different molecules on the patterned region since the oxidized area terminates with OH groups. Several applications such as read-only memories, transistors, and quantum ring devices have been suggested.

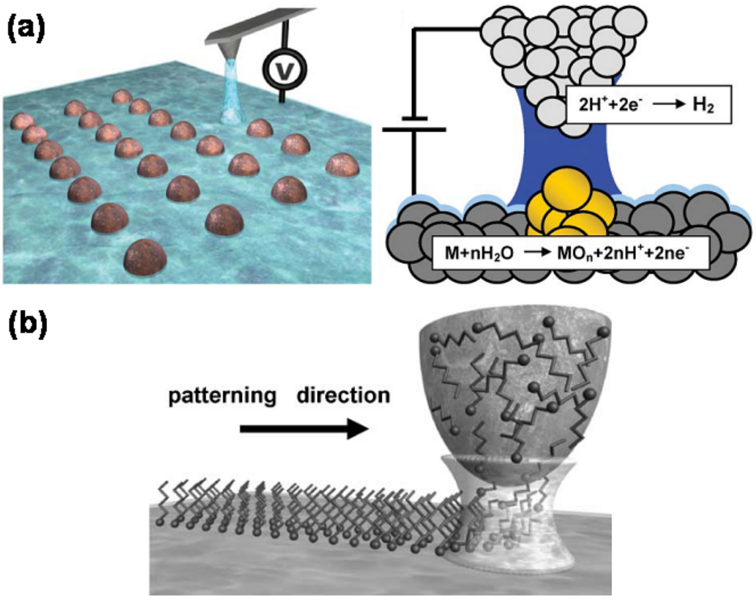

Fig. 1-2 Schematics of (a) local oxidation nanolithography by an AFM tip and (b) dip-pen nanolithography.[14]

Dip-pen nanolithography utilizes the deposition of thiol-terminated organic molecules from an AFM tip onto a gold surface.[2] A water meniscus is formed between the tip and the substrate, and it is a path for the diffusion of the molecules. However, the exact mechanism of the deposition has not been revealed yet. Dip-pen lithography can also write with functionalized proteins or DNAs or proteins.[6] The minimum feature size achieved is around 15 nm for alkanethiols inks. The disadvantage of these probe-based techniques include very low throughput and limited availability of substrates.[13]

1.3 Self-assembly of block copolymers

1.3.1 Introduction

A copolymer is composed of at least two distinct repeating monomer units. In copolymers, the repeating units can be placed randomly (random copolymer), alternating (alternating copolymer), or in blocks (block copolymer). A block copolymer can have only two blocks (diblock copolymer) or more (multiblock copolymers). There can be more complex architectures of block copolymers such as star, comb, or ladder-shaped block copolymers, where different chains can form each branch. In fact, the possible geometrical arrangements of blocks is infinite. This thesis will mainly deal with the properties of diblock copolymers. In general, block copolymers can be synthesized through living anionic polymerization, where the polymers get longer by the supply of precursors to the growing anionic chain. This method provides constant growth rate and excellent small polydispersity index; moreover, the overall growth process can be composed of separate stages using different monomers for growing each block.[15, 16] Additional advantages are precisely controllable molecular weights and end-groups of the final products.

Block copolymers have been extensively utilized for industrial purposes such as solubilizers, compatibilizers, foams, oil additives, and thermoplastic elastomers.[17] However, the boom of block copolymer researches was started decades ago after it was found that various kinds of nanoscale self-organization can be induced by simply tethering mutually immiscible chains together at their ends.[18] The excellent regularity and small size of the self-assembled features have attracted a lot of attention from various fields. In particular, the self-assembly of the microdomains of diblock copolymers within lithographically-defined templates to create patterns with long range order has attracted considerable attention, due to the scalability and cost-effectiveness of the process.[19, 20] Devices such as field effect transistors, capacitors, flash memory cells, high density magnetic storage media, photovoltaic devices, and photonic crystals made using block copolymer patterning have been proposed or demonstrated.[21-24]

1.3.2 Phase behavior of block copolymers

The thermodynamics of block copolymers composed of mutually incompatible blocks is governed by two opposing effects, entropy and enthalpy. At a lower temperature, an enthalpic effect drives the blocks to phase-separate, while an entropic effects, which dominates at a higher temperature, results in a homogeneous mixture of chains (Fig. 1-3).

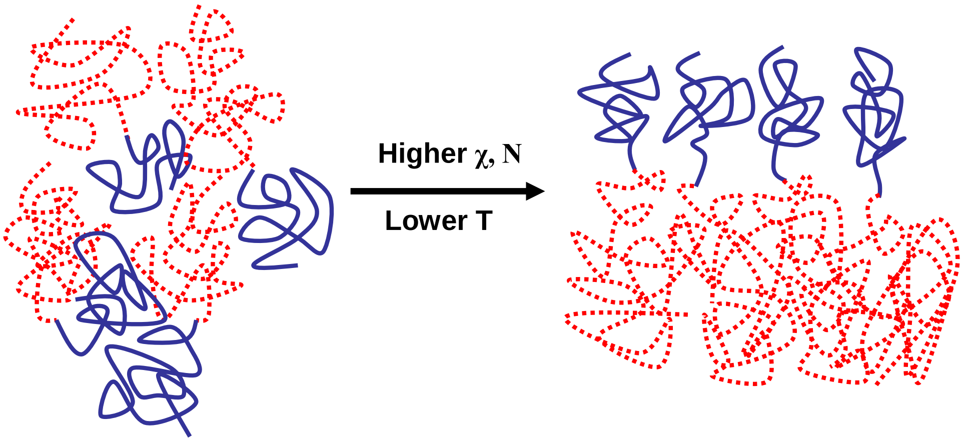

Fig. 1-3 Microphase separation of block copolymers.

In the case of a mixture of two homopolymers, phase-separation is thermodynamically favorable only when the Gibbs free energy of mixing is greater than 0. The free energy is given by the following expression.

$$\frac{\Delta G_{mix}}{k_b T} = \frac{f_A}{N_A}\ln(f_A) + \frac{f_B}{N_B}\ln(f_B) + f_A f_B \chi$$

where f and N are the volume fraction and the number of repeating unit of each homopolymer and χ is the Flory-Huggins interaction parameter. The χ parameter is related to the enthalpic contribution for phase-separation dominated by the incompatibility of monomer units. The product χN is the segregation strength, which reflects both enthalpic and entropic contributions.

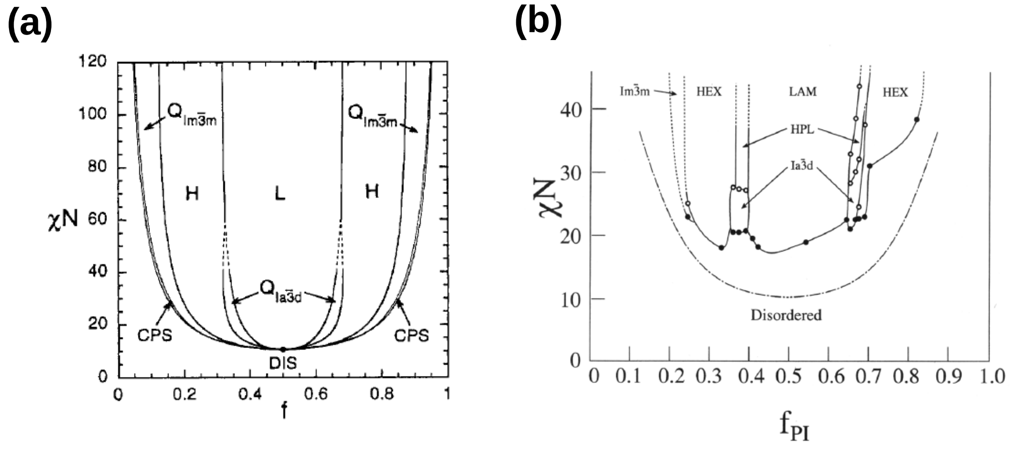

Fig. 1-4 Phase-diagrams of diblock copolymers (a) predicted by self-consistent mean field theory and (b) obtained experimentally. [25]

Fig. 1-4a shows a phase diagram calculated based on the self-consistent mean-field theory. The phase-diagram is divided into several regions depending on χN and f. When χN is smaller than a certain value (order-disorder transition; ODT) at a given composition, chains are intermixed and the morphology is disordered. For a diblock with symmetric chain length and conformation, $(\chi N)_{ODT} = 10.5$ in the mean-field calculation. If χN is slightly over the ODT value ($10.5 < \chi N < 12$), it corresponds to the weak segregation limit (WSL), where the composition profile is sinusoidal.[3] When $\chi N >> 10$ (strong segregation limit; SSL), the composition profile is close to a square function, and the interphase region is narrow. In SSL, the interfacial width and the microdomain dimension scale with $a\chi^{-1/2}$ and $aN^{2/3}\chi^{1/6}$, respectively.[3]

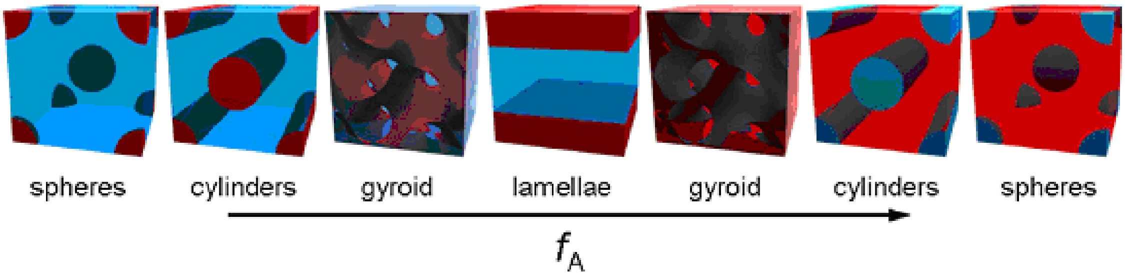

Fig. 1-5 Various morphologies of diblock copolymers with a different minority volume fractions.[20]

For $\chi N > (\chi N)_{ODT}$, the ordered phase can have body-centered cubic, hexagonally-packed cylinder, bicontinuous cubic gyroid, or lamellar phases depending on the composition and χN, as shown in Fig. 1-5, although in SSL the phase is almost independent of χN. [3, 25] The bulk phase of diblock copolymers can be determined from peak positions in the diffraction spectra of small-angle x-ray scattering (SAXS). Lamellar, cylindrical, and spherical phases have the peak position ratios of 1:2:3:4:...., 1:√3:√7:√9:...., and 1:√2:√3:√4:√5:...., respectively.[17] When the composition $f_A > 1/2$, the minority B chains gather into the inside of cylinders or spheres. This arrangement is energetically more favorable since the conformational entropy can be more increased by reducing chain-stretching.

Although the calculated phase-diagram is symmetric, as shown in Fig. 1-4a, due to the assumption of symmetric chains, real phase diagrams often show significant asymmetry due to the differences in sizes and shapes of repeating units and the dissimilarity in the chain conformation of two blocks.[17] Experimentally determined phase-diagrams are more complex and distorted as shown in Fig. 1-4b. The asymmetry also results because interactions between two blocks are not precisely represented by one universal χ parameter because χ is also dependent on f and N. The real energy penalty for making contacts between two blocks is dependent on which block is the majority.[17] One more difference between the two phase diagrams is the existence of hexagonally perforated lamellar (HPL) in the experimental phase diagram. However, it was argued that this phase is not thermodynamically stable, but is rather a long-lived transient (metastable) structure.[17] This thesis reports the formation of HPL structures induced by annealing with mixed solvent vapors in chapter 3.

For many applications, especially for lithography, we require a thin film of block copolymer on substrates. The thickness is controlled by the concentration and spin coating speed. Block copolymer thin film morphologies are influenced by the surface boundary conditions at interfaces such as polymer/substrate and polymer/air. An equilibrium period is determined by the chain length and processing conditions. For lithography applications, monolayer patterns are used as etch masks or templates. Thus, the orientation of BCP morphologies is important since it can change the pattern geometry. Fig. 1-6 presents possible morphologies of lamellar BCP films with different thickness and interfacial energy. If the film thickness (t) is similar to the equilibrium thickness (L_0), we can obtain smooth and uniform thin films with lamellae planes aligned parallel with the substrate since the free energy can be reduced by preferentially segregating one domain, which gives lower energy at the interfaces. The energetically favored block at each interface can be different or the same. For example, one block can reduce the free energy at the substrate interface and the other block can have lower surface energy. However, when $t < L_0$ or $t > L_0$, the orientation can change depending on the interfacial energy. If the asymmetry in the interfacial energy between two blocks is significant, holes or islands will form, maintaining the parallel orientation to accommodate the thickness difference.[17] On the other hand, if there is little difference in the interfacial energy, perpendicularly oriented lamellar films can be obtained. By changing the orientation, the BCPs can avoid the increase of surface area accompanied by the formation of holes or islands, and effectively reduce stretching or compression of chains given by the non-ideal film thickness.[17]

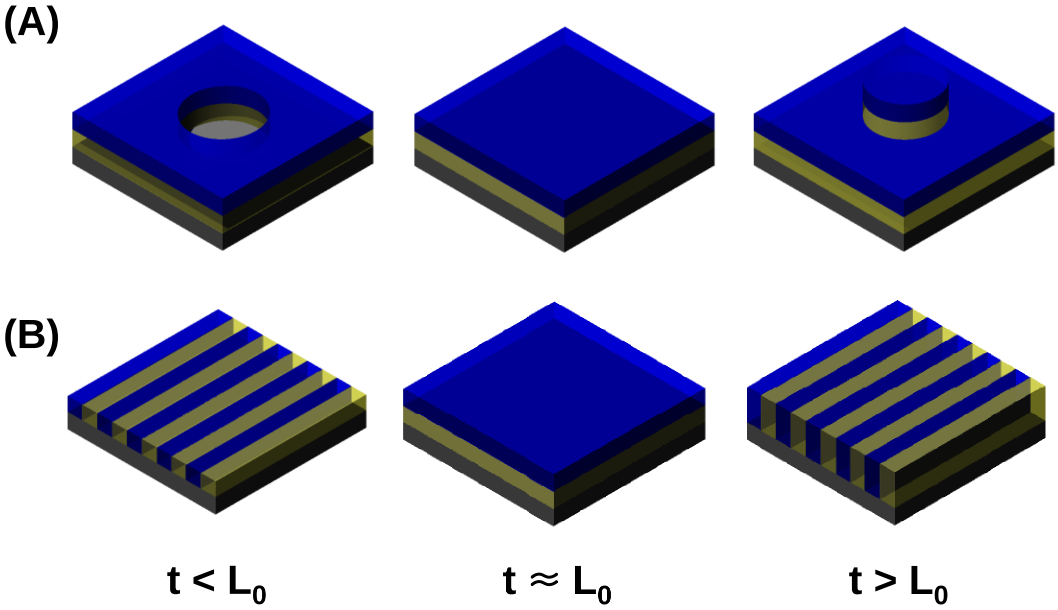

Fig. 1-6 Structures and orientations of block copolymer thin films with different thicknesses. The cases of (a) large and (b) little asymmetries in interfacial energy.

1.3.3 Block copolymer micelles

This thesis does not describe experimental results on block copolymer micelles. However, BCP micelles have extensive applications especially in the biomedical field mainly due to the responsiveness to environmental stimuli such as pH, ionic strength, or temperature. PS-PDMS block copolymers can form well-controlled micelle structures due to a large incompatibility between two blocks. Thus, basic mechanisms for micelle formation are introduced here.

Amphiphilic BCPs have affinities for two dissimilar environments. For example, one block is hydrophobic, while the other is hydrophilic. If block copolymers are dissolved in a selective solvent, which is a thermodynamically good solvent for one block and a precipitant for the other, the BCP chains would aggregate reversibly to form micellar structures. Micelles represent another form of microphase separation, which can occur both in aqueous and organic solvents. Depending on the concentration of micelles, micellization or gelation can occur.[17] In a very dilute solution, BCPs behave as unimers. However, if the concentration is over the critical micelle concentration (CMC), micelles with a core of the insoluble blocks and a corona of the soluble blocks will be generated. If the concentration is high enough over the critical gelation concentration (CGC), gelation occurs and the micelles have an ordered arrangement.[17] Depending on the relative chain length of the blocks, the structure of the micelles is determined. If the corona block is much longer than the core block, star-micelles are formed, and in the opposite case crew-cut micelles are produced.

The structure and dimension of BCP micelles can be manipulated by variables that influence the attractive and repulsive forces balancing the system. The total free energy of a micelle may be the sum of the deformation energy of the core and the corona and the interfacial energy between them. Understanding also the inter-aggregate forces in addition to the intra-aggregate forces may be important to predict the structure formed at equilibrium. It is also critical to understand the effects on the morphology and dimension, of the parameters such as solvents, micelle concentration, temperature, chain lengths, polymer architecture, and so on. The stability of micelles is important since the behavior and properties of stable micelles are more predictable and possibly useful. High stability requires low values of CMC and CMT.[26] Polymer blocks with a high glass transition temperature such as polystyrene are kinetically frozen at room temperature and decrease

CMC and CMT. A large Flory-Huggins interaction parameter also helps the stabilization.[26] In addition, crosslinking of polymers before or after micellizations have been reported to be useful.

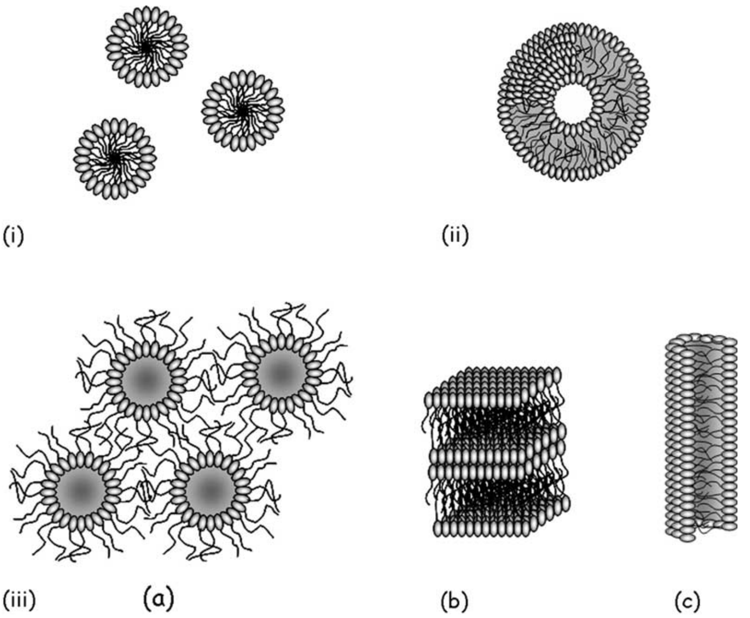

Fig. 1-7 Schematics of block copolymer micelles: (i) direct micelles, (ii) vesicles, and (iii) other morphologies: (iiia) inverse micelles, (iiib) lamellar structures, and (iiic) cylindrical or tubular micelles.[26]

1.4 Magnetic nanostructures and devices

Magnetic nanostructures have one, two, or three dimensions in the nanoscopic regime. Common examples are magnetic films and patterned thin film elements, nanoparticles, and nanowires. Magnetic nanostructures have numerous potential applications such as recording media, read heads, magnetoresistive sensors, and magnetic memory devices.[27-31] Magnetic recording technologies are targeting data storage densities on the order of one terabit per square inch.[32] To achieve this, perfectly arranged sub-20 nm scale magnetic nanostructures should be available. Stable magnetization states and reproducible switching processes are important for the applications. Various magnetic nanostructures with different geometries have been studied. However, in general, the magnetic configurations and switching mechanisms are highly dependent on geometry and edge roughness, limiting the utility for today's stringent applications.[33] In some applications such as memory cells, circular geometries can be used to lessen the dependence of magnetic properties on roughness due to the existence of vortex state, which makes the edge roughness less important.[33-35] The vortex state in ring-shaped geometries is more stable than it is in circular disks due to the absence of the unstable vortex core. This thesis research therefore focused on making magnetic nanorings by BCP lithography. This section describes the fundamental properties of ferromagnetic nanorings. The fabrication of thin film rings using block copolymer self-assembly is demonstrated in chapter 5.

The total energy of any magnetic structures can be expressed as

$$E = E_{ex} + E_H + E_{el} + E_{ca} + E_d$$

where E_{ex} is the exchange energy, E_H is the Zeeman energy, E_{el} is the magnetoelastic energy, E_{ca} is the crystalline anisotropy energy, and E_d is the magnetostatic energy. [31]

The exchange energy is caused by the interaction between neighboring spins and can be expressed as

$$E_{ex} = -2\sum_{i>j} J_{ij} S^2 \cos\theta_{ij}$$

where J_{ij} is the exchange integral, S is the spin of each atom, and θ_{ij} is the angle between individual spins.

The Zeeman energy is the magnetic potential energy and can be written as

$$E_H = -M \cdot H$$

where M is the magnetization and H is the magnetic field.

The magnetoelastic energy results from the interaction between magnetic properties and lattice strain and is typically less important for nanostructures than bulk forms.[31]

The magnetocrystalline anisotropy energy is caused by spin-orbit coupling. Due to the arrangement of atoms in crystalline materials, magnetic spins tend to align along easy crystal directions. For materials with a hexagonal close-packed structure, the magnetocrystalline anisotropy can be expressed as

$$E_{ca} = K_0 + K_1 \sin^2\theta + K_2 \sin^4\theta + \cdots\cdots$$

where K_0, K_1, and K_2 are constants and θ is the angle between the magnetization direction and the easy axis.[36] Polycrystalline films have random crystallographic orientations, and thus the average magnetocrystalline anisotropy is so small that they can be considered to be magnetically isotropic.

The magnetostatic energy is caused by the demagnetizing field, which acts in the opposite direction from the magnetization and can be written as

$$E_D = \frac{1}{2} N_d M_s^2$$

where N_d is the demagnetizing factor along the magnetization direction and M_s is the saturation magnetization.

Among the several competing energy terms, the Zeeman energy (E_H), the exchange energy (E_{ex}) and the magnetostatic energy (E_d) are most important in polycrystalline thin film nanorings. At very high magnetic field, the rings have a single-domain state (saturated), as presented in Fig. 1-8c. As the magnetic field is reduced and finally removed, a bidomain state so-called "onion state" (Fig. 1-8b), where the magnetization follows the perimeter of the rings, is formed since the Zeeman energy becomes less important than the exchange energy. At the onion state, there exist two head-to-head domain walls parallel to the applied magnetic field.[33-35] A reverse field depins one of the two domain walls, which annihilates the other domain wall, forming a state called a "vortex state" (Fig. 1-8c) with near-zero remanent magnetization. At a larger reverse field, a reverse magnetic domain forms in the region of the vortex antiparallel to the field, which grows, producing a reverse onion state and eventually a fully saturated state with a single domain.

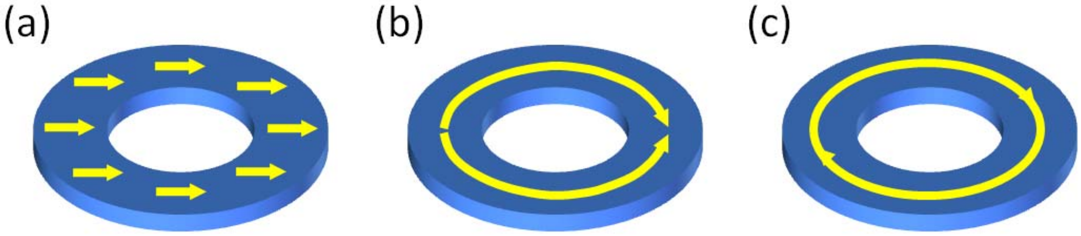

Fig. 1-8 Schematic diagrams of the magnetization states in ferromagnetic thin film rings. (a) Saturated state, (b) onion-state, and (c) vortex-state

However, the stability of the vortex state is highly sensitive to the geometrical parameters of nanorings. For instance, a vortex state is more stable for rings with a higher thickness and a smaller width.[33-35] With an increase of thickness, the magnetostatic energy becomes more dominant, and consequently the stray-field-free vortex state is favored. If a ring is narrower, due to a shape-anisotropy effect, the formation and propagation of a reverse domain is more difficult since this process requires rotation of spins and a significant increase of magnetostatic energy at the domain walls.

1.5 Chemical sensors

Chemical sensors have been widely used for detecting toxic materials which are dangerous to humans and the environment. For the last few decades, many researchers have tried to make simpler, cheaper, and more robust solid-state chemical sensors. The devices are generally based on the change of resistance or capacitance of materials caused by the introduction of chemical species, which are related to the adsorption and desorption of materials on the surface of the sensing materials.[37] The development of microelectronics has also driven progress in sensor technologies, and the major technological direction in the field is to develop small scale sensors which can be integrated with microelectronic devices. Moreover, so-called "electronic noses" may contain signal detection and processing functions in a single chip. Analyses of multiple gas components require sophisticated pattern-recognition algorithms, which is similar to the phenomenon that occurs in the human nose and brain.

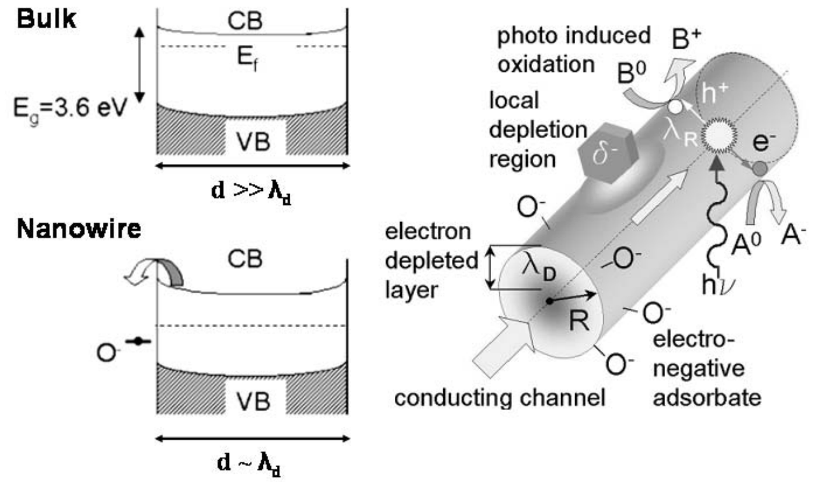

Fig. 1-9 Band bending of nanostructured oxide materials by adsorption of oxidizing and reducing gases. (Left) A summary of a few of the electronic, chemical, and optical processes occurring on metal oxides. (Right)[37]

State-of-the-art commercial sensors are usually based on metal oxides in the form of single-crystals, films or powders. The electronic properties of metal oxides are frequently very sensitive to changes in the external environment such as gas/liquid atmosphere, temperature, or pressure. Thus, the majority of commercially available sensor products is based on multicomponent oxides or doped oxides, which are also properly structured to improve their performance.

Moreover, scaling-down to a few to tens of nanometers can provide additional advantages. Nanoscale materials have a larger surface-to-volume ratio, and therefore a large fraction of atoms can participate in surface reactions.[37] Furthermore, the Debye length (measure of the field penetration into the bulk) becomes comparable to the dimension. Thus, conductivity can be varied from a fully nonconductive state to a highly conductive state, which means that higher sensitivity can be obtained. A smaller carrier diffusion length contributes to the rapid response and recovery. For example, sensors fabricated with In_2O_3 nanowires show a sensitivity approximately 10^5 times larger than that of a bulk form.[38]

On the other hand, percolation theory has been employed to explain the resistance change of composite sensor materials composed of carbon black or polypyrrole as a conductive filler and nonconductive organic polymers as the insulating matrix.[39] Through exposure to vapor or gas molecules, the composites would show different degrees of swelling depending on the interactions between the composite and the molecules, and this swelling leads to a change in the conductivity of the composite film. Percolation theory predicts that the conductivity scales with $\sim |\varphi-\varphi_c|^\alpha$, where φ (φ_c) is the volume fraction of the (critical) conductive component and the exponent α is in the range 1.5–2. Recently there have been reports that pure polymer nanowire devices integrated into microelectronic circuits show superior performance.[15, 40] It has been suggested that a higher surface-to-volume ratio causes faster diffusion of solvent molecules, and this gives nanostructured materials and thinner films a faster, higher amplitude response.[41-44] The fabrication and sensor measurement results of conducting polymer nanowires are presented in chapter 4.

References

[1] S. Y. Chou, P. R. Krauss, W. Zhang, L. J. Guo, L. Zhuang, "Sub-10 nm imprint lithography and applications", *Journal of Vacuum Science & Technology B 15*, p. 2897 (1997)

[2] R. D. Piner, J. Zhu, F. Xu, S. H. Hong, C. A. Mirkin, ""Dip-pen" nanolithography", *Science 283*, p. 661 (1999)

[3] F. S. Bates, G. H. Fredrickson, "Block Copolymer Thermodynamics - Theory and Experiment", *Annual Review of Physical Chemistry 41*, p. 525 (1990)

[4] J. Y. Cheng, C. A. Ross, V. Z. H. Chan, E. L. Thomas, R. G. H. Lammertink, G. J. Vancso, "Formation of a cobalt magnetic dot array via block copolymer lithography", *Advanced Materials 13*, p. 1174 (2001)

[5] J. Y. Cheng, C. A. Ross, H. I. Smith, E. L. Thomas, "Templated self-assembly of block copolymers: Top-down helps bottom-up", *Advanced Materials 18*, p. 2505 (2006)

[6] K. B. Lee, S. J. Park, C. A. Mirkin, J. C. Smith, M. Mrksich, "Protein nanoarrays generated by dip-pen nanolithography", *Science 295*, p. 1702 (2002)

[7] D. A. Vega, C. K. Harrison, D. E. Angelescu, M. L. Trawick, D. A. Huse, P. M. Chaikin, R. A. Register, "Ordering mechanisms in two-dimensional sphere-forming block copolymers", *Physical Review E 71*, p. 061803 (2005)

[8] S. V. Sreenivasan, "Nanoscale manufacturing enabled by imprint lithography", *Mrs Bulletin 33*, p. 854 (2008)

[9] W. Chen, H. Ahmed, "Fabrication of Sub-10 Nm Structures by Lift-Off and by Etching after Electron-Beam Exposure of Poly(Methylmethacrylate) Resist on Solid Substrates", *Journal of Vacuum Science & Technology B 11*, p. 2519 (1993)

[10] H. Schift, "Nanoimprint lithography: An old story in modern times? A review", *Journal of Vacuum Science & Technology B 26*, p. 458 (2008)

[11] E. K. Kim, N. A. Stacey, B. J. Smith, M. D. Dickey, S. C. Johnson, B. C. Trinque, C. G. Willson, "Vinyl ethers in ultraviolet curable formulations for step and flash imprint lithography", *Journal of Vacuum Science & Technology B 22*, p. 131 (2004)

[12] M. D. Stewart, C. G. Willson, "Imprint materials for nanoscale devices", *Mrs Bulletin 30*, p. 947 (2005)

[13] B. D. Gates, Q. B. Xu, M. Stewart, D. Ryan, C. G. Willson, G. M. Whitesides, "New approaches to nanofabrication: Molding, printing, and other techniques", *Chemical Reviews 105*, p. 1171 (2005)

[14] R. Garcia, R. V. Martinez, J. Martinez, "Nano-chemistry and scanning probe nanolithographies", *Chemical Society Reviews 35*, p. 29 (2006)

[15] J. Zhang, B. J. Wang, X. Ju, T. Liu, T. D. Hu, "New observations on the optical properties of PPV/TiO2 nanocomposites", *Polymer 42*, p. 3697 (2001)

[16] M. Kamigaito, T. Ando, M. Sawamoto, "Metal-catalyzed living radical polymerization", *Chemical Reviews 101*, p. 3689 (2001)

[17] A. K. Khandpur, S. Forster, F. S. Bates, I. W. Hamley, A. J. Ryan, W. Bras, K. Almdal, K. Mortensen, "Polyisoprene-polystyrene diblock copolymer phase diagram near the order-disorder transition", *Macromolecules 28*, p. 8796 (1995)

[18] G. E. Molau, *Block copolymers*, Plenum, New York (1970)

[19] C. T. Black, R. Ruiz, G. Breyta, J. Y. Cheng, M. E. Colburn, K. W. Guarini, H. C. Kim, Y. Zhang, "Polymer self assembly in semiconductor microelectronics", *IBM Journal of Research and Development 51*, p. 605 (2007)

[20] S. B. Darling, "Directing the self-assembly of block copolymers", *Progress in Polymer Science 32*, p. 1152 (2007)

[21] C. T. Black, "Self-aligned self assembly of multi-nanowire silicon field effect transistors", *Applied Physics Letters 87*, p. 163116 (2005)

[22] T. Deng, C. T. Chen, C. Honeker, E. L. Thomas, "Two-dimensional block copolymer photonic crystals", *Polymer 44*, p. 6549 (2003)

[23] V. Gowrishankar, N. Miller, M. D. McGehee, M. J. Misner, D. Y. Ryu, T. P. Russell, E. Drockenmuller, C. J. Hawker, "Fabrication of densely packed, well-ordered, high-aspect-ratio silicon nanopillars over large areas using block copolymer lithography", *Thin Solid Films 513*, p. 289 (2006)

[24] C. Osuji, C. Y. Chao, I. Bita, C. K. Ober, E. L. Thomas, "Temperature-dependent photonic bandgap in a self-assembled hydrogen-bonded liquid-crystalline diblock copolymer", *Advanced Functional Materials 12*, p. 753 (2002)

[25] F. S. Bates, G. H. Fredrickson, "Block copolymers - Designer soft materials", *Physics Today 52*, p. 32 (1999)

[26] J. Rodriguez-Hernandez, F. Checot, Y. Gnanou, S. Lecommandoux, "Toward 'smart' nano-objects by self-assembly of block copolymers in solution", *Progress in Polymer Science 30*, p. 691 (2005)

[27] L. Krusin-Elbaum, T. Shibauchi, B. Argyle, L. Gignac, D. Weller, "Stable ultrahigh-density magnetooptical recordings using introduced linear defects", *Nature 410*, p. 444 (2001)

[28] S. Kaka, M. R. Pufall, W. H. Rippard, T. J. Silva, S. E. Russek, J. A. Katine, "Mutual phase-locking of microwave spin torque nano-oscillators", *Nature 437*, p. 389 (2005)

[29] T. Atanasijevic, M. Shusteff, P. Fam, A. Jasanoff, "Calcium-sensitive MRI contrast agents based on superparamagnetic iron oxide nanoparticles and calmodulin", *Proceedings of the National Academy of Sciences of the United States of America 103*, p. 14707 (2006)

[30] J. Wang, "Nanoparticle-based electrochemical DNA detection", *Analytica Chimica Acta 500*, p. 247 (2003)

[31] H. Zeng, J. Li, J. P. Liu, Z. L. Wang, S. H. Sun, "Exchange-coupled nanocomposite magnets by nanoparticle self-assembly", *Nature 420*, p. 395 (2002)

[32] Z. Z. Bandic, D. Litvinov, M. Rooks, "Nanostructured materials in information storage", *Mrs Bulletin 33*, p. 831 (2008)

[33] M. Klaui, C. A. F. Vaz, L. Lopez-Diaz, J. A. C. Bland, "Vortex formation in narrow ferromagnetic rings", *Journal of Physics-Condensed Matter 15*, p. R985 (2003)

[34] C. A. Ross, F. J. Castano, D. Morecroft, W. Jung, H. I. Smith, T. A. Moore, T. J. Hayward, J. A. C. Bland, T. J. Bromwich, A. K. Petford-Long, "Mesoscopic thin-film magnetic rings (invited)", *Journal of Applied Physics 99,* p. 08S501 (2006)

[35] C. A. Ross, F. J. Castano, W. Jung, B. G. Ng, I. A. Colin, D. Morecroft, "Magnetism in multilayer thin film rings", *Journal of Physics D-Applied Physics 41* (2008)

[36] N. A. Spaldin, *Magnetic materials*, Cambridge University Press, New York (2003)

[37] A. Kolmakov, M. Moskovits, "Chemical sensing and catalysis by one-dimensional metal-oxide nanostructures", *Annual Review of Materials Research 34*, p. 151 (2004)

[38] C. Li, D. H. Zhang, X. L. Liu, S. Han, T. Tang, J. Han, C. W. Zhou, "In2O3 nanowires as chemical sensors", *Applied Physics Letters 82*, p. 1613 (2003)

[39] C. Brosseau, F. Boulic, P. Queffelec, C. Bourbigot, Y. L. Mest, J. Loaec, A. Beroual, "Dielectric and microstructure properties of polymer carbon black composites", *Journal of Applied Physics 81*, p. 882 (1997)

[40] H. Q. Liu, J. Kameoka, D. A. Czaplewski, H. G. Craighead, "Polymeric nanowire chemical sensor", *Nano Letters 4*, p. 671 (2004)

[41] C. Harrison, P. M. Chaikin, D. A. Huse, R. A. Register, D. H. Adamson, A. Daniel, E. Huang, P. Mansky, T. P. Russell, C. J. Hawker, D. A. Egolf, I. V. Melnikov, E. Bodenschatz, "Reducing substrate pinning of block copolymer microdomains with a buffer layer of polymer brushes", *Macromolecules 33*, p. 857 (2000)

[42] N. T. Kemp, D. McGrouther, J. W. Cochrane, R. Newbury, "Bridging the gap: Polymer nanowire devices", *Advanced Materials 19*, p. 2634 (2007)

[43] B. Dong, N. Lu, M. Zelsmann, N. Kehagias, H. Fuchs, C. M. S. Torres, L. F. Chi, "Fabrication of high-density large-area conducting-polymer nanostructures", *Advanced Functional Materials 16*, p. 1937 (2006)

[44] S. Virji, J. X. Huang, R. B. Kaner, B. H. Weiller, "Polyaniline nanofiber gas sensors: Examination of response mechanisms", *Nano Letters 4*, p. 491 (2004)

Chapter 2

Self-assembled pattern-generation of lines using a cylindrical block copolymer

2.1 Introduction

The growing demand for nanoscale fabrication methods, combined with the inherent feature-size limitations of optical lithography and the low throughput of electron-beam lithography, have motivated a search for cost-effective nanoscale fabrication technologies, including nanoimprint lithography,[1] dip-pen nanolithography,[2] and block copolymer lithography.[3-7] In the case of block copolymer lithography, the use of a chemical or topographical template enables control over the long range order of the self-assembled patterns, providing a simple and scalable nanopatterning method in which the feature sizes and geometries are controlled via the chain length and volume fractions of the block copolymer.

In block copolymer lithography, arrays of holes or dots may be defined using a spherical-morphology block copolymer[4, 6, 7] or a cylindrical-morphology block copolymer with the cylinders oriented perpendicular to the substrate.[8, 9] In contrast, patterns consisting of parallel lines may be defined using a cylindrical-morphology block copolymer with the cylinders parallel to the surface[10-12] or a lamellar block copolymer with a perpendicular orientation.[13, 14] Such patterns have been templated using both chemical and topographical substrate features. For example, lamellar poly (styrene-b-polymethyl methacrylate) (PS-PMMA) patterns have been templated using a self-assembled monolayer patterned by extreme ultraviolet interference lithography (EUV-IL) or electron-beam (e-beam) lithography, and have attracted much attention due to their high aspect ratio and absence of defects.[13, 14] However, this process requires template generation on the same length scale as the period of the block copolymer.[15] On the other hand, well-ordered arrays of in-plane cylinders templated by larger scale topographic patterns have been demonstrated by several groups. Horizontal cylinders from diblocks such as poly (styrene-b-ethylene propylene) (PS-PEP)[12] and PS-PMMA[10, 11] have been successfully aligned in templates. The templates have critical dimensions an order of magnitude or more larger than the block copolymer period, and can be made by optical lithography.

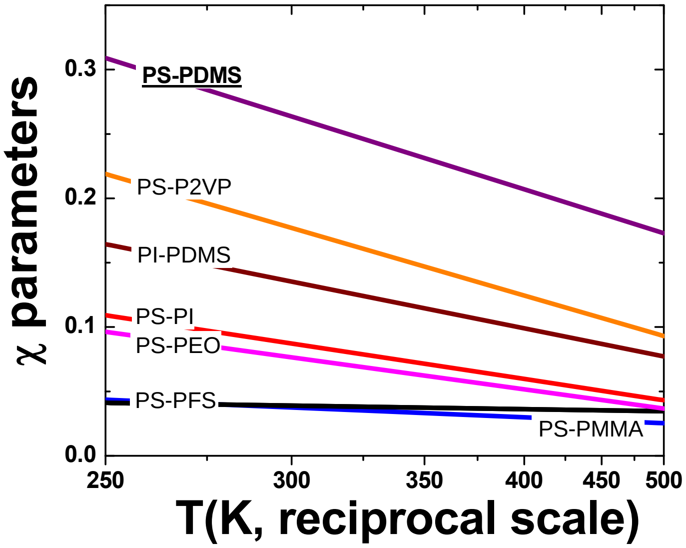

Fig. 2-1 Comparison of Flory-Huggins χ-parameters for common diblock copolymers. [16-19]

In all these examples the removal of one block leaves a structure made from the other block, typically PS, that could be used as a mask for pattern transfer into a functional material. PS is, however, a rather poor mask, having a glass transition temperature of 100°C and relatively low etch resistance. In addition, in these block copolymers a small but significant number of defects (dislocations or disinclinations) remain, which is undesirable for nanolithographic applications. The defect population is related to the Flory-Huggins interaction parameter, χ, which describes the driving force for microphase separation in the block copolymer. Block copolymers with higher χ have a higher driving force for reducing the defect population, and are therefore more desirable for achieving long range ordering.[20]

The ideal block copolymer for nanolithography applications therefore exhibits both a high value of χ and one highly etch-resistant block. Poly(styrene-b-dimethylsiloxane) (PS-PDMS) block copolymers satisfy both criteria. The high density of Si in the backbone of PDMS provides extremely high etch contrast between the two blocks when treated in an oxygen plasma, which is advantageous for pattern transfer into underlying materials, and the large interaction parameter χ, as shown in Fig. 2-1, enables the formation of ordered structures with a large correlation length. Moreover, PDMS has been widely utilized in soft lithography and micro/nanofluidic devices, and ordered PDMS block copolymer patterns may be expected to have extensive applications in nano- and biological technologies.[21] PS-PDMS has been studied in the bulk,[22] and has been used in forming polymer blends,[23] but its templating behavior and applications in nanolithography have not yet been reported. Here, we report the formation of defect-free robust nanoscale line patterns from PS-PDMS with an orientation that can be controlled by the annealing conditions and template geometry, and their use as etch masks for nanolithography.

2.2 Experimental

A diblock copolymer of PS-PDMS with overall molecular weight of 45.5 kg/mol and volume fraction of PDMS f_{DMS} = 33.5% was custom made by Polymer Source, Inc. The substrates used in this experiment consisted of smooth or trench-patterned Si substrates with native oxide layers. The 40-nm deep periodic trench patterns were fabricated using a Lloyd's Mirror interference lithography system with a 325 nm wavelength He-Cd laser to expose grating patterns in a trilayer resist, combined with reactive ion etching to transfer the grating into the substrate. The period of the trenches was close to 1 µm, and the mesa width was varied between 125 and 500 nm. In some experiments, the surfaces were modified by hydroxy-terminated PS or PDMS homopolymer with molecular weight 5kg/mol, which was spun-cast on the substrates and annealed at 150 °C for 15 hours, then washed with toluene to remove unreacted material. The thickness of the grafted brush layer was estimated to be around 3-4 nm by ellipsometry. 35 nm-thick thin films were obtained by spin-casting toluene solutions of 1.5% by weight of the block copolymer on the substrates, then the samples were solvent-annealed under toluene vapor at room temperature for 4 to 70 hours. The vapor pressure of toluene was controlled via the ratio R between the surface area of the liquid solvent and the volume of the annealing chamber. During solvent annealing, the block copolymer flows from the mesas to the trenches. The as-spun block copolymer film thickness was chosen so that, after solvent annealing, a monolayer of cylinders was present within the trenches while the mesas were left clear of cylinders. The annealed film was treated with a 5 sec, 50 W CF_4 plasma then a 90W O_2 plasma to remove the PS leaving oxygen-plasma-modified PDMS cylinders on the substrate. The surface morphology was observed using a Zeiss/Leo Gemini 982 scanning electron microscope (SEM) operated with an acceleration voltage of 5 kV. A thin layer of Au-Pd alloy was sputter-coated on the samples in order to avoid charging effects.

2.3 Thin film structure of a PS-PDMS block copolymer and two-step reactive ion etching

The surface tension of PDMS (γ=19.9 mN/m) is lower than that of PS (γ=40.7 mN/m),[24] and thus PDMS preferentially segregates at the air/polymer interface. This produces the structure shown schematically in Fig. 2-2 for a film formed on a PDMS-brush coated substrate. The thin continuous PDMS surface layer is resistant to an oxygen plasma, and an oxygen etch alone fails to produce sharp domain patterns (Fig. 2-3a). Therefore, a short (5 sec) CF_4 plasma treatment was performed to remove the PDMS surface layer before the oxygen plasma processing. Fig. 2-3b shows the results of this etching, which on a smooth substrate produces well-defined in-plane cylinder patterns without long range order.

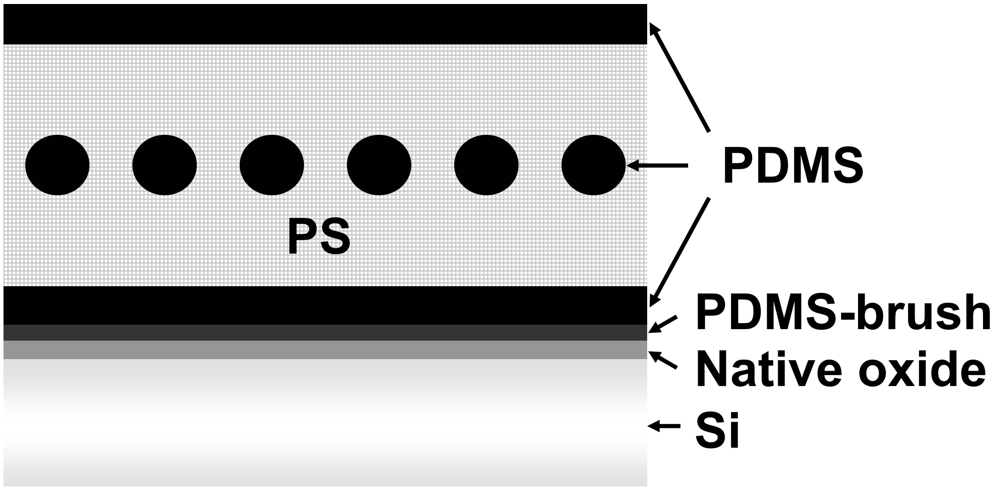

Fig. 2-2 Schematic cross-section diagram of a film of PS-PDMS on a PDMS-brush-treated silica surface. A layer of PDMS is present at the air-film interface, and below it a layer of parallel cylinders.

The structure in Fig. 2-3b is characterized by very smooth edges of patterns. The edge roughness is believed to scale with the thickness of the inter-material dividing surface (IMDS), which delineates the two blocks. The IMDS geometry is determined by the condition that interfacial energy is minimized and chain conformational entropy is maximized.[25] The χ parameter of PS-PDMS (χ~0.26) at room temperature is considerably larger than those of PS-PMMA (χ~0.06), poly(styrene-b-isoprene) (χ~0.09),poly(styrene-b-2-vinylpyridine) (χ~0.18), and poly(styrene-b-ethylene oxide) (χ~0.08), [16-19] leading to a thinner IMDS and low pattern edge roughness.

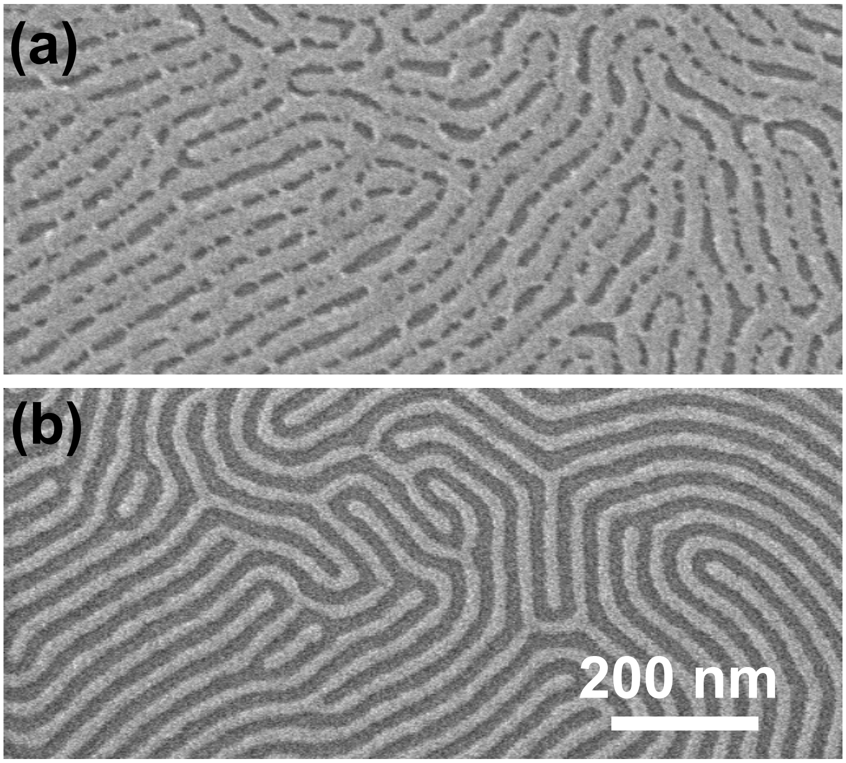

Fig. 2-3 SEM images of PS-PDMS thin film after (a) exposure to an O2 plasma for 1 min; (b) exposure to a CF4 plasma (5 sec) followed by an O2 plasma (1 min.).

2.4 Effect of brush treatments on morphology

To illustrate the role of surface chemistry, Fig. 2-4a, b, c shows the cylinder morphology on three different trench-patterned substrates pre-coated with no brush, a PS-brush, and a PDMS-brush, respectively. The PS-PDMS on bare

Si (Fig. 2-4a) shows a disordered structure with some perpendicular and some in-plane cylinders, which is assumed to result from the strong interaction between the PDMS block and the hydroxyl-terminated polar native oxide surface. Such interactions impede the diffusivity of the polymer on the surface, leading to non-equilibrium morphologies, as found for polybutadiene.[15] On a PS-brush coated substrate (Fig. 2-4b), uniform cylinders form, but the ordering within the trenches is poor. In this case, island formation is observed (for example, at bottom of the figure) since a smaller thickness of polymer is required to form one monolayer of cylinders on a brush composed of the majority component of the diblock copolymer.[15]

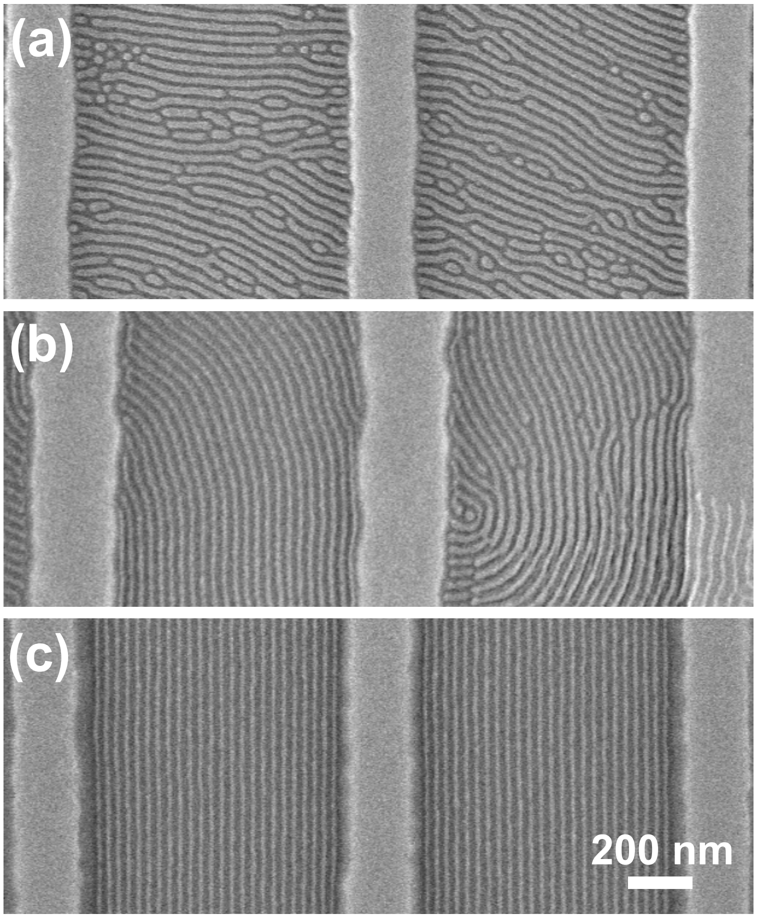

Fig. 2-4 SEM images of PS-PDMS on trench substrates (a) without a brush, (b) with a PS-brush, and (c) with a PDMS brush. The samples were solvent-annealed for 15 hrs.

On a PDMS-brush coated surface (Fig. 2-4c), the degree of ordering of the cylinders within the trenches is markedly improved, and correlation lengths of tens of microns are observed in some trenches. This contradicts the proposal that a brush made of the minority block should have little effect on ordering of a block copolymer in which the minority block preferentially wets the substrate.[15] These remarkable differences are attributed to the extremely low surface energy of the PDMS surface. The flexibility of the Si-O backbone enables the molecules of the brush layer to adsorb on the silica surface presenting their methyl groups upwards.[26] This provides a very low energy barrier for surface diffusion of the PS-PDMS diblock copolymer. These results suggest that a PDMS brush might be also effective for self-organization of other block copolymers.

2.5 Effects of solvent-annealing conditions and template patterns

We will now show how the collective effects of mesa width, solvent vapor pressure and annealing time can be used to control the alignment of cylinders in trenches. In this experiment the period of the topographic patterns was set to 1 μm, and the width ratio of mesa to trench was varied from 0.18 to 1. The solvent vapor pressure was varied by changing the solvent surface area to annealing chamber volume ratio R within the range of 0.3 cm^{-1} (designated condition A) to 0.99 cm^{-1} (condition F). A higher vapor pressure causes the polymer to swell, lowers the glass transition temperature, and facilitates rearrangement of the polymer chains. The effect of R on swelling was evident from the color of the samples, which changed from grey (as-spun) to gold, violet or blue for conditions A – F.

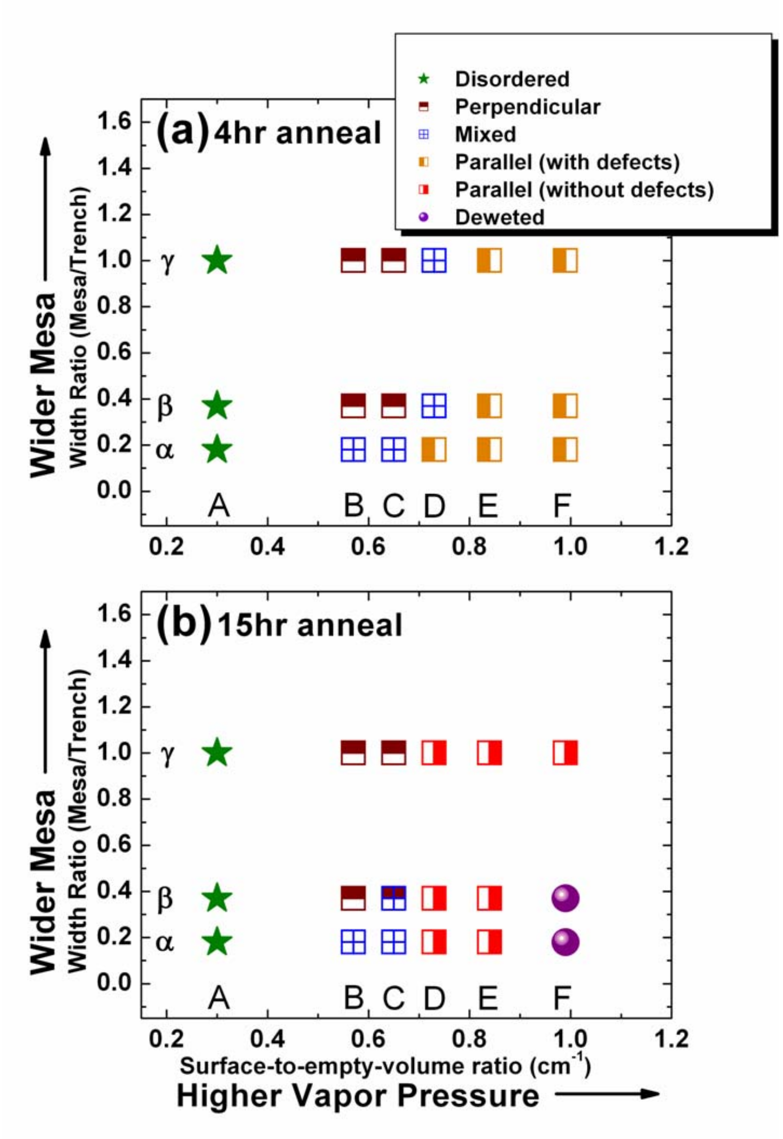

Fig. 2-5 Arrangement of cylinders as a function of mesa/trench width ratio and solvent vapor pressure for (a) tanneal = 4 hours and (b) tanneal = 15 hours. For condition Cβ in (b), both perpendicular and mixed orientations were observed.

Fig. 2-5a and b show systematic trends in the cylinder morphology as a function of solvent vapor pressure R and trench geometry (mesa width/trench width at constant periodicity) for two different annealing times. A low solvent vapor pressure (condition A) gives only disordered cylinders regardless of the trench geometry. In contrast, under a high vapor pressure (condition F), the cylinders align parallel to the trench edges at an early stage of annealing (4 hrs, Fig. 2-5a) but eventually dewet (15 hrs, Fig. 2-5b), particularly for wide trenches (designated α and β). At intermediate vapor pressures the cylinders can align either parallel or perpendicular to the trench edges, and defect levels decrease with increasing annealing time. At condition E, a parallel alignment of cylinders containing defects such as Y-junctions is observed after 4 hrs anneal, while 15 hrs anneal gives virtually defect-free patterns over a large scale substrate (4 cm^2), as shown in Fig. 2-6a, b, c, except near the edge of the sample, where the as-spun film thickness is higher. Cylinders with a width of 16 nm and a period of 34 nm were aligned in each trench. The number of cylinders in each trench depends on its width, for example in Fig. 2-6a, 26 cylinders are visible. This degree of ordering on a macroscopic scale is attributed to the large χ parameter of PS-PDMS and exceptionally low surface energy of the PDMS-brush grafted on the native oxide surface.

The ability to orient cylinders either perpendicular or parallel to the trenches by controlling the trench geometry and annealing conditions is of particular interest in nanolithography applications. Trenches with wide mesas (β and γ) and relatively low vapor pressure annealing (B and C) lead to uniformly or predominantly perpendicular orientation (Fig. 2-6d), despite the higher free energy of the ends of the cylinders. Perpendicular alignment of cylinders in local areas of trenches has been reported and attributed to capillary flow from mesas to trenches, perpendicular to the trench walls.[12] Such a flow will be greater for higher mesa/trench ratios, and this mechanism could account for the observation of perpendicular cylinders only for the higher width ratios β and γ. The perpendicular or mixed orientation is metastable and is gradually replaced by the parallel orientation (see conditions Cβ, Dβ, Dγ) for longer annealing times.

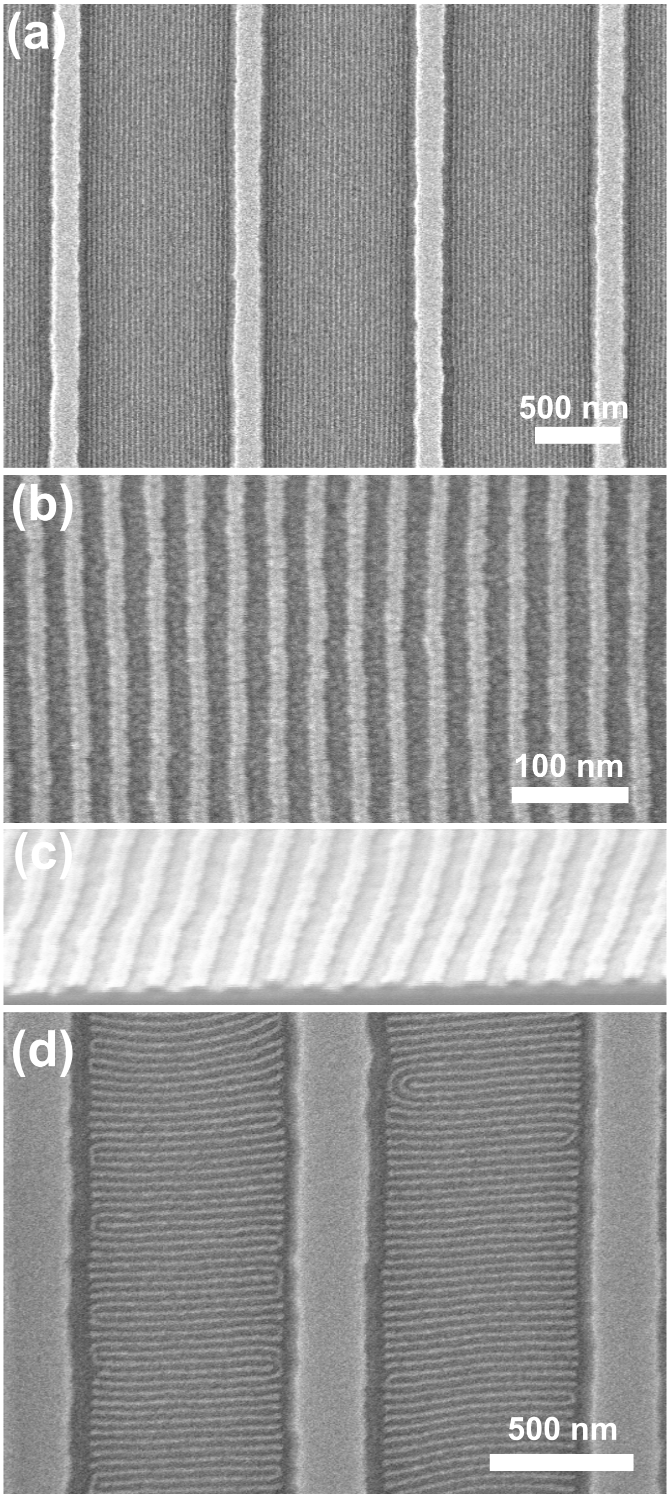

Fig. 2-6 SEM images of (a), (b), (c) parallel cylinders on trench substrates with narrow mesas (W_{mesa}=125nm and W_{trench}=875nm) under a high vapor pressure of toluene (condition Eα from Fig. 2-5) and (d) perpendicular cylinders in a wide-mesa pattern (W_{mesa}=270 nm and W_{trench}=730 nm) at a lower vapor pressure (condition Bβ). The annealing time was 15 hours.

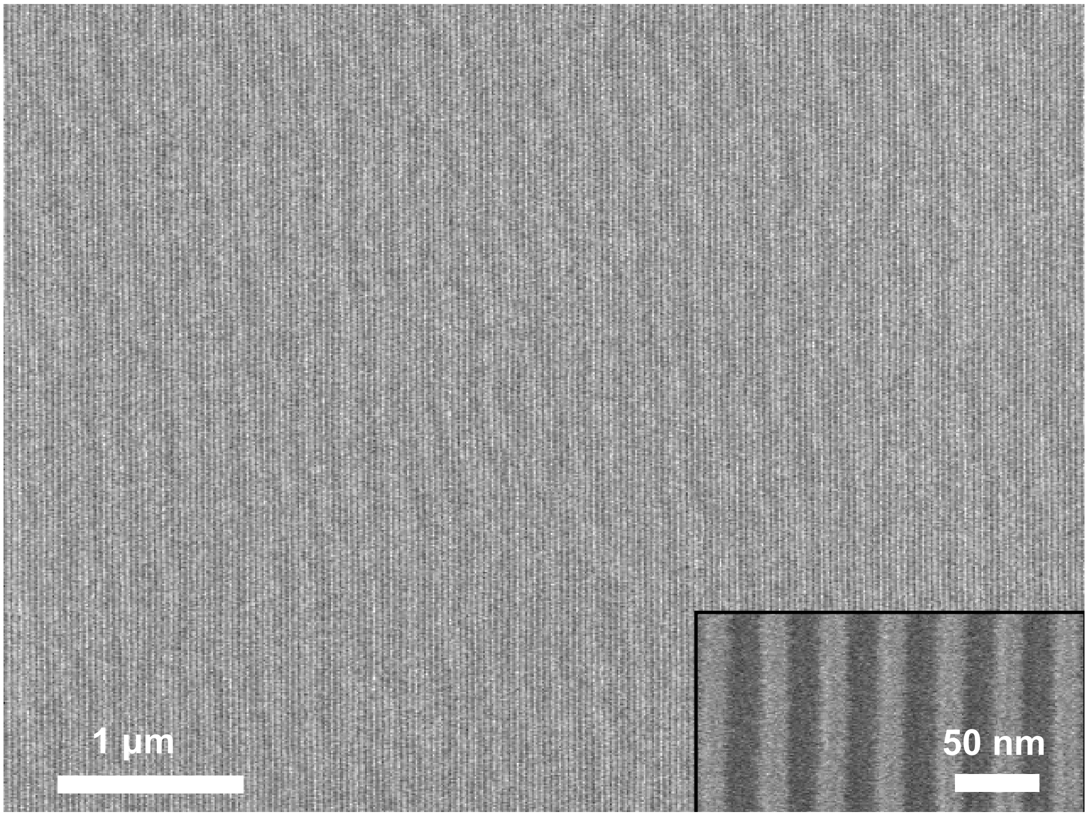

Fig. 2-7 SEM images of cylinders guided by 7μm-wide trenches.

Fig. 2-7 presents SEM images of the self-assembly patterns on a template with a periocity of 7 μm. Thus, the correlation length of this self-assembly is estimated to be at least 7 μm. The measured critical dimension and line edge roughness are 14.2 ± 0.2 nm and 3.2 ± 0.5 nm, respectively. The exceptional degree of long-range ordering and uniformity can be confirmed by the GISAXS analysis in Fig. 2-8, which shows sharp diffraction patterns and high order peaks in the y direction. The linearity of the diffraction patterns and the absence of separate spots in the z direction confirm the uniform monolayer formation over the incident beam area. The calculated periodicity of the patterns from the GISAXS result is around 34 nm, which is consistent with the value measured with the SEM images. The diffraction patterns from the 1 µm-period trench patterns occurring at near $q_y=0$ were screened by a beam blocker.

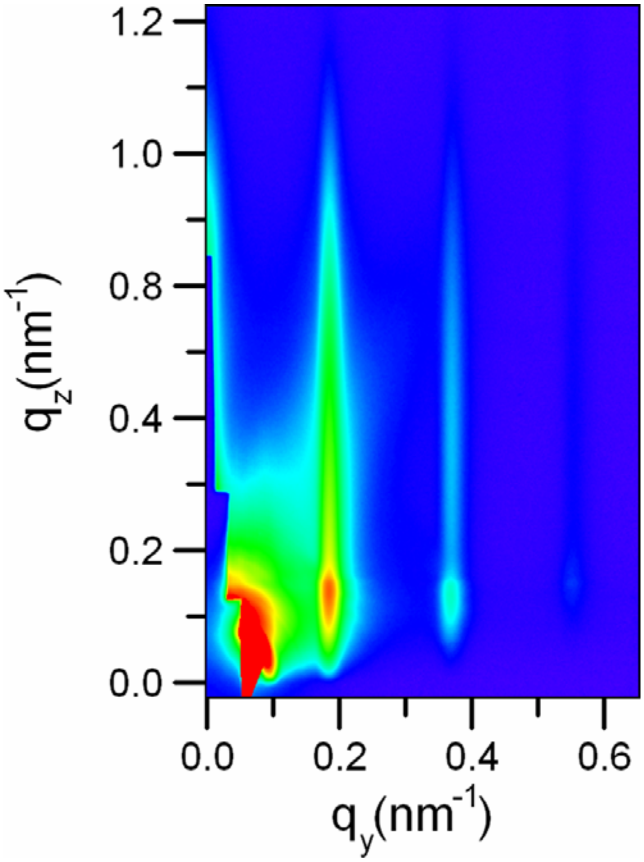

Fig. 2-8 Grazing incidence small-angle X-ray scattering patterns of cylinders.

2.6 Summary

A PS-PDMS block copolymer has been investigated for applications in self-assembled nanolithography. This material combines the advantages of a high χ parameter, leading to well-ordered structures with low edge roughness, and a high etch selectivity between the two blocks, providing etch-resistant masks for pattern transfer. A topographical PDMS-brush coated silica surface can be used to template in-plane cylinder arrays with long range order. Moreover, the cylinder arrays may be selectively oriented parallel or perpendicular to the trench walls by control of solvent annealing and mesa width. These well-controlled nanoscale PDMS patterns may have a variety of applications in the fabrication of narrow interconnect lines, nanoimprint lithography stamps, or nano-fluidic devices.

References

[1] S. Y. Chou, P. R. Krauss, W. Zhang, L. J. Guo, L. Zhuang, "Sub-10 nm imprint lithography and applications", *Journal of Vacuum Science & Technology B 15*, p. 2897 (1997)

[2] R. D. Piner, J. Zhu, F. Xu, S. H. Hong, C. A. Mirkin, ""Dip-pen" nanolithography", *Science 283*, p. 661 (1999)

[3] F. S. Bates, G. H. Fredrickson, "Block Copolymer Thermodynamics - Theory and Experiment", *Annual Review of Physical Chemistry 41*, p. 525 (1990)

[4] J. Y. Cheng, C. A. Ross, V. Z. H. Chan, E. L. Thomas, R. G. H. Lammertink, G. J. Vancso, "Formation of a cobalt magnetic dot array via block copolymer lithography", *Advanced Materials 13*, p. 1174 (2001)

[5] J. Y. Cheng, C. A. Ross, H. I. Smith, E. L. Thomas, "Templated self-assembly of block copolymers: Top-down helps bottom-up", *Advanced Materials 18,* p. 2505 (2006)

[6] M. Park, C. Harrison, P. M. Chaikin, R. A. Register, D. H. Adamson, "Block copolymer lithography: Periodic arrays of similar to 10(11) holes in 1 square centimeter", *Science 276*, p. 1401 (1997)

[7] D. A. Vega, C. K. Harrison, D. E. Angelescu, M. L. Trawick, D. A. Huse, P. M. Chaikin, R. A. Register, "Ordering mechanisms in two-dimensional sphere-forming block copolymers", *Physical Review E 71*, p. 061803 (2005)

[8] S. H. Kim, M. J. Misner, T. P. Russell, "Solvent-induced ordering in thin film diblock copolymer/homopolymer mixtures", *Advanced Materials 16,* p. 2119 (2004)

[9] T. Thurn-Albrecht, J. Schotter, C. A. Kastle, N. Emley, T. Shibauchi, L. Krusin-Elbaum, K. Guarini, C. T. Black, M. T. Tuominen, T. P. Russell, "Ultrahigh-density nanowire arrays grown in self-assembled diblock copolymer templates", *Science 290,* p. 2126 (2000)

[10] C. T. Black, "Self-aligned self assembly of multi-nanowire silicon field effect transistors", *Applied Physics Letters 87*, p.163116 (2005)

[11] C. T. Black, O. Bezencenet, "Nanometer-scale pattern registration and alignment by directed diblock copolymer self-assembly", *IEEE Transactions on Nanotechnology 3*, p. 412 (2004)

[12] D. Sundrani, S. B. Darling, S. J. Sibener, "Hierarchical assembly and compliance of aligned nanoscale polymer cylinders in confinement", *Langmuir 20*, p. 5091 (2004)

[13] S. O. Kim, H. H. Solak, M. P. Stoykovich, N. J. Ferrier, J. J. de Pablo, P. F. Nealey, "Epitaxial self-assembly of block copolymers on lithographically defined nanopatterned substrates", *Nature 424*, p. 411 (2003)

[14] M. P. Stoykovich, M. Muller, S. O. Kim, H. H. Solak, E. W. Edwards, J. J. de Pablo, P. F. Nealey, "Directed assembly of block copolymer blends into nonregular device-oriented structures", *Science 308,* p. 1442 (2005)

[15] C. Harrison, P. M. Chaikin, D. A. Huse, R. A. Register, D. H. Adamson, A. Daniel, E. Huang, P. Mansky, T. P. Russell, C. J. Hawker, D. A. Egolf, I. V. Melnikov, E. Bodenschatz, "Reducing substrate pinning of block copolymer

microdomains with a buffer layer of polymer brushes", *Macromolecules 33*, p. 857 (2000)

[16] T. L. Bucholz, Y. L. Loo, "Phase behavior of near-monodisperse semifluorinated diblock copolymers by atom transfer radical polymerization", *Macromolecules 39*, p. 6075 (2006)

[17] H. Frielinghaus, N. Hermsdorf, K. Almdal, K. Mortensen, L. Messe, L. Corvazier, J. P. A. Fairclough, A. J. Ryan, P. D. Olmsted, I. W. Hamley, "Micro- vs. macro-phase separation in binary blends of poly(styrene)-poly(isoprene) and poly(isoprene)-poly(ethylene oxide) diblock copolymers", *Europhysics Letters 53*, p. 680 (2001)

[18] M. R. Hammond, E. Cochran, G. H. Fredrickson, E. J. Kramer, "Temperature dependence of order, disorder, and defects in laterally confined diblock copolymer cylinder monolayers", *Macromolecules 38*, p. 6575 (2005)

[19] Y. Ren, T. P. Lodge, M. A. Hillmyer, "Synthesis, characterization, and interaction strengths of difluorocarbene-modified polystyrene-polyisoprene block copolymers", *Macromolecules 33*, p. 866 (2000)

[20] J. Bang, S. H. Kim, E. Drockenmuller, M. J. Misner, T. P. Russell, C. J. Hawker, "Defect-free nanoporous thin films from ABC triblock copolymers", *Journal of the American Chemical Society 128*, p. 7622 (2006)

[21] M. A. Unger, H. P. Chou, T. Thorsen, A. Scherer, S. R. Quake, "Monolithic microfabricated valves and pumps by multilayer soft lithography", *Science 288*, p. 113 (2000)

[22] J. H. Chu, P. Rangarajan, J. L. Adams, R. A. Register, "Morphologies of Strongly Segregated Polystyrene-Poly(Dimethylsiloxane) Diblock Copolymers", *Polymer 36*, p. 1569 (1995)

[23] C. Z. Chuai, S. Li, K. Almdal, J. Alstrup, J. Lyngaae-Jorgensen, "Influence of diblock copolymer on the morphology and properties of polystyrene/poly(dimethylsiloxane) blends", *Journal of Applied Polymer Science 92*, p. 2747 (2004)

[24] C. M. Chan, Polymer Surface Modification and characterzation, 1st ed., Hanser Publishers (1994)

[25] S. P. Gido, D. W. Schwark, E. L. Thomas, M. D. Goncalves, "Observation of a Nonconstant Mean-Curvature Interface in an Abc Triblock Copolymer", *Macromolecules 26*, p. 2636 (1993)

[26] S. J. Clarson, J. A. Semlyen, Siloxane Polymers, *PTR Prentice Hall, Inc.* (1993)

Chapter 3

Solvent vapor induced tunability of self-assembled block copolymer patterns

3.1 Introduction

This chapter deals with the systematic tunability of pattern dimension and morphology in a microphase separated block copolymer by controlling the solvent-annealing conditions, where the key parameters are solvent vapor pressure and the mixing ratio of selective and partially selective solvent vapors. Vapor pressure can control the degree of solvent uptake in the film, which changes both the chain mobility and the interfacial interaction between the two blocks. This thesis also proposes a theoretical model to explain the increase of pattern period with a decrease in vapor pressure. It was recently reported that a change in the effective volume fraction can be accomplished using selective and nonselective vapors.[1, 2] Independent control of both the pattern width and the periodicity by using a mixed vapor of a selective (heptane) and a partially selective (toluene) solvent will be shown. It will be also demonstrated that a cylinder-forming BCP can be transformed to a perforated lamellar structure by increasing the portion of selective solvent in the vapor. This study suggests a way to relieve the constraints on the achievable microdomain pattern geometries imposed by the molecular structure of the BCP.

Well-controlled monolayer patterns of block copolymer (BCP) microdomains have been pursued widely for applications in sub-30 nm nanolithography.[3-13]

BCP film processing is scalable and low cost, and is compatible with existing semiconductor fabrication techniques. Diblock copolymers with a molecular weight of a few tens to a few hundreds kg/mol spontaneously form periodic arrays of well-defined nanoscale features such as dots, holes and lines, which can be used as masks for fabrication of arrays of nanoscale functional features after the selective elimination of one block.[3-5, 13] Long-range ordering and positional registration of the features can be imposed by using chemical or topographical templates.[6, 14-16] The morphology of the patterns can be further diversified by using multi-block copolymers or employing various confinement geometries.[8, 13, 17, 18] The morphology and length scale of the microdomain arrays in BCPs are governed by the degree of polymerization of each block [19, 20], and thus to obtain different geometries and feature sizes, polymers with different chain lengths or BCP/homopolymer blends have been employed.[21] However, in terms of device fabrication, it would be advantageous to be able to manipulate the shape and dimensions of the features formed from a single BCP simply by altering the processing conditions.

Polymeric materials often provide an exceptional degree of controllability in their molecular configurations due to their weak intermolecular forces which are largely based on Van der Waals interactions. Solvent vapor annealing, which has been employed to provide high chain flexibility to BCPs and to promote self-assembly into the microphase-separated state [2, 6, 13, 22-25], can be an effective lever to engineer the resulting structures. It has been shown that treatments with selective or nonselective vapor resulted in different morphologies or different orientations, demonstrating solvent-induced controllability.[1, 2, 26] However, precise adjustment of pattern size and morphology using controlled mixed solvent vapors has not been studied so far.

3.2 Experimental

A cylinder-forming PS-PDMS block copolymer (Polymer Source, Inc.) with total molecular weight of 45.5 kg/mol and nominal volume fraction of PDMS, f_{DMS} = 33.5% was used. Substrates patterned with 40-nm deep trenches with a periodicity of 1.3μm were fabricated using a Lloyd's Mirror interference lithography system with a 325 nm wavelength He-Cd laser. The laser exposed grating patterns into a 200 nm thick PFI-88 photoresist (Sumitomo Chemical Co.), which were transferred into the Si substrate by a 10 mTorr CF_4 reactive ion etching. The native oxide surfaces were treated by hydroxy-terminated PDMS homopolymer with molecular weight 5kg/mol, which was spun-cast on the substrates and annealed at 150 °C for 15 hours, then washed with toluene to remove unattached polymers. The thickness of the grafted brush layer was estimated to be around 3-4 nm by ellipsometry. BCP thin films with a thickness of 30 nm were obtained by spin-casting toluene solutions of 1.5% by weight of the block copolymer on the substrates, then the samples were solvent-annealed under toluene or toluene/heptane vapor at room temperature for three hours. The vapor pressure of the solvent was controlled via the ratio between the surface area of the liquid solvent and the empty volume of the annealing chamber.[13] The annealed film was treated with a 5 sec, 50 W CF_4 plasma followed by a 22 sec, 90 W O_2 plasma to remove the PDMS surface layer and selectively eliminate the PS block, resulting in oxidized PDMS microdomains in the trenches. The surface morphology was observed using a Zeiss/Leo Gemini 982 scanning electron microscope (SEM) operated with an acceleration voltage of 5 kV. A thin layer of Au-Pd alloy was sputter-coated on the samples in order to avoid charging effects.

3.3 Effect of solvent vapor pressure

The effect of solvent vapor pressure on the morphology of the cylinder patterns is considered first. The vapor pressure is characterized by the ratio between the surface area (S) of a beaker of the solvent placed in the solvent-annealing chamber and the volume (V) of the air (at atmospheric pressure) in the chamber that mixes with the solvent vapor. The chamber has a small leak path through which solvent vapor escapes. The amount of solvent vapor in the chamber is determined by three flux components: evaporation from the solvent surface (F_1), condensation into the solvent surface (F_2), and the leak flow (F_3). At steady state, the concentration (C) of solvent vapor in the chamber is given by

$$C = \frac{a_0(F_1 - F_2 - F_3)}{V} = \frac{a_1 S - a_2 S \cdot C - a_3 \cdot C}{V} = \frac{a_1 S}{a_2 S + a_3 + V}, \qquad (1)$$

where a_0-a_3 are proportionality constants. Eq. 1 shows that there is an inverse proportionality between the vapor pressure and the air volume. Thus, to identify the effects of vapor pressure, in our experiments the solvent surface area was fixed at 5.16 cm^2 and the air volume was changed from 5.3 cm^3 to 9.0 cm^3.

Figure 3-1 presents scanning electron microscopy (SEM) images of oxidized PDMS patterns as a function of S/V, and Figure 3-2 shows the change in the period, linewidth and filling factor (linewidth/period) of the PDMS cylinders. The PS-PDMS was templated in shallow grooves, and the cylinders form well ordered parallel arrays. The pattern period decreases from 38.6 to 32.3 nm, a change of 19.5%, as the vapor pressure increases (S/V increases from 0.57 to 0.97 cm^{-1}), and the linewidth decreases from 24.2 nm to 11.4 nm, a change of 112%. The majority of the change occurs in the lower vapor pressure regime (S/V = 0.57 - 0.70). Changes in the pattern dimensions are consistent with other observations of variations in domain spacing with changes in vapor pressure[27] or with the concentration of polymer in solution.[28] Due to the screening effect of the solvent molecules, the effective Flory-Huggins interaction parameter (χ_{eff}) is reduced as the volume fraction (f_s) of solvent in the film increases:[20, 28]

$$\chi_{eff} = \chi(1 - f_s), \tag{2}$$

where χ is the interaction parameter in the absence of solvent uptake. Thus, solvent uptake in BCP films decreases the effective segregation strength $\chi_{eff}N$, where N is the degree of polymerization, and consequently affects the equilibrium domain spacing.

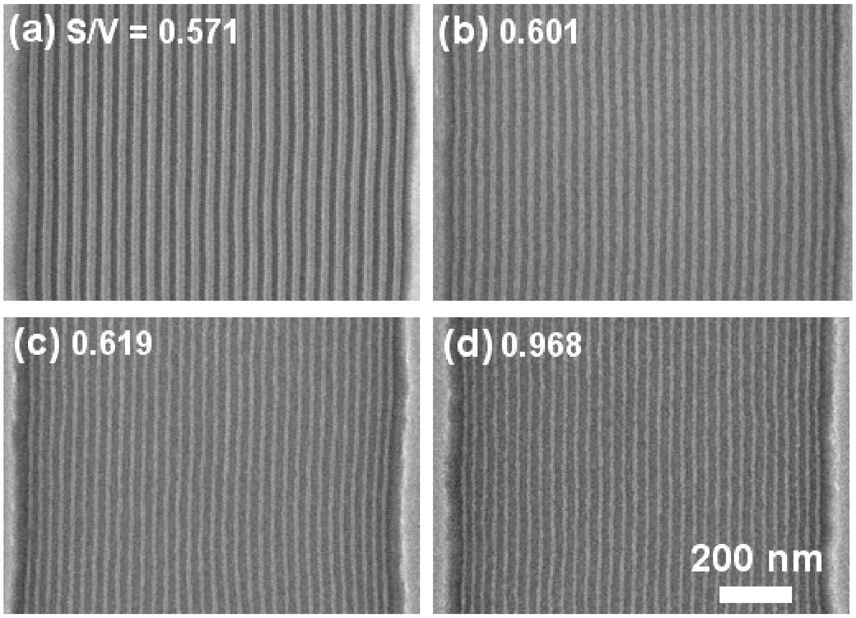

Fig. 3-1 Scanning electron micrographs of the cylinder-forming PS-PDMS block copolymer after solvent-annealing and reactive ion etching to remove PS. Linear patterns with various period and linewidth were obtained with different toluene vapor pressure conditions. The solvent vapor pressure was varied by changing the ratio of solvent surface area (S) to the annealing chamber volume (V). The S/V ratios are (b) 0.571, (c) 0.601, (d) 0.619, and (e) 0.968 cm^{-1}, respectively.

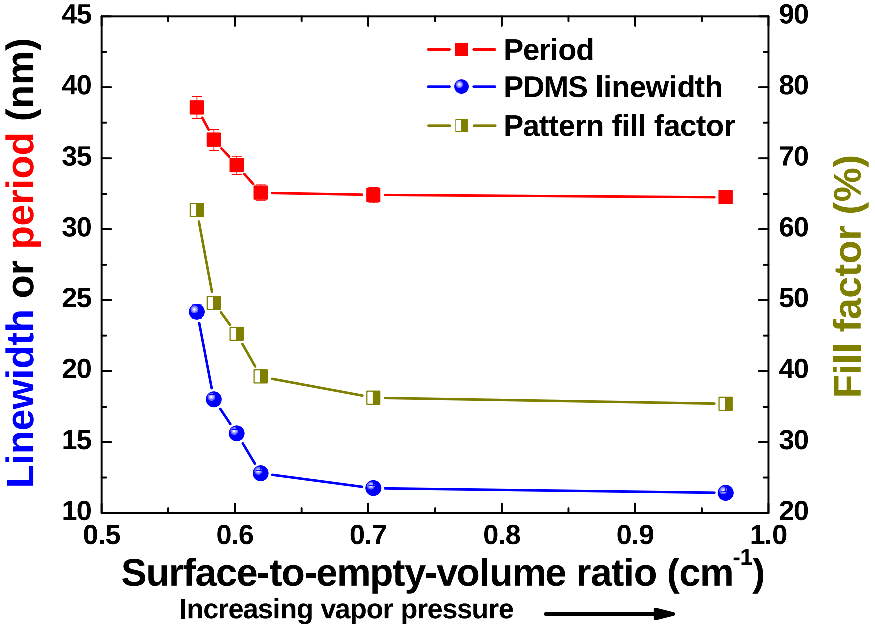

Fig. 3-2 Measured period, fill factor, and linewidth of each pattern as a function of S/V.

The total free energy of a block copolymer includes the interfacial energy and the chain conformational energy in the strong segregation limit. Thus, the equilibrium spacing λ_{eq} can be determined by differentiating the total Gibbs free energy with respect to the period λ and equating this to zero. The reference state, wherein the free energy is zero, is the macrophase-separated homopolymers without interfaces between the different polymer blocks, or stretching of the chains. The decrease of conformational entropy upon stretching of a polymer is proportional to the square of strain: [9, 29-32]

$$\Delta S = -\frac{k}{2}(\alpha_x^2 + \alpha_y^2 + \alpha_z^2 - 3) = -\frac{k}{2}(\alpha_x^2 + \frac{2}{\alpha_x} - 3) = -\frac{k}{2}[(\frac{\lambda}{\lambda_0})^2 + 2(\frac{\lambda_0}{\lambda}) - 3] \qquad (3)$$

where k is the Boltzmann constant, α_x, α_y, and α_z denote the extension ratios in the x, y, and z directions, and λ_0 and λ indicate the domain spacing for relaxed and perturbed chains, respectively. Incompressibility of the polymer is assumed, so $\alpha_x \alpha_y \alpha_z = 1$.

The total Gibbs free energy change per chain, ΔG can be expressed as a function of λ:

$$\Delta G(\lambda) = \Delta H - T\Delta S = \gamma\Sigma + \frac{1}{2}kT[(\frac{\lambda}{\lambda_0})^2 + 2(\frac{\lambda_0}{\lambda}) - 3] \tag{4}$$

where γ denotes the interfacial energy/unit area and Σ the contact area per chain between the two blocks. By using the relations that the volume per chain= $Ma^3 = \frac{\lambda}{2}\Sigma$, where *a* is the Kuhn step size and M is the total number of Kuhn segments, χ_{eff} is the effective Flory-Huggins interaction parameter, $\gamma = \frac{kT}{a^2}\sqrt{\frac{\chi_{eff}}{6}}$, obtained from the Helfand-Tagami expression for the interfacial energy between A and B homopolymers,[20] and $\lambda_0 = 2aM^{1/2}$, which is twice the end-to-end distance of a Gaussian chain, and following the Alexander-de Gennes formalism,[32] the overall free energy has the following form as a function of λ:

$$\Delta G(\lambda) = \frac{kT}{a^2}\sqrt{\frac{\chi_{eff}}{6}} \cdot 2Ma^3 \cdot \frac{1}{\lambda} + \frac{1}{2}kT \cdot [\frac{\lambda^2}{4Ma^2} + \frac{4\sqrt{Ma^2}}{\lambda} - 3] \tag{5}$$

When χ is zero, the chains are fully relaxed with the maximum conformational entropy, and λ equals λ_0 (= $2aM^{1/2}$, twice the end-to-end distance of a Gaussian chain since one period is composed of two polymer chains). As χ increases, the conformational structure becomes more perturbed and λ increases. The equilibrium spacing λ_{eq} can be determined by differentiating eq. 3 with respect to λ and equating it to zero. In the strong segregation limit (high χ), this leads to the result that chains are 10-40% stretched by microphase separation compared to the relaxed state due to the unfavorable contacts between different blocks,[32, 33] and, in the limit of high χ, the $1/\lambda$ component of the strain energy term is small and $\lambda_{eq} \sim a\chi^{1/6}N^{2/3}$.

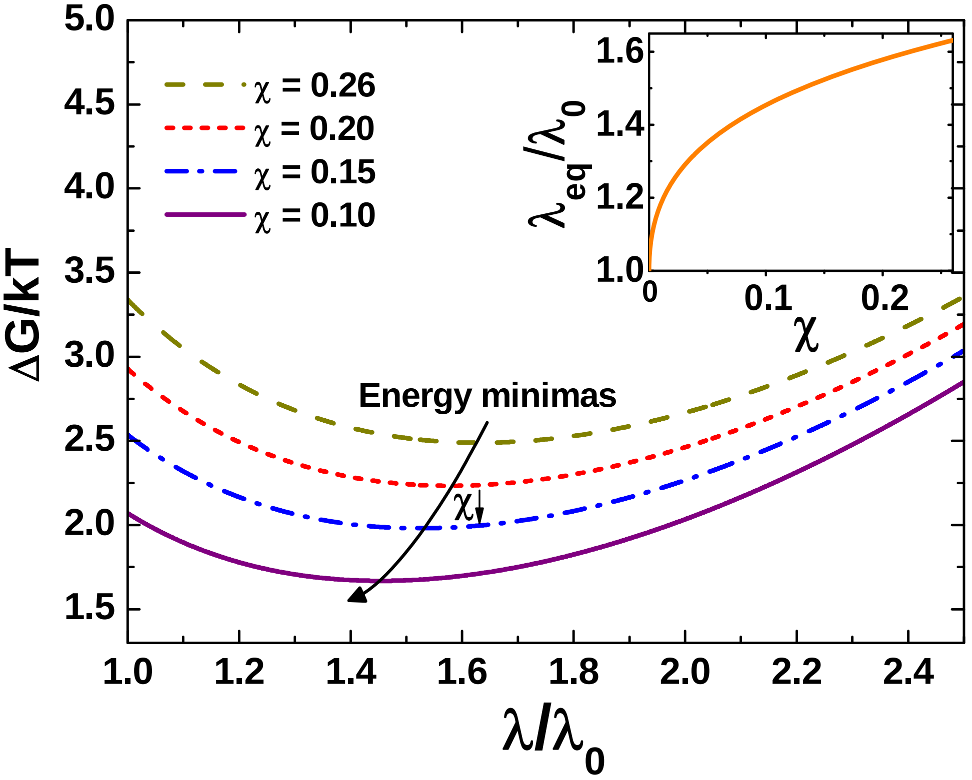

Fig. 3-3 Calculated free energy curves with different χ parameters. The inset shows the change of equilibrium domain spacing with χ.

Figure 3-3 shows the shift of the free energy curves towards a larger domain spacing with an increase of χ, and the inset presents the calculated dependence of λ_{eq} on χ. By increasing the domain spacing at higher χ and, as a result, decreasing the interfacial area per chain, the interfacial energy can be reduced at the expense of increased strain energy (stemming from decreased conformational entropy). This free energy model explains the decrease of pattern period with an increase of solvent vapor pressure during annealing.

Figure 3-2 also shows that the pattern filling factor varies from 62.7% to 35.4% as S/V increases from 0.57 to 0.97, which indicates that the PDMS linewidth decreases faster than the period does with increasing solvent vapor pressure. This can be attributed to the fact that toluene is a partially selective solvent for the PS block. Although PDMS also dissolves well in toluene, there is a larger solubility parameter difference ($|\delta_{tol} - \delta_{PDMS}| = |18.2 - 15.5| = 2.7$ MPa$^{1/2}$) between PDMS and toluene compared to that ($|\delta_{tol} - \delta_{PS}| = |18.2 - 18.5| = 0.3$ MPa$^{1/2}$) between PS and toluene.[34] Thus, the author expects that the toluene provides a higher degree of swelling to PS than to PDMS. It should also be noted that the density of defects such as Y junctions increases as the vapor pressure goes down due to reduced chain mobility.

3.4 Effects of mixed solvent vapors

While the results in Figs. 3-1 and 3-2 demonstrate the ability to manipulate pattern period and linewidth, the two dimensions cannot be varied independently. A method to break the correlation by using a mixed solvent is introduced here. Heptane ($\delta_{hep} = 15.3$ MPa$^{1/2}$) is a good solvent for PDMS but a poor solvent for PS.[34] The SEM images in Fig. 3-3 and the measurements in Fig. 3-5 show the variation of the period, linewidth and filling factor with the ratio of liquid toluene:heptane (T/H) at a fixed surface-to-volume ratio in the chamber (S/V = 0.62). For T/H greater than 3, the PDMS forms parallel cylinders with little variation in period, but with a systematic change in linewidth and filling factor. The increase of linewidth with the fraction of heptane in the vapor is a result of the selective increase of the effective PDMS volume fraction by heptane, and the very small variation of pattern periodicity can be explained as a tradeoff between the shrinking of the PS domains and the expansion of the PDMS domains. As a result, an increase of heptane volume fraction in the solvent from 0 to 25% leads to a linewidth increase of 54%, from 12.8 to 19.7 nm, without an appreciable change in period. These results suggest a convenient way to fabricate line patterns with desired period and linewidth. First, an appropriate vapor pressure condition can be determined for the chosen period, then a specific line width can be obtained by treating the polymer film with vapor of the proper heptane/toluene ratio. A larger defect density for a higher fraction of heptane was observed and can be understood from decreased chain mobility of the majority block, PS.

The morphology shows a striking change as the fraction of heptane increases further (T/H < 3). Figure 3-4 presents the evolution of the PDMS domain geometry from cylinders to perforated lamellae, and eventually to a disorganized morphology as the fraction of heptane (and consequently the effective volume fraction of PDMS) increases. Hexagonally perforated lamellar phases, where the minority block forms a lamella with regularly arranged holes with a six-fold symmetry, have been reported for BCPs with a volume fraction range between those corresponding to cylinder and lamellar phases, for example, triblock copolymer thin films such as poly(styrene-b-butadiene-b-styrene) or poly(styrene-b-2-vinylpyridine-b-t-butyl methacrylate), and poly(styrene-b-methyl methacrylate) diblock copolymer thin films.[27, 35, 36] It was also reported that a transition from lamellae to perforated lamellae can be induced by selectively swelling the polyethylene oxide block in a poly(ethylene oxide-b-methyl methacrylate-b-styrene) triblock copolymer film.[1] However, the poor etch-selectivity or the formation of multiple lamellae make these examples less useful for lithographic applications.

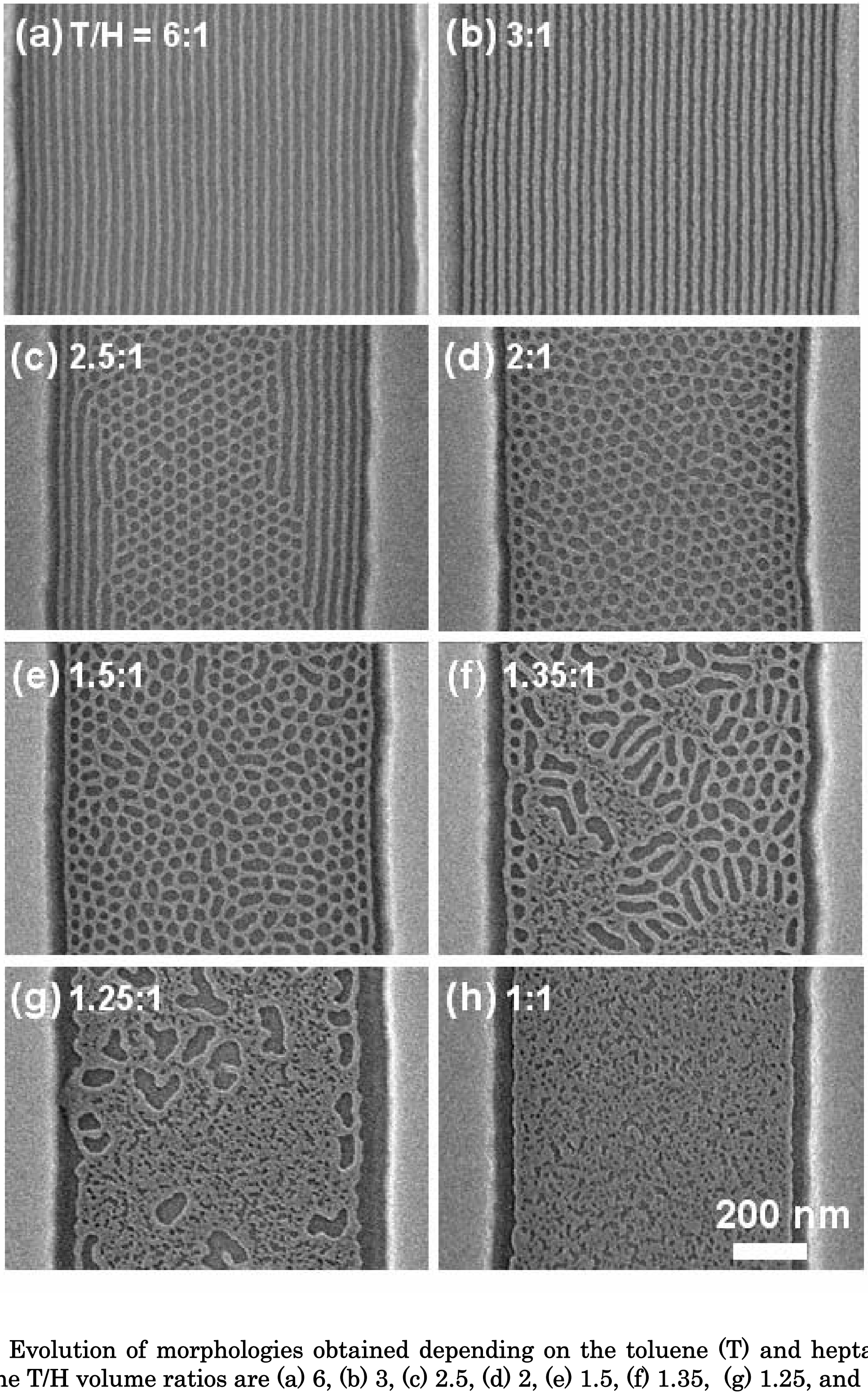

Fig. 3-4 Evolution of morphologies obtained depending on the toluene (T) and heptane (H) ratio. The T/H volume ratios are (a) 6, (b) 3, (c) 2.5, (d) 2, (e) 1.5, (f) 1.35, (g) 1.25, and (h) 1.

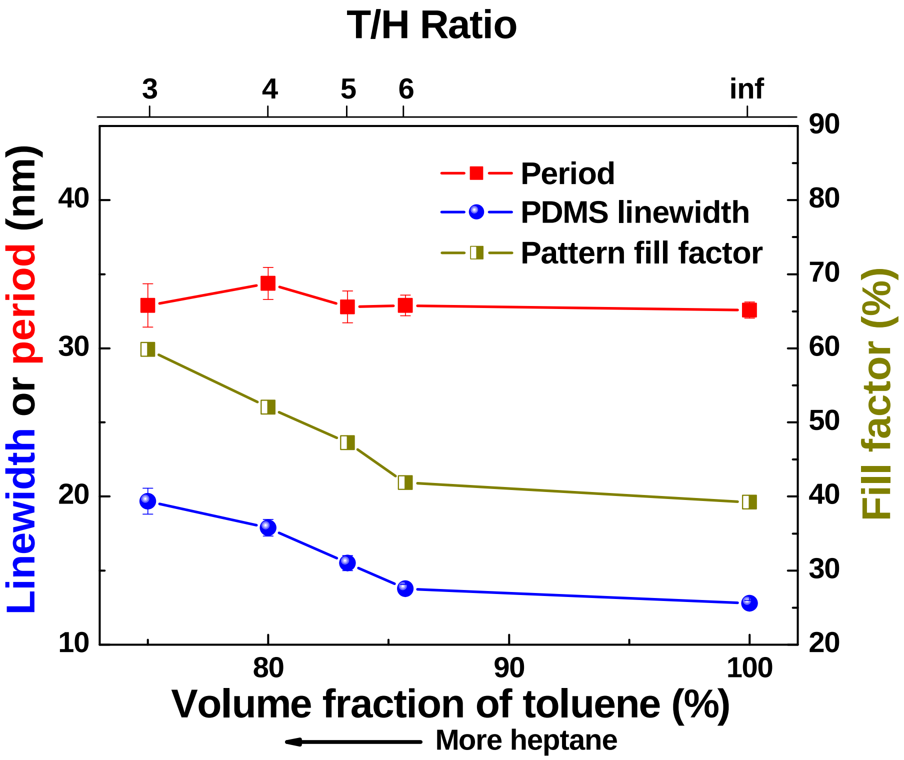

Fig. 3-5 Measured period, fill factor, and linewidth of patterns obtained with different toluene (T) and heptane (H) mixing ratios. The volume fraction of toluene was calculated as T/(T+H).

The mixed morphology of cylinders and perforated lamellae seen at T/H = 2.5 (Fig. 3-4c) suggests the possibility of forming mixed morphologies controllably in a single annealing step. It is likely that the shallow steps in the substrate stabilise the parallel cylinders, while the perforated lamella forms at the center of the substrate trench. The most uniform perforated lamellar structure was obtained at T/H = 2. At higher heptane ratios (T/H < 1.5), the size and period of the perforations increases and the structure becomes disorganized. Further studies using a variety of solvents may bring additional opportunities to tune the microphase-separated structures.

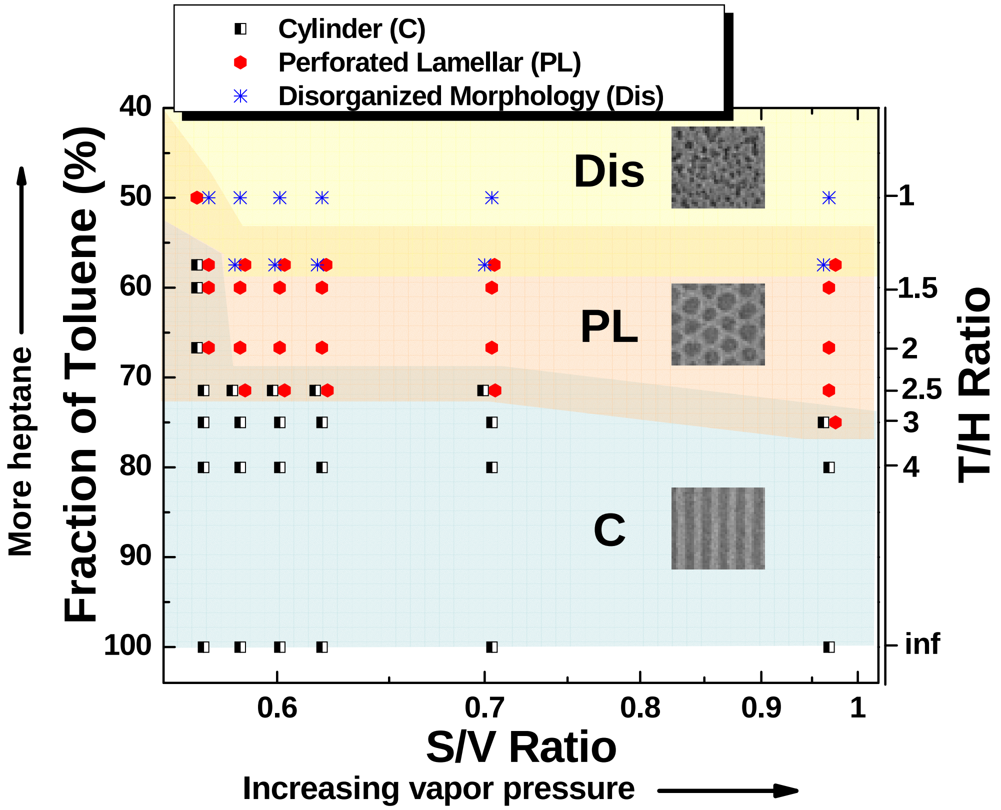

Fig. 3-6 A phase diagram of morphologies obtained with various solvent mixing ratios and vapor pressure. A perforated lamellar structure was obtained at T/H = 2.

The different morphologies obtained with various T/H and S/V ratios are presented as a phase diagram in Fig. 3-6. As expected, the dominant factor controlling the morphology is the toluene fraction. For every S/V ratio, the morphology shows a similar evolution from cylinders, through perforated lamellae, to a disorganized structure, as shown in Fig. 3-4. However, the morphology is also influenced slightly by vapor pressure. At the lowest vapor pressure condition (S/V = 0.53), cylindrical morphologies are observed even with a relatively high heptane fraction, but at higher S/V perforated lamellar or poorly ordered morphologies occur. These results suggest that a higher vapor pressure at a fixed T/H ratio slightly increases the effective volume fraction of PDMS. This can be explained from the partly selective and selective characters of toluene and heptane, respectively. In general, the majority of toluene molecules interact with PS due to a smaller energy penalty. However, as the degree of swelling increases, an entropic effect resulting from the stretching of PS may drive more toluene molecules into the PDMS block and therefore make toluene a less selective solvent, which is consistent with the saturated fill factor at the high vapor pressure range (S/V >0.7) shown in Fig. 3-2. On the other hand, the highly selective nature of heptane enhances the effective volume fraction of PDMS as the vapor pressure increases. Thus, the effective volume fraction of PDMS is expected to be slightly increased as the total vapor pressure of a mixed vapor increases.

The influence of vapor pressure on the ordering of the perforated lamellar structure was investigated at a fixed solvent ratio of T/H = 2. Figure 3-7 demonstrates the change in the degree of ordering of the perforations depending on the vapor pressure. The ordering can be much improved by lowering the vapor pressure, which is attributed to a larger effective interaction parameter (χ_{eff}) and consequently a higher thermodynamic driving force for microphase separation and ordering. On the other hand, if the vapor pressure is too low (Fig. 3-7a), the chain mobility may not be enough to reach an equilibrium state during three hours of solvent annealing. The best ordering was acquired for the intermediate vapor pressure conditions (S/V= 0.585 ~ 0.601), although a low level of local defects is still present. The most common defects are missing bridges between neighboring pores.

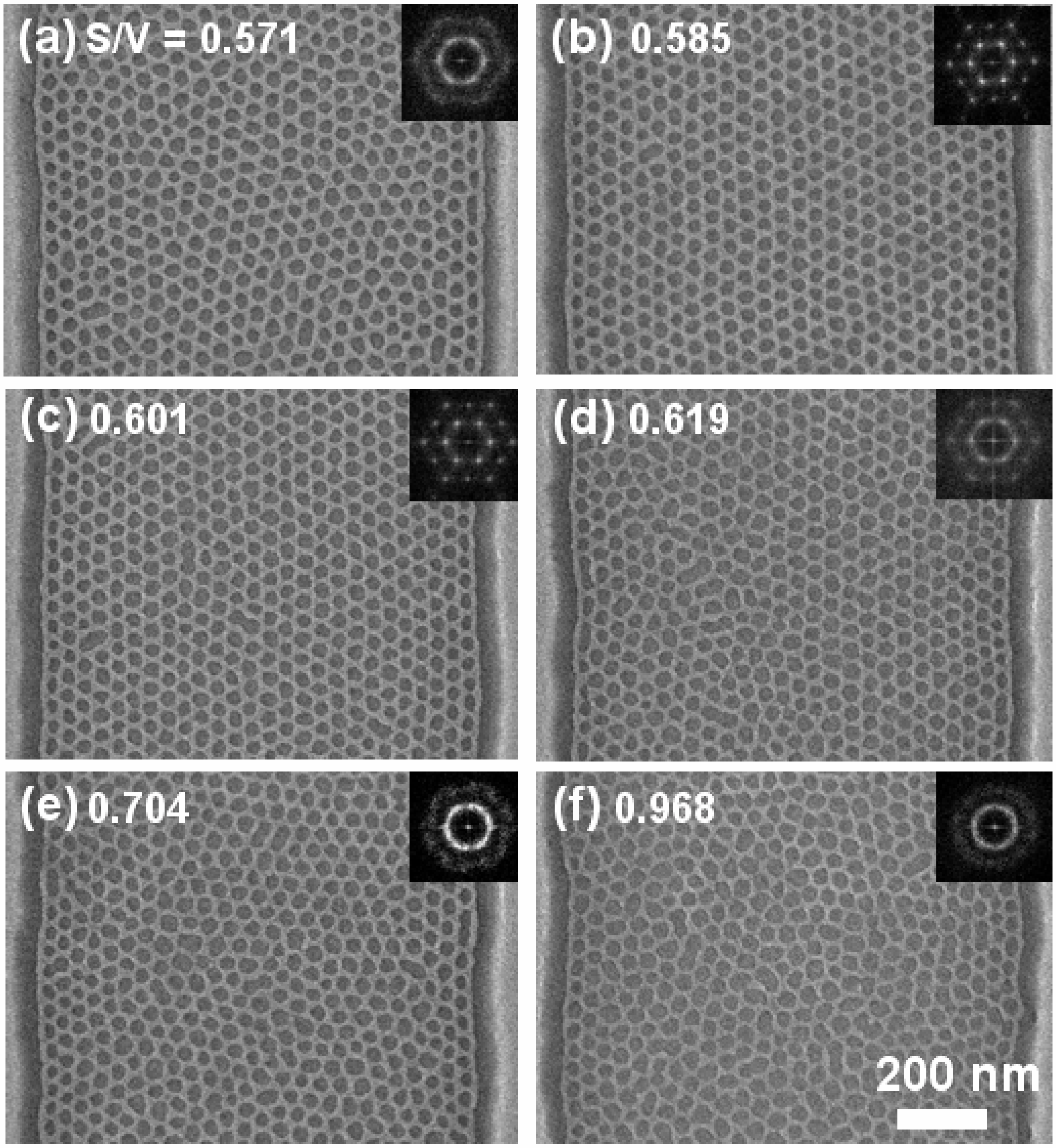

Fig. 3-7 Perforated lamellar morphologies annealed at various vapor pressures. The S/V ratios are (a) 0.571, (b) 0.585, (c) 0.601, (d) 0.619, (e) 0.704, and (f) 0.968, respectively. The insets show fast Fourier transforms. The best ordering was obtained with S/V = 0.585 ~ 0.601 cm^{-1}.

Figure 3-8 shows a larger area of well ordered pattern at S/V = 0.585. The average center-to-center spacing and the pore diameter are 44.8 ± 3.1 nm and 31.7 ± 2.1 nm, respectively. The size distributions are provided as histograms in Fig. 3-9. The closest-packed orientation is parallel with the trench walls, which is analogous to an arrangement of hexagonally ordered spherical BCP domains in one-dimensional trenches.[37]

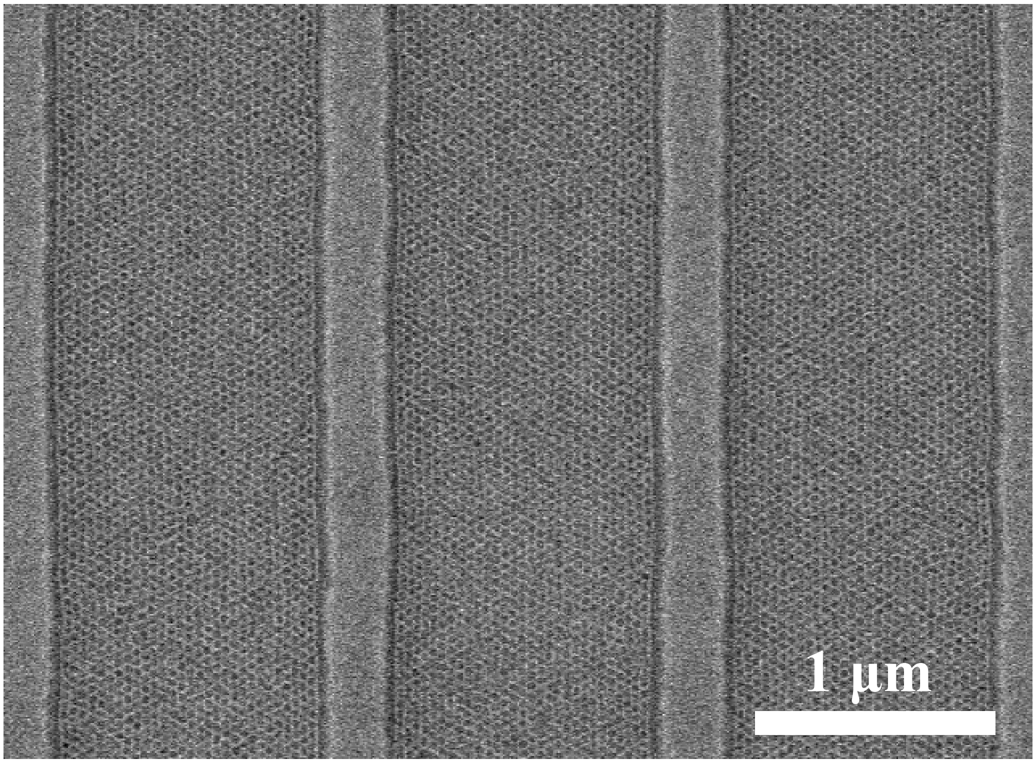

Fig. 3-8 A lower magnification image of perforated lamellar morphology at S/V = 0.585.

Nanoporous patterns, which are useful for making hole arrays by etching or dots through a lift-off process, are usually made by orienting cylindrical BCP domains perpendicularly to a substrate with neutral interfaces and selectively removing the cylinders.[4, 38] The formation of templated nanoporous patterns in PS-PDMS by the use of mixed solvent annealing is significant because it is difficult to obtain such a structure from a perpendicular cylinder morphology, due to the very large surface energy difference between the two blocks. The nanoporous PDMS structures described here will be particularly useful in making hole arrays, due to their high etch resistance.

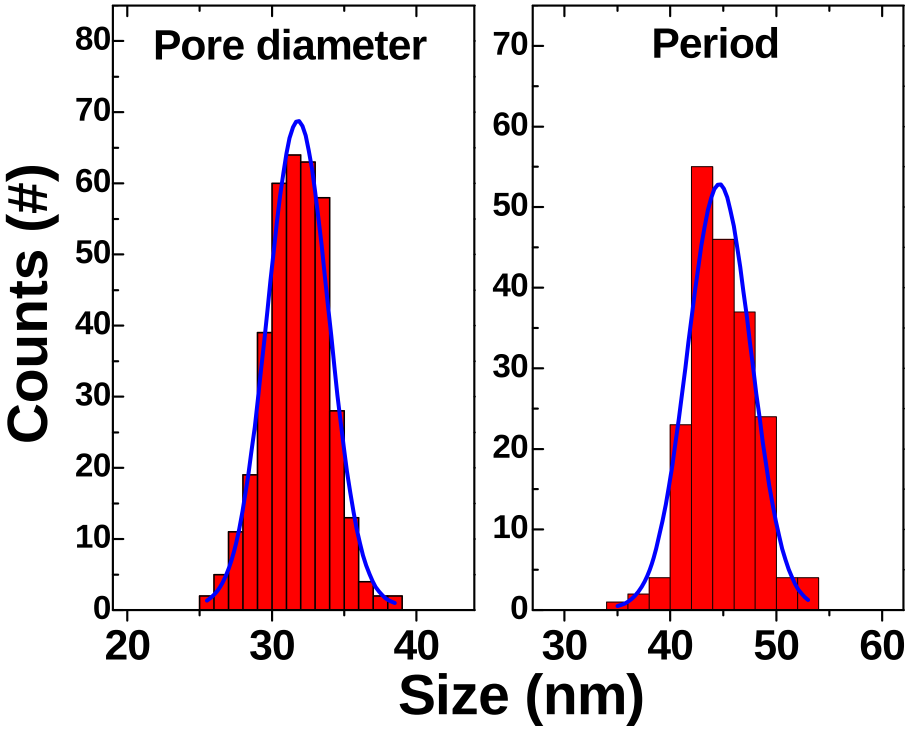

Fig. 3-9 Histograms of pore diameters (31.7 ± 2.1 nm) and periodicity (44.8 ± 3.1).

3.5 Summary

This chapter has presented how the geometry of thin films of a cylinder-forming BCP can be tuned over a wide range by using controlled solvent vapors. Control of two solvent-annealing parameters, the solvent mixing ratio and the vapor pressure, affect the period and linewidth of parallel cylinder arrays, and can even lead to different morphologies such as a perforated lamellar structure. The demonstration of independent control over the linewidth and period is useful for BCP-based fabrication of device structures. This process may also be applicable to other morphologies such as spheres and lamellae, and even to other material systems such as micelles or organic surfactant-coated nanoparticles.

References

[1] J. Bang, B. J. Kim, G. E. Stein, T. P. Russell, X. Li, J. Wang, E. J. Kramer, C. J. Hawker, "Effect of humidity on the ordering of PEO-based copolymer thin films", *Macromolecules 40*, p. 7019 (2007)

[2] J. K. Bosworth, M. Y. Paik, R. Ruiz, E. L. Schwartz, J. Q. Huang, A. W. Ko, D. M. Smilgies, C. T. Black, C. K. Ober, "Control of self-assembly of lithographically patternable block copolymer films", *Acs Nano 2*, p. 1396 (2008)

[3] M. Park, C. Harrison, P. M. Chaikin, R. A. Register, D. H. Adamson, "Block copolymer lithography: Periodic arrays of similar to 10(11) holes in 1 square centimeter", *Science 276*, p. 1401 (1997)

[4] T. Thurn-Albrecht, J. Schotter, C. A. Kastle, N. Emley, T. Shibauchi, L. Krusin-Elbaum, K. Guarini, C. T. Black, M. T. Tuominen, T. P. Russell, "Ultrahigh-density nanowire arrays grown in self-assembled diblock copolymer templates", *Science 290*, p. 2126 (2000)

[5] J. Y. Cheng, C. A. Ross, E. L. Thomas, H. I. Smith, G. J. Vancso, "Templated self-assembly of block copolymers: Effect of substrate topography", *Advanced Materials 15*, p. 1599 (2003)

[6] E. K. Kim, N. A. Stacey, B. J. Smith, M. D. Dickey, S. C. Johnson, B. C. Trinque, C. G. Willson, "Vinyl ethers in ultraviolet curable formulations for step and flash imprint lithography", *Journal of Vacuum Science & Technology B 22*, p. 131 (2004)

[7] R. A. Segalman, A. Hexemer, E. J. Kramer, "Edge effects on the order and freezing of a 2D array of block copolymer spheres", *Physical Review Letters 91*(2003)

[8] C. T. Black, O. Bezencenet, "Nanometer-scale pattern registration and alignment by directed diblock copolymer self-assembly", *IEEE Transactions on Nanotechnology 3*, p. 412 (2004)

[9] J. Y. Cheng, A. M. Mayes, C. A. Ross, "Nanostructure engineering by templated self-assembly of block copolymers", *Nature Materials 3*, p. 823 (2004)

[10] D. Sundrani, S. B. Darling, S. J. Sibener, "Hierarchical assembly and compliance of aligned nanoscale polymer cylinders in confinement", *Langmuir 20*, p. 5091 (2004)

[11] C. T. Black, "Self-aligned self assembly of multi-nanowire silicon field effect transistors", *Applied Physics Letters 87*, p. 163116 (2005)

[12] C. T. Black, R. Ruiz, G. Breyta, J. Y. Cheng, M. E. Colburn, K. W. Guarini, H. C. Kim, Y. Zhang, "Polymer self assembly in semiconductor microelectronics", *IBM Journal of Research and Development 51*, p. 605 (2007)

[13] J. Y. Cheng, W. Jung, C. A. Ross, "Magnetic nanostructures from block copolymer lithography: Hysteresis, thermal stability, and magnetoresistance", *Physical Review B 70*(2004)

[14] L. Rockford, S. G. J. Mochrie, T. P. Russell, "Propagation of nanopatterned substrate templated ordering of block copolymers in thick films", *Macromolecules 34*, p. 1487 (2001)

[15] J. Y. Cheng, C. T. Rettner, D. P. Sanders, H. C. Kim, W. D. Hinsberg, "Dense Self-Assembly on Sparse Chemical Patterns: Rectifying and Multiplying Lithographic Patterns Using Block Copolymers", *Advanced Materials* (2008)

[16] R. Ruiz, H. M. Kang, F. A. Detcheverry, E. Dobisz, D. S. Kercher, T. R. Albrecht, J. J. de Pablo, P. F. Nealey, "Density multiplication and improved lithography by directed block copolymer assembly", *Science 321*, p. 936 (2008)

[17] Y. Y. Wu, G. S. Cheng, K. Katsov, S. W. Sides, J. F. Wang, J. Tang, G. H. Fredrickson, M. Moskovits, G. D. Stucky, "Composite mesostructures by nano-confinement", *Nature Materials 3*, p. 816 (2004)

[18] H. Q. Xiang, K. Shin, T. Kim, S. I. Moon, T. J. McCarthy, T. P. Russell, "Block copolymers under cylindrical confinement", *Macromolecules 37*, p. 5660 (2004)

[19] F. S. Bates, G. H. Fredrickson, "Block Copolymer Thermodynamics - Theory and Experiment", *Annual Review of Physical Chemistry 41*, p. 525 (1990)

[20] E. Helfand, Y. Tagami, "Theory of the Interface between Immiscible Polymers. II", *Journal of Chemical Physics 56*, p. 3592 (1972)

[21] M. P. Stoykovich, M. Muller, S. O. Kim, H. H. Solak, E. W. Edwards, J. J. de Pablo, P. F. Nealey, "Directed assembly of block copolymer blends into nonregular device-oriented structures", *Science 308*, p. 1442 (2005)

[22] K. Fukunaga, H. Elbs, R. Magerle, G. Krausch, "Large-scale alignment of ABC block copolymer microdomains via solvent vapor treatment", *Macromolecules 33*, p. 947 (2000)

[23] J. Peng, Y. Xuan, H. F. Wang, Y. M. Yang, B. Y. Li, Y. C. Han, "Solvent-induced microphase separation in diblock copolymer thin films with reversibly switchable morphology", *Journal of Chemical Physics 120*, p. 11163 (2004)

[24] K. A. Cavicchi, K. J. Berthiaume, T. P. Russell, "Solvent annealing thin films of poly(isoprene-b-lactide)", *Polymer 46*, p. 11635 (2005)

[25] J. Bang, S. H. Kim, E. Drockenmuller, M. J. Misner, T. P. Russell, C. J. Hawker, "Defect-free nanoporous thin films from ABC triblock copolymers", *Journal of the American Chemical Society 128*, p. 7622 (2006)

[26] R. Guo, H. Y. Huang, Y. Z. Chen, Y. M. Gong, B. Y. Du, T. B. He, "Effect of the nature of annealing solvent on the morphology of diblock copolymer blend thin films", *Macromolecules 41*, p. 890 (2008)

[27] A. Knoll, A. Horvat, K. S. Lyakhova, G. Krausch, G. J. A. Sevink, A. V. Zvelindovsky, R. Magerle, "Phase behavior in thin films of cylinder-forming block copolymers", *Physical Review Letters 89*(2002)

[28] T. Hashimoto, M. Shibayama, H. Kawai, "Ordered Structure in Block Polymer-Solutions .4. Scaling Rules on Size of Fluctuations with Block Molecular-Weight, Concentration, and Temperature in Segregation and Homogeneous Regimes", *Macromolecules 16*, p. 1093 (1983)

[29] S. Alexander, "Polymer Adsorption on Small Spheres - Scaling Approach", *Journal De Physique 38*, p. 977 (1977)

[30] P. G. Degennes, "Conformations of Polymers Attached to an Interface", *Macromolecules 13*, p. 1069 (1980)

[31] A. Frischknecht, G. H. Fredrickson, "Microphase boundaries and chain conformations in multiply branched diblock copolymers", *Macromolecules 32*, p. 6831 (1999)

[32] S. P. Gido, D. W. Schwark, E. L. Thomas, M. D. Goncalves, "Observation of a Nonconstant Mean-Curvature Interface in an Abc Triblock Copolymer", *Macromolecules 26*, p. 2636 (1993)

[33] E. Helfand, Z. R. Wasserman, "Block Co-Polymer Theory .6. Cylindrical Domains", *Macromolecules 13*, p. 994 (1980)

[34] A. F. Barton, *CRC Handbook of Solubility Parameters and Other Cohesion Parameters* 2nd ed. ed., CRC Press, Boca Raton, FL (1991)

[35] S. Ludwigs, A. Boker, A. Voronov, N. Rehse, R. Magerle, G. Krausch, "Self-assembly of functional nanostructures from ABC triblock copolymers", *Nature Materials 2*, p. 744 (2003)

[36] I. Park, S. Park, H. W. Park, T. Chang, H. C. Yang, C. Y. Ryu, "Unexpected hexagonally perforated layer morphology of PS-b-PMMA block copolymer in supported thin film", *Macromolecules 39*, p. 315 (2006)

[37] R. A. Segalman, H. Yokoyama, E. J. Kramer, "Graphoepitaxy of spherical domain block copolymer films", *Advanced Materials 13*, p. 1152 (2001)

[38] D. Y. Ryu, K. Shin, E. Drockenmuller, C. J. Hawker, T. P. Russell, "A generalized approach to the modification of solid surfaces", *Science 308*, p. 236 (2005)

Chapter 4

Conductive polymer nanowires for gas sensor applications

4.1 Introduction

A molecular rectifier, theoretically proposed by Ratner and Aviram in 1974, was the starting point for a boom in molecular electronics research that has persisted for the last three decades.[1] Later, single-molecule field-effect transistors and logic gates were also conceptually proposed,[2] and Reed et al. first reported single-molecule conductance measurements through benzene-1,4-dithiol.[3] The development of conductive polymers has continued to attract considerable interest for many different applications including optoelectronic devices,[4-6] field effect transistors,[7, 8] and chemical or biological sensors.[8, 9] In these applications, device performance has been improved by miniaturizing the feature sizes down to the nanoscale regime,[10, 11] and there is, therefore, considerable interest in methods that enable the patterning of electronically-active polymers on the nanoscale.

Various fabrication techniques have been developed for generating conducting polymer nanowires. Chemical or electrochemical growth without templates usually produces entangled nanowires with a large distribution in diameter and length, which is undesirable in terms of performance and reproducibility, despite the convenience of fabrication.[12-16] For better-organized structures, scanning-probe and electron-beam patterning have been employed to direct the growth of conducting polymer nanowires.[11, 17, 18] Recently, spontaneous ordering of polymer nanowires was induced within a submicron gap between electrodes fabricated using a focused ion beam.[19]

However, the throughput and manufacturability of these methods are limited by the serial nature of the patterning techniques. Well-ordered conducting polymer nanopatterns have also been produced by nanoimprint lithography,[20] but this technique requires fabrication of master molds.

This chapter describes the fabrication of well-ordered arrays of 15 nm wide, 35 nm period poly(3,4-ethylenedioxythiophene):poly(styrenesulfonate) (PEDOT:PSS) conducting polymer nanowires, made over areas of several sq. cm. using a self-assembled block copolymer mask. This chapter also presents the capability of the patterned structures to act as an ethanol vapor sensor, confirming the preservation of the electronic properties of the PEDOT:PSS during patterning. Block copolymer self-assembly is a simple, cost-effective, and scalable maskless nanofabrication technique, in which the feature sizes and geometries can be controlled via the chain length and volume fractions of the blocks.[21-23] Poly(styrene-b-dimethylsiloxane) (PS-PDMS) diblock copolymer have an excellent etch-selectivity between the two polymer blocks as a result of the high Si content in the PDMS block,[24-26] and this facilitates pattern transfer into an underlying functional material. PEDOT:PSS was chosen for this study due to its superior stability and conductivity compared to other conducting polymers such as polypyrrole.[27] The well-organized conductive polymer nanowire arrays formed by this method may be useful for nanoscale organic device components such as interconnect lines or electrodes.

4.2 Experimental

Nanowire Fabrication

The substrates used were Si wafers with 30 nm-thick thermal oxide layers coated with a 40 nm-thick layer of sputtered silica. The substrates were patterned over areas of 1.7×1.7 cm^2 with parallel trenches with period of approximately 1.3 μm, width 1 μm and depth 40 nm. The trenches were made by coating the substrates with a positive resist (PFI-88) and exposing them with a grating pattern using a Lloyd's Mirror interference lithography system with a 325 nm wavelength He-Cd laser. Reactive ion etching (RIE) with a CF_4 plasma was used to transfer the grating pattern into the deposited silica. 20 nm-thick PEDOT:PSS thin films were spin-coated on the grating patterns from a 1.3 wt% aqueous solution of PEDOT:PSS purchased from Sigma-Aldrich and diluted to 0.87 wt% with deionized water. To remove agglomerated particles, the solution was filtered through a 0.25 μm membrane (Nalgene) before use. After spin-coating, the films were dried at 150°C for two minutes to remove moisture. Then, a thin silica film (5 nm) was sputter-deposited, and the silica surface was modified by hydroxy-terminated PDMS homopolymer with a molecular weight 5kg/mol, which was spin-cast on the substrates and annealed at 170°C for 15 hours, then washed with toluene to remove unreacted polymer. The thickness of the grafted brush layer was estimated to be 3-4 nm by ellipsometry. The diblock copolymer of PS-PDMS with overall molecular weight of 45.5 kg/mol and volume fraction of PDMS of 33.5% was purchased from Polymer Source, Inc. To obtain 35 nm-thick thin films, toluene solutions of 1.5% by weight of the block copolymer were spin-coated onto the substrates. Solvent-annealing in toluene vapor promoted self-assembly of the block copolymer into a structure consisting of in-plane cylinders of PDMS within a PS matrix, with a PDMS layer at the surface and at the substrate interface. Reactive ion etching was used to remove the PDMS surface layer (with a CF_4 plasma) and the PS matrix (with an O_2 plasma), leaving well-ordered arrays of oxidized PDMS cylinders.[24] These patterns were then transferred into the PEDOT:PSS layer using further reactive ion etch steps. To begin with, the very thin oxidized PDMS brush layer and the 5 nm-thick SiO_2 film were etched with a short CF_4 plasma, leading to a structure consisting of 12-13 nm thick oxidized PDMS cylinders on top of the PEDOT:PSS layer. The PEDOT:PSS layer was then etched with an O_2 plasma to form in-plane nanowires of PEDOT:PSS. A controlled overetching process using the 30 nm thick underlying SiO_2 as an etch stopper was employed to ensure a complete removal of the polymer film in unmasked areas. The etch selectivity between PEDOT:PSS and the oxidized PDMS mask is at least 10:1. The remaining oxidized PDMS was removed with another CF_4 plasma treatment step.

Electrical testing

The sensitivity of PEDOT:PSS nanowires and films to ethanol vapor was tested at room temperature. Au electrodes were deposited on top of the film or nanowire arrays by DC sputtering with a power of 50 W and an Ar working pressure of 10 mTorr. Two rectangular 1 mm x 6 mm Au electrodes with a 1 mm inter-electrode gap were fabricated using a stainless steel shadow mask. The samples were mounted on Al_2O_3 sample holders and contacted by Pt wires that were attached to the sputtered Au electrodes using silver paste (SPI Silver Paste Plus, SPI Supplies, Chester, PA, USA). The sample holders were then inserted inside a quartz tube chamber (16 mm inner diameter, 300 mm length, G. Finkenbeiner Inc., Waltham, MA, USA) to which inlet and outlet fittings had been attached. Mass flow controllers (MKS 1359C mass flow controllers and an MKS 647A controller unit) regulated the flow of nitrogen (99.998% purity) carrier gas through the two lines. One line was bubbled through liquid ethanol, providing a known flow rate of a saturated vapor. To eliminate interference effects due to changes in gas flow rate, the tests were carried out at a constant flow rate of total 200 sccm by mixing the ethanol/nitrogen gas with pure nitrogen from a second line. Thus, the ethanol concentration was varied from 0.5 to 50% of the saturated vapor. The resistance was measured under a DC bias voltage between 0.01 and 0.1 V using a DC power supply and picoammeter (HP 6626A and 4349B, respectively). R_0 is defined as the reference resistance measured in pure nitrogen while ΔR is the resistance change induced by exposure to ethanol in nitrogen. The relative sensitivity to ethanol is then given in terms of $\Delta R/ R_0$. The current-voltage response (HP 4142B Modular DC Source/Monitor) showed that this voltage lies within the linear regime of the sample's current-voltage response.

4.3 Patterning polymers using block copolymer etch masks

The procedure to fabricate PEDOT:PSS nanowires is depicted in Fig. 4-1 and described in detail in the previous section. The fabrication process is based on self-assembly of a PS-PDMS block copolymer film on a substrate. The silica-coated silicon substrate was initially patterned with 40 nm deep, 1.3 μm period trenches and then coated with PEDOT:PSS (20 nm), SiO_2 (5 nm) and a thin (3 - 4 nm) PDMS homopolymer brush. The silica layer provides a surface for grafting of the homopolymer, which improves the quality of the self-assembled PS-PDMS pattern.[24] The PS-PDMS block copolymer was spin-coated on this multilayer substrate and solvent annealed, leading to arrays of parallel PDMS cylinders in a PS matrix within the trenches. The arrays of PDMS cylinders, with thickness of 12 - 13 nm, period 35 nm, and width 15 nm, was etched into the underlying PEDOT:PSS film to form nanowires of PEDOT:PSS.

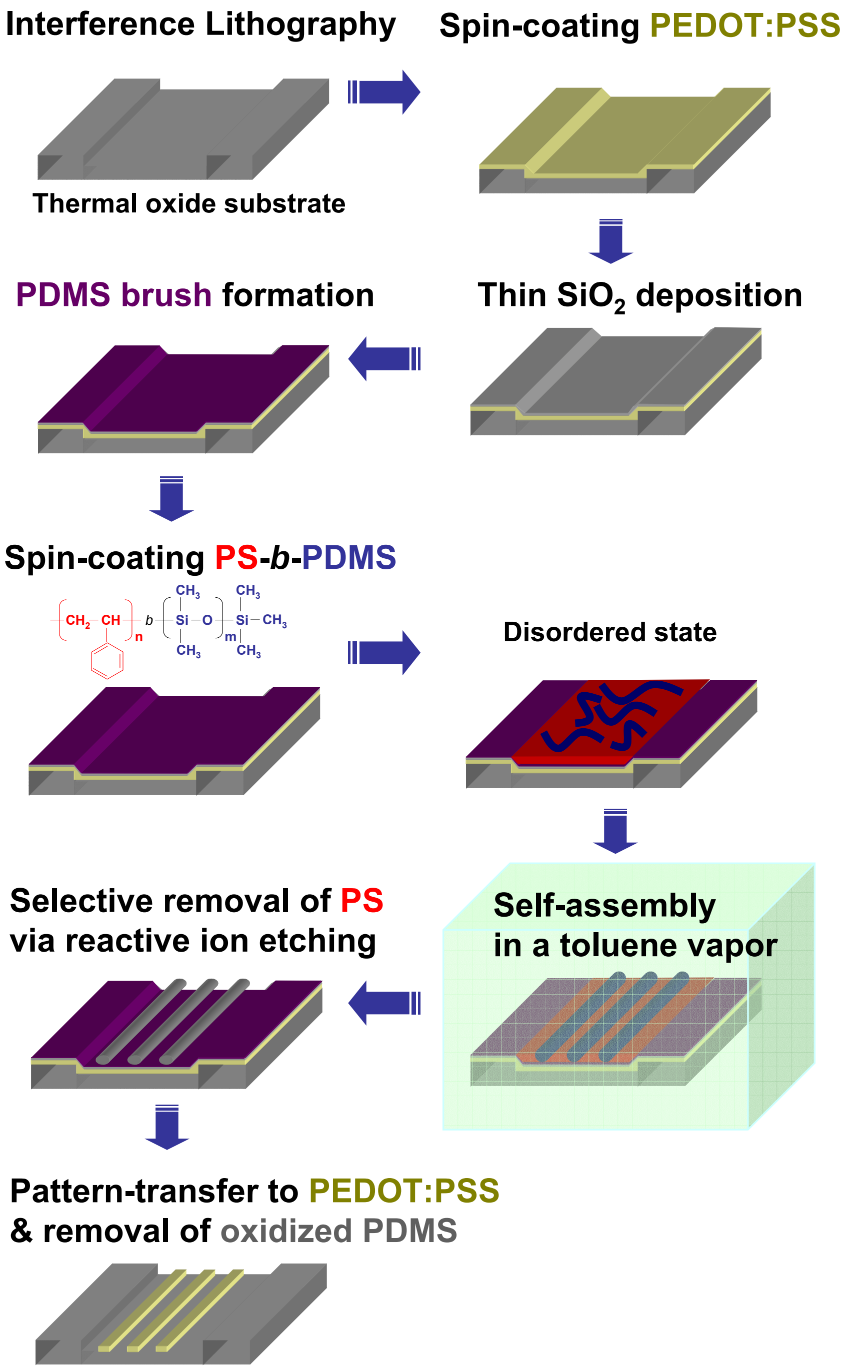

Fig. 4-1 Procedure for polymer nanowire fabrication. An aqueous PEDOT:PSS solution was spin-coated on a substrate patterned with a 1.3 μm period grating, then coated with a thin SiO$_2$ layer and a PDMS homopolymer brush. A PS-PDMS block copolymer thin film was then spin-coated and solvent-annealed. The self-assembled block copolymer patterns were transferred into the underlying PEDOT:PSS film through a series of reactive ion etching steps employing CF$_4$ and O$_2$ plasmas.

Self-assembled block copolymer patterns have been transferred into a range of metallic, oxide and semiconductor materials,[13, 24, 28, 29] but pattern transfer into functional polymers is more challenging. First, the underlying functional polymer must have a very low surface roughness, so that self-assembly of the block copolymer is not kinetically hindered. Second, the underlying polymer must be tolerant to the processing conditions used to form the homopolymer brush layer, or to promote microphase segregation in the block copolymer. In this case, the brush layer formation is carried out at 170°C for over 10 hours, while the solvent annealing of the block copolymer is carried out in toluene vapor for 17 hours. This requirement precludes the patterning of polymers with a low glass transition temperature, which may agglomerate on heating, or polymers soluble in toluene, e.g. polystyrene or polymethylmethacrylate, which can swell by toluene vapor uptake. However, spin-coated BarLi® or PEDOT:PSS films satisfy these criteria since they are smooth (root-mean-square roughness < 0.8 nm), thermally stable at 170°C, and poorly soluble in toluene.

In general, one disadvantage of block copolymer cylinders as an etch mask is a small thickness compared to a lamellar morphology. However, a pattern-transfer into underlying a polymer film can be a useful way to overcome the issue. In this way, patterns with a higher aspect ratio can be obtained. Figure 4-2 shows the patterning of a BarLi® film, which is often used as an antireflection coating for optical lithography. The polymer resin was diluted with cyclohexanone before spin-coating. After spin-coating the film was dried at 110°C for 90 seconds. After CF_4 and O_2 reactive ion etching processes, the aspect ratio was significantly enhanced as shown in Fig. 4-2 (b-d).

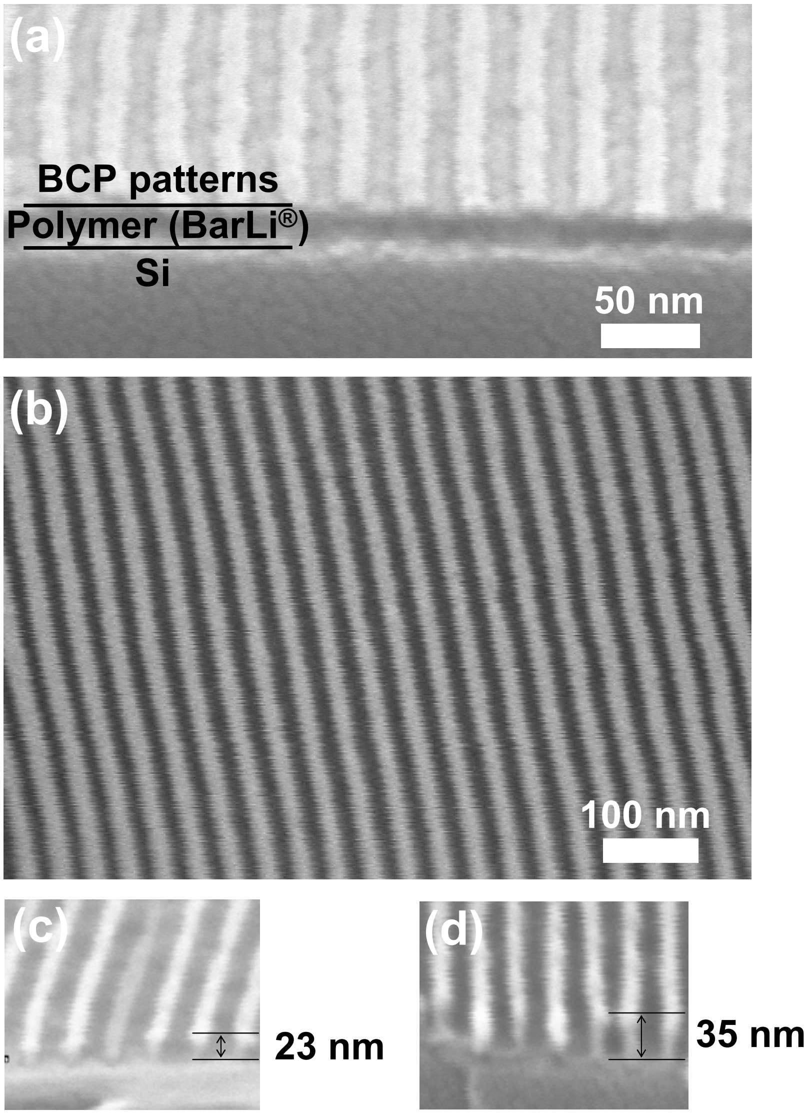

Fig. 4-2 (a) Self-assembled cylinders on a BarLi® film. (After removing PS) (b), (c), and (d) after O_2 reactive ion etching using the cylinders as an etch mask.

As shown in Fig. 4-3, the self-assembled PS-PDMS block copolymer patterns show an excellent degree of ordering within the trenches, with quality similar to that obtained previously in trenches etched into silicon and coated with a thin PDMS brush.[24] Although the cylinders adjacent to the trench edges show some edge roughness, correlated to roughness in the trench walls, the cylinders closer to the center of the groove are very straight with an edge roughness of 3.6 nm.

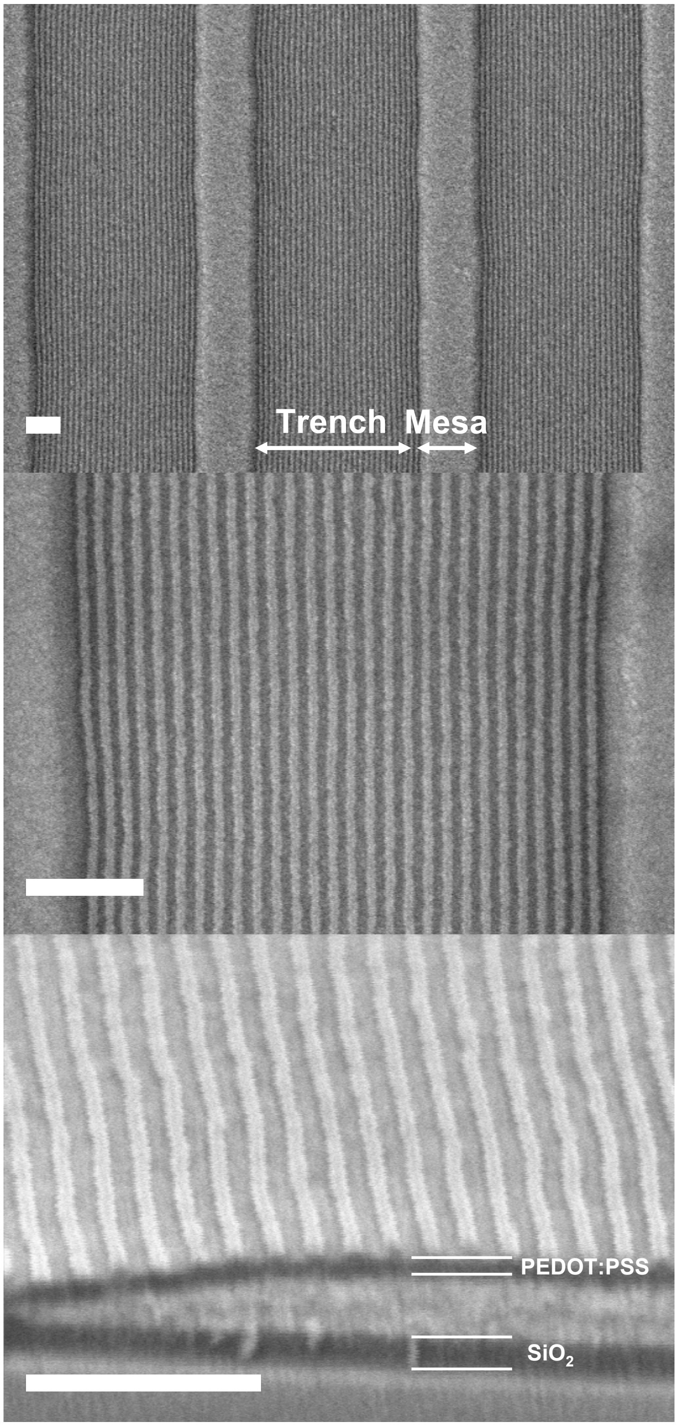

Fig. 4-3 Self-assembled cylinders on a PEDOT:PSS film. (After removing PS) The scale bars are 200 nm.

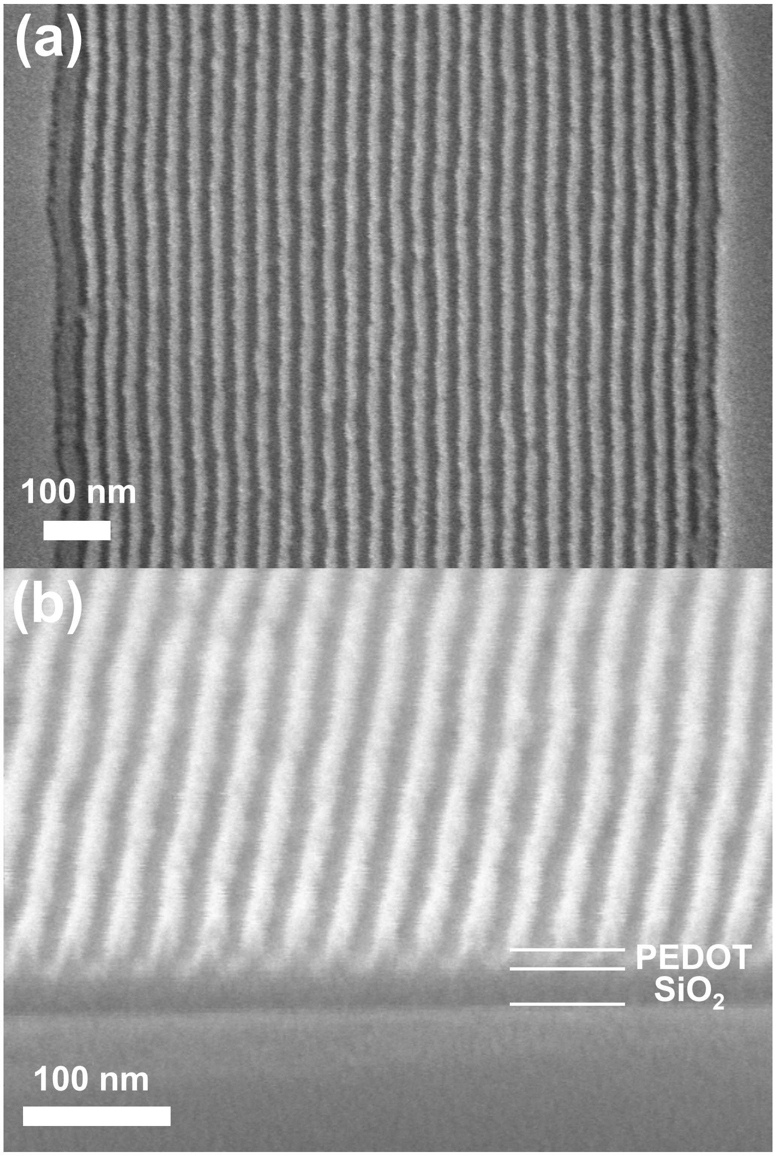

Fig. 4-4 PEDOT:PSS nanowires after 30 sec, 50W, O_2/He reactive ion etching, using the self-assembled PDMS patterns as an etch mask. The remaining PDMS and thin oxide interlayer were removed with an additional CF_4 plasma treatment.

Patterned conducting polymer nanowires with a width of 15 nm and a height of 20 nm are shown in Fig. 4-4. On a 1.7×1.7 cm^2 substrate, around 3.8×10^5 parallel conducting polymer nanowires were produced. To our knowledge, these PEDOT:PSS nanowires have the highest pattern density reported for conducting polymer nanowires. This patterning method therefore represents a simple and manufacturable process which is capable of defining large areas of nanoscale features in soft materials with a high aspect ratio (height/width), 1.33 in this case. The line edge roughness of the PEDOT:PSS patterns was 5.7 nm, larger than the 3.6 nm edge roughness of the block copolymer patterns.

4.4 Ethanol vapor sensor measurement

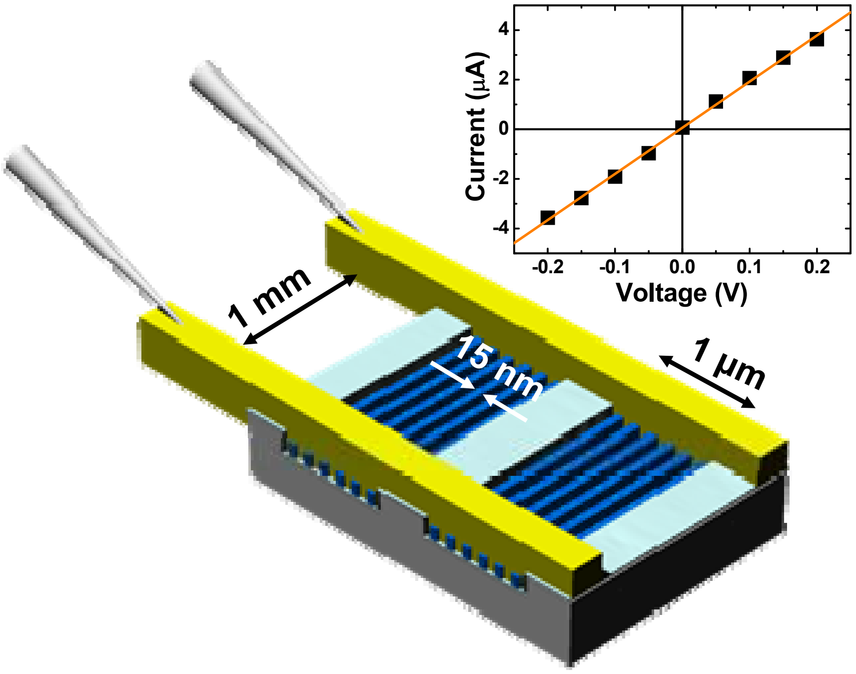

Fig. 4-5 Schematic (not to scale) of a chemiresistor for ethanol vapor detector based on PEDOT:PSS nanowires. 50 nm thick Au electrodes, 1 mm apart, are formed perpendicular to the nanowires. The linear current-voltage relationship is also demonstrated.

To test whether patterning affected the electrical properties of the polymer, thus study prepared a two-terminal chemiresistor gas sensor device based on the reversible change in electrical conductivity of the polymer as it swells upon exposure to an organic vapor.[30, 31] Uptake of small organic molecules changes the chain conformation and affects charge carrier hopping between the chains. The degree of swelling depends on the partial vapor pressure and the interaction between the polymer and organic vapor.

Fig. 4-5 schematically illustrates the formation of Au electrodes on top of the polymer nanopattern, enabling a large number (1.3×10^5) of nanowires to be measured in parallel. The linear current-voltage curve, as seen in the inset of Fig. 4-5, indicates that an ohmic contact was formed between the electrodes and the PEDOT:PSS. Fig. 4-6 shows the response of the conducting polymer nanowires to varying ethanol concentrations in the nitrogen carrier gas. The response, $\Delta R/R_0$, increased with the partial pressure of ethanol in the gas phase, confirming the ability of the nanowires to operate as an ethanol vapor detector, despite any damage to the PEDOT:PSS originating from the RIE processes. The resistance changes are observed to be largely reversible with some upward drift in R_0 apparent at larger partial pressures of ethanol. Based on the assumption that the ethanol vapor from the bubbler is fully saturated, the concentration of ethanol vapor was calculated from the equilibrium vapor pressure of ethanol (49.5 Torr at 22 ^{o}C), and thereby an ethanol detection limit may be estimated. Even the smallest partial pressure (0.25 Torr) of ethanol vapor, corresponding to 325 ppm, exhibits a relative resistance change of 1.5% as shown in Fig. 4-6. Both the polymer nanowires and thin films show a partial irreversibility of resistance as high as 3-5% especially for a large concentration of ethanol, which is consistent with previous reports.[13, 32] This is attributed to a non-equilibrium configuration of the chains in the as-deposited material, which rearrange in the presence of ethanol vapor, giving an aging effect.

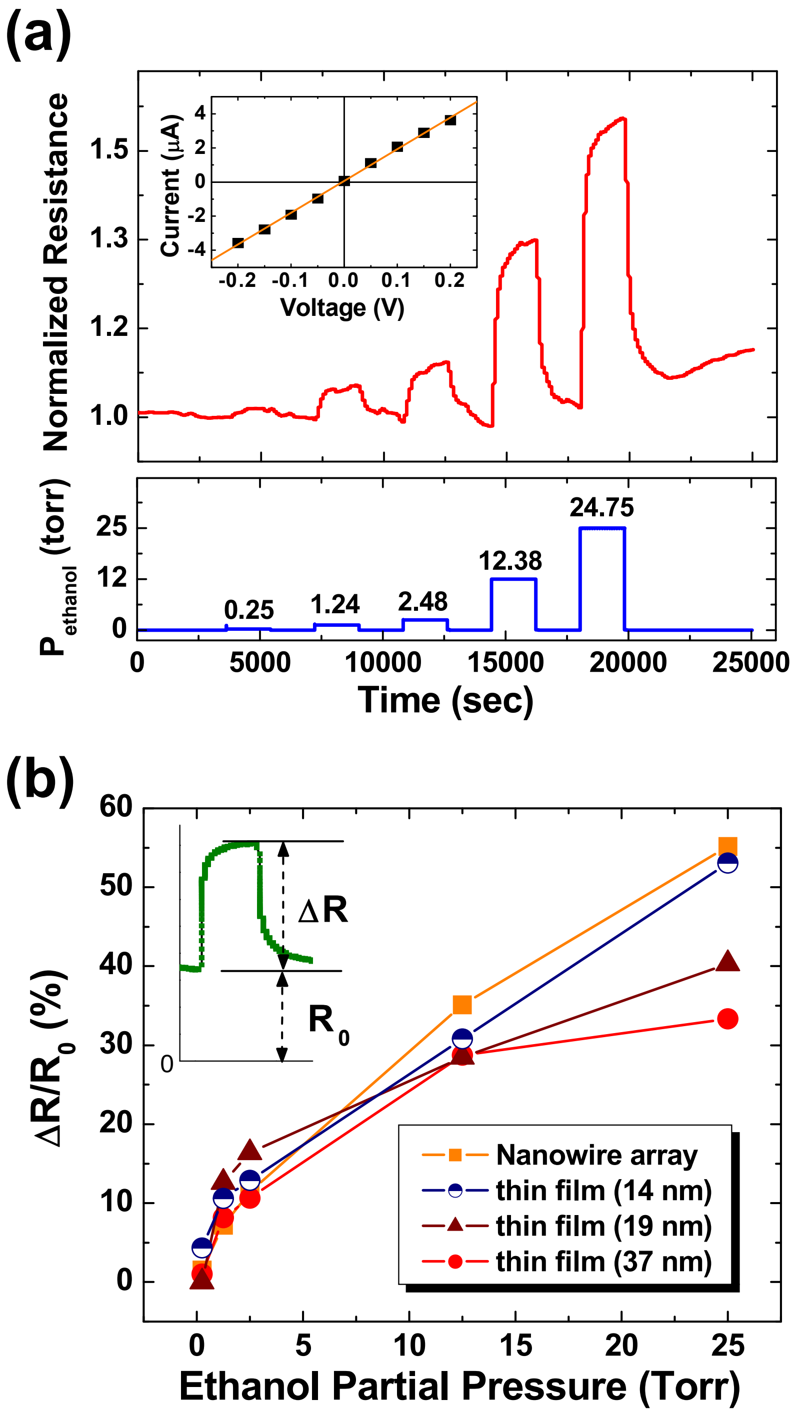

Fig. 4-6 (a) The resistance change of the polymer nanowires upon exposure to ethanol vapor. (b) Comparison of the response ($\Delta R/R_o$) of the nanowire array compared to that of thin films of three different thicknesses (14, 19, and 37 nm).

The response $\Delta R/R_0$ of the nanowire array is compared with that of three thin films in Fig. 4-6. All of the samples show an increase in $\Delta R/R_0$ with increased partial pressure of ethanol vapor. There is an evident divergence in response between the different thicknesses at the highest vapor pressure of 24.75 Torr, and so the influence of geometry was more carefully examined. At this pressure, the nanowires (20 nm thick, 15 nm wide) show a considerably higher $\Delta R/R_0$ response compared to the 19 nm and 37 nm thick films, but similar to that of the 14 nm thick film. This appears to be due to the thicker films exhibiting a saturation in response to higher ethanol vapor pressure. This result is consistent with a previous report on polyaniline, which showed that as film thickness decreases, the sensitivity increases and that if the film is thin enough, a sensitivity close to that of a nanostructured material can be obtained.[31]

It has been suggested that a higher surface-to-volume ratio causes faster diffusion of solvent molecules, and this gives nanostructured materials and thinner films a faster, higher amplitude response.[13, 19, 20, 31] In inorganic materials used for vapor detection, gas adsorption on the surface induces a Fermi level shift and carrier depletion near the surface, which explains the enhanced sensitivity for devices with higher surface area.[33] However, swelling of a polymer, which is responsible for the electrical response of the PEDOT:PSS to ethanol vapor, occurs throughout its volume, and thus a higher diffusion rate, while leading to a faster response, should not lead to higher sensitivity at equilibrium. That is, unless we assume that the near-surface region has a higher equilibrium solubility for a given vapor pressure compared to the bulk, due to a larger free energy resulting from added surface energy and smaller conformational entropy (Fig. 4-7a).[34, 35] While this would explain the trends in Fig. 4-6 for the highest gas concentrations, it does not explain the near equal responses of all the devices to ethanol partial pressures of 2.5 Torr and below. It is more likely that the difference in sensitivity between the samples is caused by a kinetic limitation related to the longer characteristic diffusion lengths associated with the thicker structures (Fig. 4-7b). Particularly for high vapor pressures, considerable residual swelling remains in the thicker films from previous exposures, leading to an apparent decrease in sensitivity for these films.

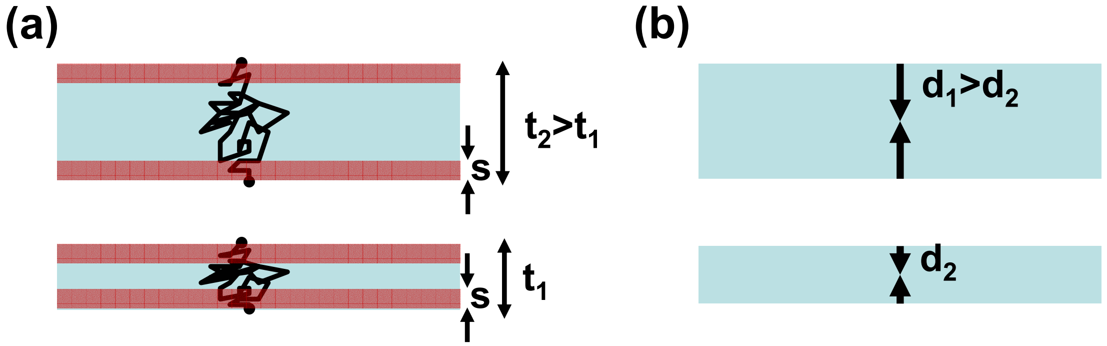

Fig. 4-7 (a) Thermodynamic and (b) kinetic models to explain the enhancement of sensitivity as a function of surface-to-volume ratio

4.5 Summary

This chapter demonstrated the fabrication of a nanowire ethanol vapor sensor from a film of PEDOT:PSS conducting polymer, patterned into a nanowire array using a block copolymer self-assembled within a topographical template. The nanowire array shows a higher and more linear resistance response than an unpatterned film with the same thickness, which is attributed to its high surface area to volume ratio and to its short diffusion length. The fact that the conducting properties of the film are preserved through the etching process further suggests that self-assembled nanolithography may also be applied to fabricate other conductive conjugated polymers to form active devices such as light-emitting diodes, memories, or transistor arrays.

References

[1] A. Aviram, M. A. Ratner, "Molecular Rectifiers", *Chemical Physics Letters 29*, p. 277 (1974)

[2] A. Aviram, "Molecules for Memory, Logic, and Amplification", *Journal of the American Chemical Society 110*, p. 5687 (1988)

[3] M. A. Reed, C. Zhou, C. J. Muller, T. P. Burgin, J. M. Tour, "Conductance of a molecular junction", *Science 278*, p. 252 (1997)

[4] D. Braun, A. J. Heeger, "Visible-Light Emission from Semiconducting Polymer Diodes", *Applied Physics Letters 58*, p. 1982 (1991)

[5] Q. B. Pei, G. Yu, C. Zhang, Y. Yang, A. J. Heeger, "Polymer Light-Emitting Electrochemical-Cells", *Science 269*, p. 1086 (1995)

[6] H. Sirringhaus, N. Tessler, R. H. Friend, "Integrated optoelectronic devices based on conjugated polymers", *Science 280*, p. 1741 (1998)

[7] H. Sirringhaus, P. J. Brown, R. H. Friend, M. M. Nielsen, K. Bechgaard, B. M. W. Langeveld-Voss, A. J. H. Spiering, R. A. J. Janssen, E. W. Meijer, P. Herwig, D. M. de Leeuw, "Two-dimensional charge transport in self-organized, high-mobility conjugated polymers", *Nature 401*, p. 685 (1999)

[8] F. Garnier, R. Hajlaoui, A. Yassar, P. Srivastava, "All-Polymer Field-Effect Transistor Realized by Printing Techniques", *Science 265*, p. 1684 (1994)

[9] B. S. Gaylord, A. J. Heeger, G. C. Bazan, "DNA hybridization detection with water-soluble conjugated polymers and chromophore-labeled single-stranded DNA", *Journal of the American Chemical Society 125*, p. 896 (2003)

[10] J. Zhang, B. J. Wang, X. Ju, T. Liu, T. D. Hu, "New observations on the optical properties of PPV/TiO2 nanocomposites", *Polymer 42*, p. 3697 (2001)

[11] H. Q. Liu, J. Kameoka, D. A. Czaplewski, H. G. Craighead, "Polymeric nanowire chemical sensor", *Nano Letters 4*, p. 671 (2004)

[12] H. X. He, C. Z. Li, N. J. Tao, "Conductance of polymer nanowires fabricated by a combined electrodeposition and mechanical break junction method", *Applied Physics Letters 78*, p. 811 (2001)

[13] C. Harrison, P. M. Chaikin, D. A. Huse, R. A. Register, D. H. Adamson, A. Daniel, E. Huang, P. Mansky, T. P. Russell, C. J. Hawker, D. A. Egolf, I. V. Melnikov, E. Bodenschatz, "Reducing substrate pinning of block copolymer microdomains with a buffer layer of polymer brushes", *Macromolecules 33*, p. 857 (2000)

[14] E. S. Forzani, H. Q. Zhang, L. A. Nagahara, I. Amlani, R. Tsui, N. J. Tao, "A conducting polymer nanojunction sensor for glucose detection", *Nano Letters 4*, p. 1785 (2004)

[15] M. M. Alam, J. Wang, Y. Y. Guo, S. P. Lee, H. R. Tseng, "Electrolyte-gated transistors based on conducting polymer nanowire junction arrays", *Journal of Physical Chemistry B 109*, p. 12777 (2005)

[16] Y. J. Wang, K. K. Coti, W. Jun, M. M. Alam, J. J. Shyue, W. X. Lu, N. P. Padture, H. R. Tseng, "Individually addressable crystalline conducting polymer nanowires in a microelectrode sensor array", *Nanotechnology 18*, p. 424021 (2007)

[17] M. H. Yun, N. V. Myung, R. P. Vasquez, C. S. Lee, E. Menke, R. M. Penner, "Electrochemically grown wires for individually addressable sensor arrays", *Nano Letters 4*, p. 419 (2004)

[18] K. Ramanathan, M. A. Bangar, M. H. Yun, W. F. Chen, A. Mulchandani, N. V. Myung, "Individually addressable conducting polymer nanowires array", *Nano Letters 4*, p. 1237 (2004)

[19] N. T. Kemp, D. McGrouther, J. W. Cochrane, R. Newbury, "Bridging the gap: Polymer nanowire devices", *Advanced Materials 19*, p. 2634 (2007)

[20] B. Dong, N. Lu, M. Zelsmann, N. Kehagias, H. Fuchs, C. M. S. Torres, L. F. Chi, "Fabrication of high-density large-area conducting-polymer nanostructures", *Advanced Functional Materials 16*, p. 1937 (2006)

[21] M. Park, C. Harrison, P. M. Chaikin, R. A. Register, D. H. Adamson, "Block copolymer lithography: Periodic arrays of similar to 10(11) holes in 1 square centimeter", *Science 276*, p. 1401 (1997)

[22] E. Schaffer, T. Thurn-Albrecht, T. P. Russell, U. Steiner, "Electrically induced structure formation and pattern transfer", *Nature 403*, p. 874 (2000)

[23] J. Y. Cheng, C. A. Ross, H. I. Smith, E. L. Thomas, "Templated self-assembly of block copolymers: Top-down helps bottom-up", *Advanced Materials 18*, p. 2505 (2006)

[24] Y. S. Jung, C. A. Ross, "Orientation-controlled self-assembled nanolithography using a polystyrene-polydimethylsiloxane block copolymer", *Nano Letters 7*, p. 2046 (2007)

[25] I. Bita, J. K. W. Yang, Y. S. Jung, C. A. Ross, E. L. Thomas, K. K. Berggren, "Graphoepitaxy of self-assembled block copolymers on two-dimensional periodic patterned templates", *Science 321*, p. 939 (2008)

[26] Y. S. Jung, W. Jung, C. A. Ross, "Nanofabricated Concentric Ring Structures by Templated Self-Assembly of a Diblock Copolymer", *Nano Lett.8*, p. 2975 (2008)

[27] G. A. Sotzing, S. M. Briglin, R. H. Grubbs, N. S. Lewis, "Preparation and properties of vapor detector arrays formed from poly(3,4 ethylenedioxy)thiophene-poly(styrene sulfonate)/insulating polymer composites", *Analytical Chemistry 72*, p. 3181 (2000)

[28] J. Y. Cheng, C. A. Ross, V. Z. H. Chan, E. L. Thomas, R. G. H. Lammertink, G. J. Vancso, "Formation of a cobalt magnetic dot array via block copolymer lithography", *Advanced Materials 13*, p. 1174 (2001)

[29] C. T. Black, "Self-aligned self assembly of multi-nanowire silicon field effect transistors", *Applied Physics Letters 87*, p. 163116 (2005)

[30] K. J. Albert, N. S. Lewis, C. L. Schauer, G. A. Sotzing, S. E. Stitzel, T. P. Vaid, D. R. Walt, "Cross-reactive chemical sensor arrays", *Chemical Reviews 100*, p. 2595 (2000)

[31] S. Virji, J. X. Huang, R. B. Kaner, B. H. Weiller, "Polyaniline nanofiber gas sensors: Examination of response mechanisms", *Nano Letters 4*, p. 491 (2004)

[32] M. F. Mabrook, C. Pearson, M. C. Petty, "An inkjet-printed chemical fuse", *Applied Physics Letters 86*, p. 013507 (2005)

[33] A. Kolmakov, M. Moskovits, "Chemical sensing and catalysis by one-dimensional metal-oxide nanostructures", *Annual Review of Materials Research 34*, p. 151 (2004)

[34] M. R. Wattenbarger, H. S. Chan, D. F. Evans, V. A. Bloomfield, K. A. Dill, "Surface-Induced Enhancement of Internal Structure in Polymers and Proteins", *Journal of Chemical Physics 93*, p. 8343 (1990)

[35] M. Khayet, M. V. Alvarez, K. C. Khulbe, T. Matsuura, "Preferential surface segregation of homopolymer and copolymer blend films", *Surface Science 601*, p. 885 (2007)

[36] T. H. Andersen, S. Tougaard, N. B. Larsen, K. Almdal, I. Johannsen, "Surface morphology of PS-PDMS diblock copolymer films", *Journal of Electron Spectroscopy and Related Phenomena 121*, p. 93 (2001)

Chapter 5

Formation of concentric ring patterns by circular confinement

5.1 Introduction

Self-organization of macromolecular materials can provide an alternative pathway to conventional lithography for the fabrication of devices on the nanometer scale. In particular, the self-assembly of the microdomains of diblock copolymers within lithographically-defined templates to create patterns with long range order has attracted considerable attention, due to the scalability and cost-effectiveness of the process.[1, 2] Devices such as field effect transistors, capacitors, flash memory cells, high density magnetic storage media, photovoltaic devices, and photonic crystals made using block copolymer patterning have been proposed or demonstrated.[3-6]

In developing self-assembly methods for device fabrication, it is important to be able to create a range of pattern geometries. One important geometry is that consisting of single or concentric rings. Several devices based on ring shaped features have been designed, including sensors,[7, 8] magnetic memories,[9-11] transistors,[12] optical memories,[13] ring resonator lasers,[14] and structures used to investigate quantum interference phenomena such as the Aharonov–Bohm effect[15] or persistent currents.[16, 17] As an example, three-dimensionally confined semiconductor quantum rings (or coupled concentric double quantum rings) that behave as artificial atoms have discrete energy levels that can be engineered for performing quantum computations or realizing advanced electronic or optoelectronic devices.[18, 19]

Self-assembly of thin films of diblock copolymers typically yields patterns consisting of parallel lines or close-packed arrays of dots or holes, and the formation of 2D ring-shaped patterns suitable for device fabrication is less well explored. A self-assembly-based method for creating ring patterns of controlled geometry may enable the scaling of ring-shape devices, with consequent improvements in speed or power consumption.

This chapter demonstrates the templating of concentric ring patterns from cylindrical-morphology poly(styrene-b-dimethylsiloxane) (PS-PDMS) using topographical templates, and show how these patterns can be incorporated into a device fabrication process by forming and characterizing a high-density (1.1×10^{9}/cm^{2}) array of ferromagnetic cobalt rings. In particular, this thesis analyzes the effects of commensurability between the diameter of the template and the period of the unconfined block copolymer. This fabrication technique is tolerant to a wide range of processing conditions due to the robustness of the oxidized PDMS patterns, and is applicable to diverse types of materials and deposition techniques.

5.2 Experimental

The 40-nm deep circular trench patterns (Fig. 5-1) were fabricated using a Lloyd's Mirror interference lithography system with a 325 nm wavelength He-Cd laser. A negative resist (PS4, Tokyo Ohka Co., Ltd.) with a thickness of 200 nm was spin-coated on an oxidized Si wafer. Circular patterns on a 10-cm-wafer were fabricated by exposing an interference pattern (a grating) at a dose that is lower than a full exposure condition, rotating the sample by 90˚, and exposing a second grating. The dose distribution is given by the superposition of two perpendicularly aligned standing waves ($I=A\sin^{2}(\pi x/p)+A\sin^{2}(\pi y/p)$, where $2A$ is the maximum dose, p is the interference period, and x and y are the directions of the standing waves). Development results in a square array of rounded holes with their longest diameters in the x and y directions.[20] The diameter of the circular patterns was changed from 60 to 350 nm by controlling the total exposure time and the interference angle of the laser beams. Reactive ion etching with CF_4 gas was employed to transfer the circular patterns into the oxide substrate.

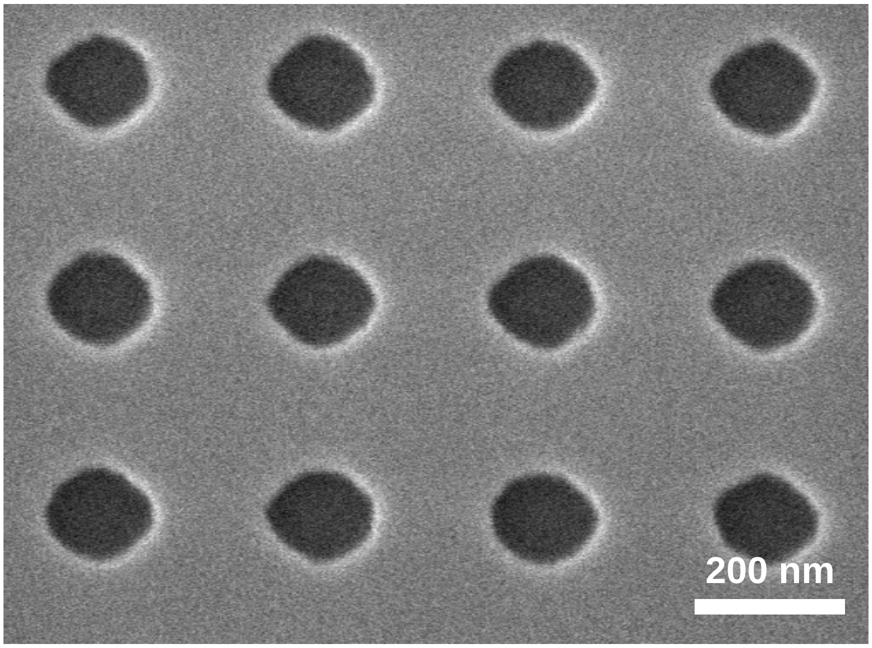

Fig. 5-1 Circular trench patterns fabricated by interference lithography.

A diblock copolymer of PS-PDMS with overall molecular weight of 45.5 kg/mol and volume fraction of PDMS f_{DMS} = 33.5% was custom made by Polymer Source, Inc. The substrate surface was modified by hydroxy-terminated PDMS homopolymer with molecular weight 5kg/mol, which was spin-cast and annealed at 170 °C for 15 hours, then unreacted material was removed with a toluene wash. The thickness of the grafted brush layer was estimated to be 3-4 nm by ellipsometry. The PS-PDMS block copolymer films were spin-cast from a 1 wt% solution in toluene. Solvent annealing was performed at room temperature for 16 hours under a controlled toluene vapor pressure.[21] Toluene vapor induces swelling of the polymer films, decreases the glass transition temperature below room temperature, and promotes rearrangement of the polymer chains. During the solvent annealing, the block copolymer flows from the mesas to the trenches,[2, 21] and a careful thickness tuning was necessary to get a thickness of 35 nm PS-PDMS in the trenches without any excess polymer present on the mesa regions after solvent annealing. The annealed film was treated with a 5 sec, 50 W CF_4 plasma and then a 90 W O_2 plasma to remove first the PDMS surface layer and then the PS matrix to leave oxygen-plasma-modified PDMS cylinders on the substrate.[21] The surface morphology was observed using a Zeiss/Leo Gemini 982 scanning electron microscope (SEM) operated at 5 kV. The samples were coated with a thin Au-Pd alloy film before loading in order to reduce charging effects. A Co thin film with a thickness of 70 nm was sputter-deposited (300 W, 2 mtorr) on top of the block copolymer patterns and etched with a 450W 10 mTorr CF_4 plasma for 25 mins. Initially the Co film is sputter-etched at 2.3 nm/min by ionized CF_x species but after approximately 58 nm of film was removed, the buried block copolymer patterns were exposed to the plasma, and then were etched about 60 times faster than the Co. Magnetic hysteresis loops were obtained from a vibrating sample magnetometer (ADE, model 1660) at room temperature. Micromagnetic modeling was carried out using the two dimensional OOMMF software from NIST, with 2×2 nm^2 cells, 10 nm thick, and saturation magnetization M_s = 1400 emu/cm^3, random anisotropy $K_1 = 5.2\times10^6$ erg/cm^3, exchange constant $A = 1\times10^{-6}$ erg/cm, and damping coefficient of $\alpha = 0.5$.

5.3 Formation of ring patterns induced by circular confinement

Previous work has demonstrated both topographical[22, 23] and chemical templating[24, 25] as a method to improve the long range order of self-assembled block copolymer microdomains. Although large scale 2D concentric ring patterns have been made by confinement of cylindrical or lamellar morphology block copolymers,[2, 26, 27] there has been no work reported on small diameter circular patterns where commensurability effects are critical. In contrast, considerable attention has been paid to understanding the 3D confinement of block copolymers within cylindrical pores, both computationally[2, 28, 29] and experimentally.[30-33] However, these 3D morphologies cannot easily be incorporated into a 2D planar process for device fabrication. Nanoring arrays have been prepared using polymeric templates such as nanospheres[34] or nanoporous[35] films, obtaining, for example, 13 nm diameter rings using angled evaporation of metal into cylindrical pores[35]. However, these methods typically yield rings with 3D tapered cross-sections, and cannot produce concentric patterns.

A PS-PDMS diblock copolymer for block copolymer lithography was chosen because of the high etch selectivity between the two blocks, the robustness of the PDMS patterns for pattern transfer, and the large correlation length and low edge roughness of the patterns.[21] The PS-PDMS (31 kg/mol for PS, 11 kg/mol for PDMS) block copolymer was spin-coated over PDMS brush-coated silica substrates prepatterned with arrays of 40 nm deep approximately-circular pits of a range of diameters, then solvent-annealed and etched to reveal the arrangement of the PDMS cylinders in plane. Figure 5-2 shows a scanning electron micrograph of a sample of the resulting concentric rings, which were formed over large area substrates (1 cm^2) with good uniformity. The white stripes indicate the oxidized PDMS in-plane cylindrical domains after O_2 plasma reactive ion etching (RIE), about 13 nm tall, while the dark regions correspond to the volume originally occupied by the PS domains, which were removed by the RIE. The central feature in these structures is a circular PDMS domain, analogous to the central cylinder seen for lamellar block copolymers assembled in tall pores[33].

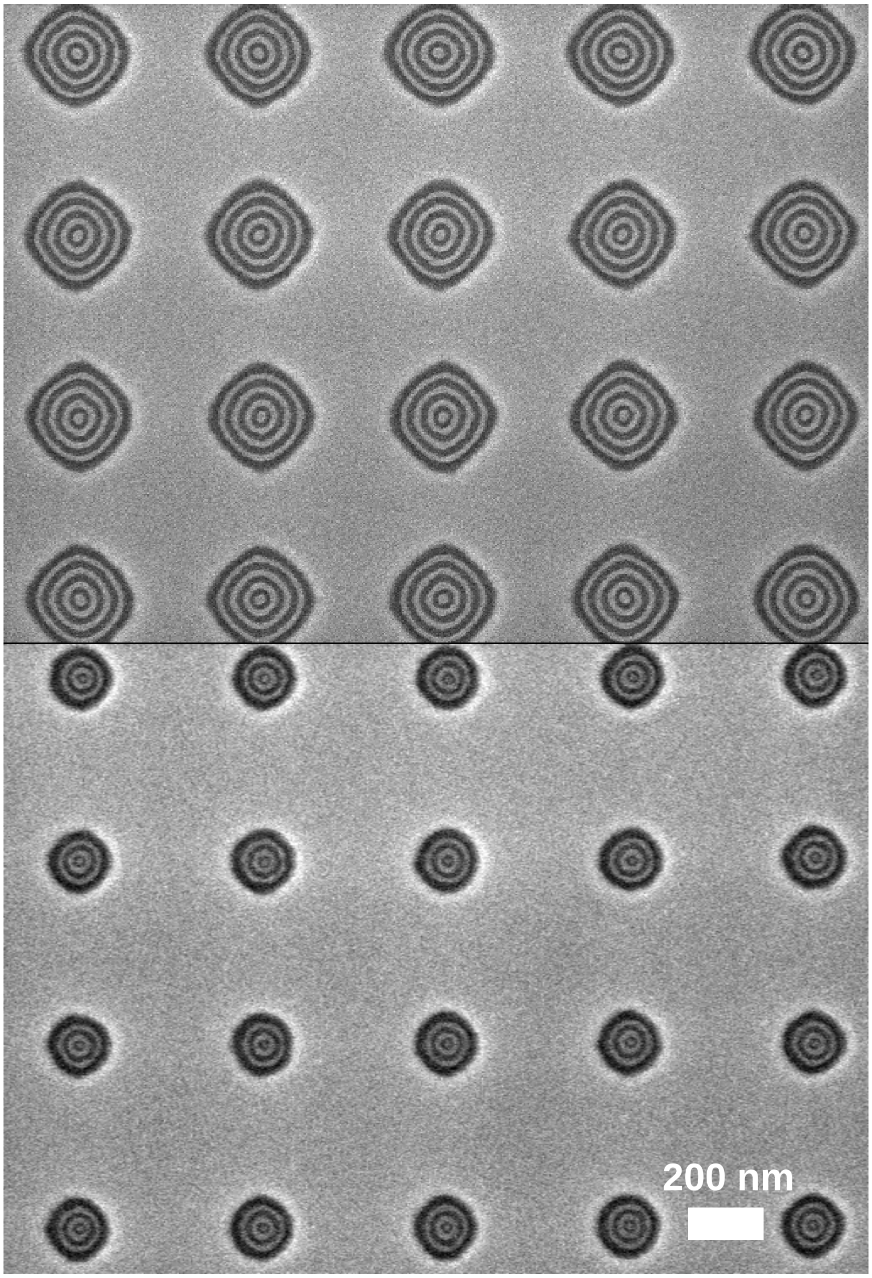

Fig. 5-2 Morphology of the self-assembled PS-PDMS block copolymer after exposure to a CF_4 plasma (5 s) followed by an O_2 plasma (30 s). Scanning electron micrograph of concentric PDMS ring patterns (light contrast) in an array of 250 nm (top) and 170 nm (bottom) diameter circular pits.

The circular patterns in the pits have a lower eccentricity than the templates, which resemble rounded squares, and the rings show lower edge roughness than rings made from PS-PMMA.[26] The smoothly curved structures observed here are attributed to the very large χ parameter of PS-PDMS

(χ~0.26 at 300K, compared to 0.06 for PS-PMMA[36, 37]), which promotes the formation of geometries that minimize the interfacial area between the domains. Based on the relative χ parameters, PS-PDMS is expected to have an interfacial width of 0.95 nm, compared to 3 nm for PS-PMMA.[1] A root-mean-square roughness of 3.2±0.2 nm was measured for etched PDMS patterns. In bulk, the PDMS cylinders are generally straight, and their bending into circular shapes of small radius incurs an additional energy term, which will be analysed later. In this study, both the trench surfaces, with their grafted PDMS brush, and the air interface, due to differences in surface tension, all strongly attract the minority PDMS block, which has a significantly lower surface tension (γ=19.9 mN/m) than PS (γ=40.7 mN/m).[38] The concentric PDMS ring structures in their PS matrix are therefore sandwiched between thin surface and interface PDMS brush layers.

5.4 Analyses and modeling on concentric ring patterns

Figure 5-3 illustrates how the ring patterns vary with confinement diameter C. The equilibrium period (L_{eq}) of in-plane cylinders on a smooth substrate is 34.2 nm for this polymer.[21] The ratio C/L_{eq} was varied from 1.7 to 10. For some diameters, the innermost feature is a PDMS sphere while for others a smaller PS sphere is formed. For the smallest trenches ($C < 77$ nm, $C/L_{eq} < 2.2$), only a PDMS sphere is observed. This may be compared to simulation results[29] for the self-assembly of a block copolymer in a tall, narrow cylindrical pore, in which the minority block forms a central axial feature for $2.1 < C/L_{eq} < 2.7$.

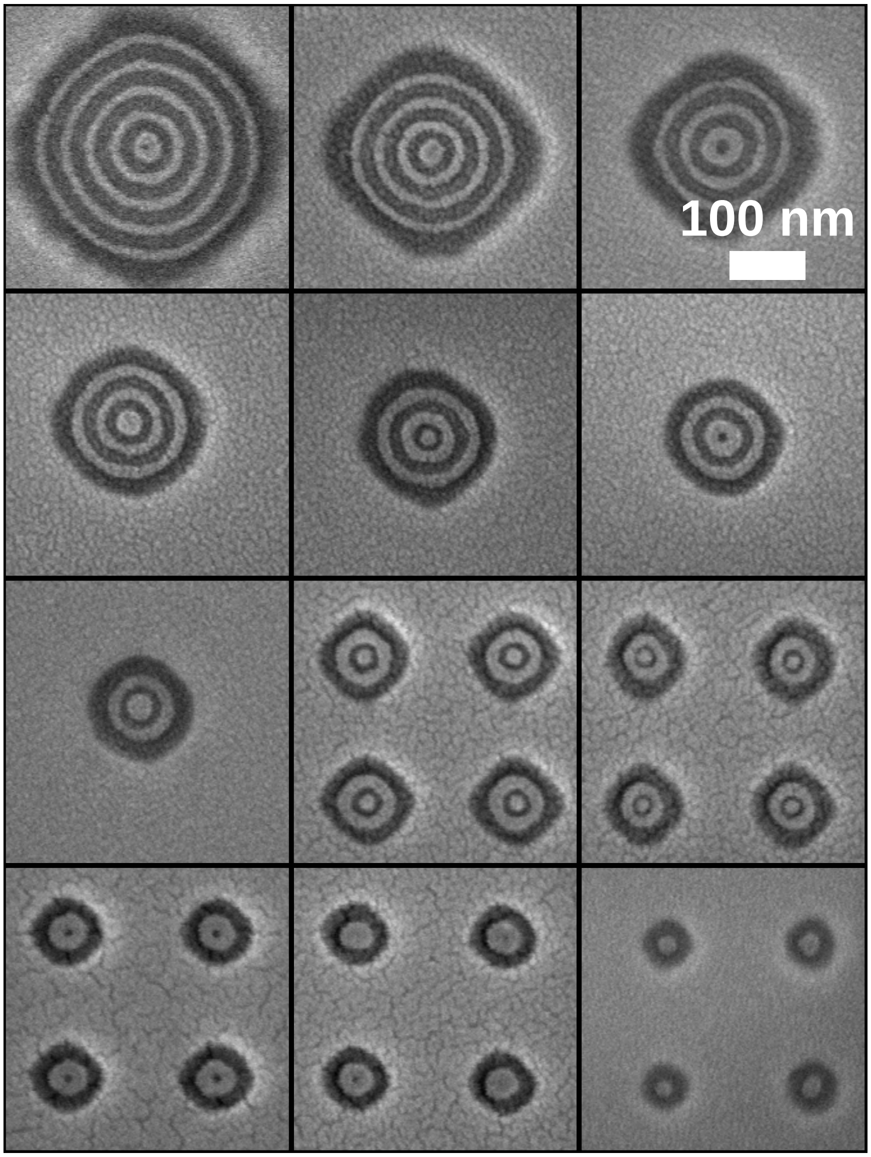

Fig. 5-3 Concentric ring patterns in templates with various confinement diameters C. The ratio C/L_{eq} was varied from 1.7 to 10. For some diameters, the innermost feature is a PDMS sphere (light contrast) and for others a smaller PS sphere (dark) is formed. The scale bar represents 100 nm.

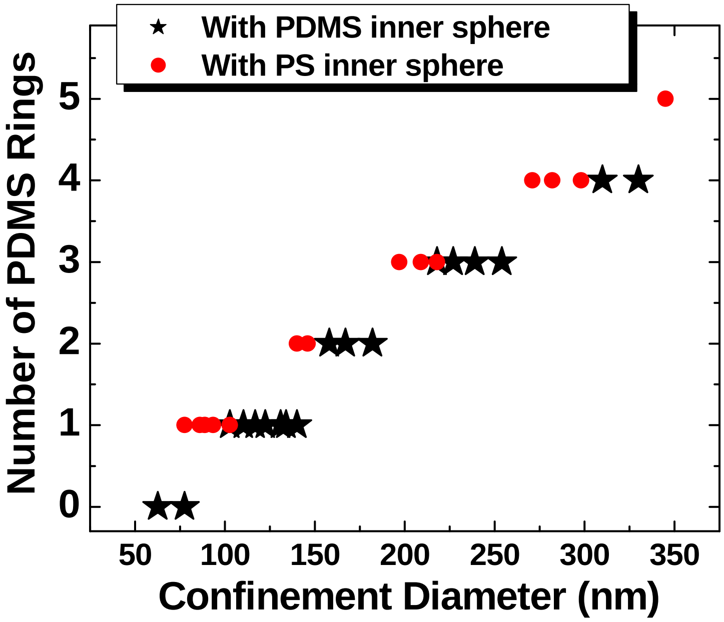

Fig. 5-4 The number of concentric rings in a template as a function of its diameter, C. Stars indicate patterns with a central PDMS sphere while solid circles indicate patterns with a central PS sphere.

Fig. 5-4 shows the number of rings formed as a function of confinement diameter C. Solid symbols and stars indicate the structures with a PS domain and a PDMS domain in the center, respectively. There is an overlap between the ranges of confinement diameter that generate a given pattern, for example a pit of diameter 140 nm may contain either two PDMS rings with a PS inner feature, or one PDMS ring plus a center PDMS sphere, while a pit of diameter 218 nm may contain three PDMS rings with either a PS or PDMS inner feature. Similar degeneracy has been observed in a number of confined block copolymer systems, for example in spheres packed into trenches[22] or lamellae packed into pores[33], where a given confinement diameter can accommodate n or n+1 domains.

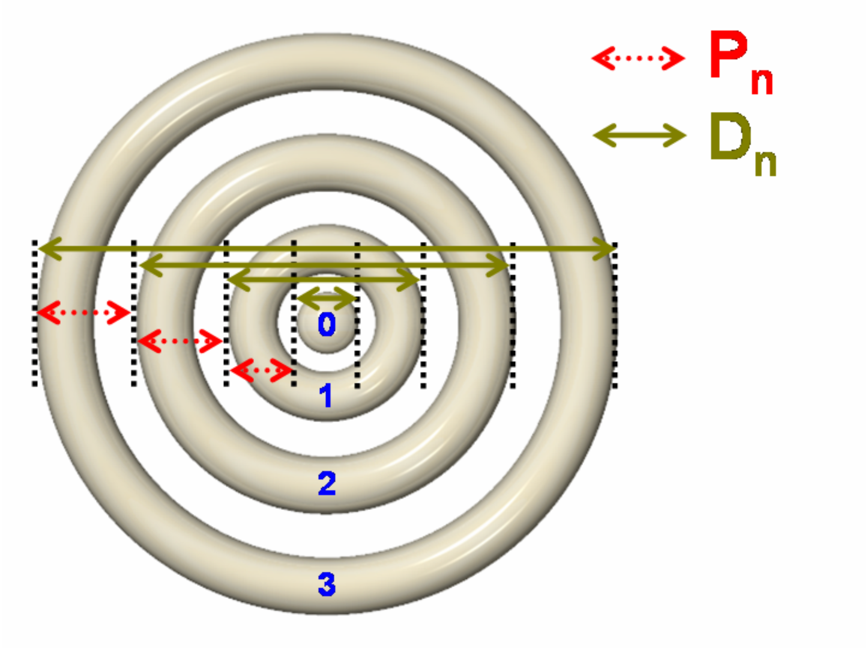

Fig. 5-5 The definition of the period P_n and outer diameter D_n of the concentric ring patterns. Here $P_n = [D_n - D_{n-1}]/2$ or for the inner spheres, $P_0 = D_0/2$.

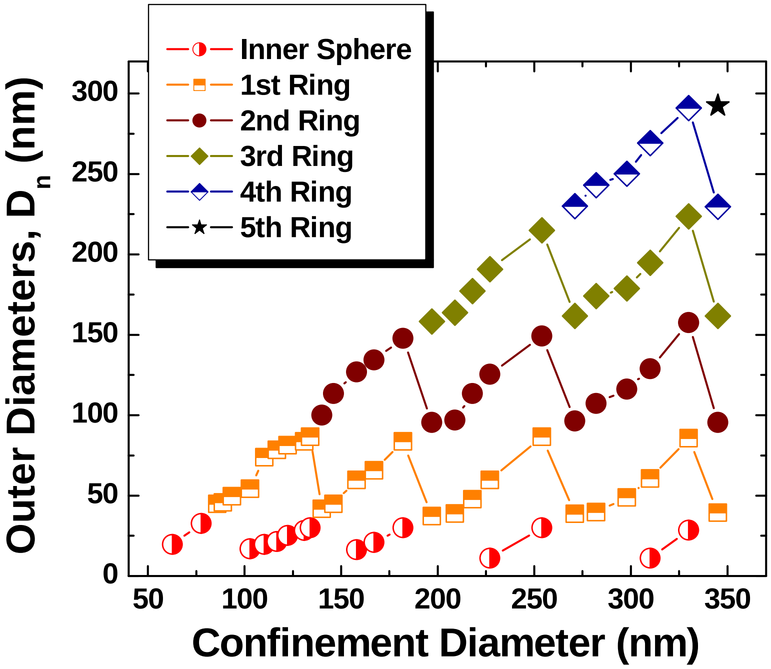

Fig. 5-6 The outer diameter D_n of each PDMS ring as a function of confinement diameter C.

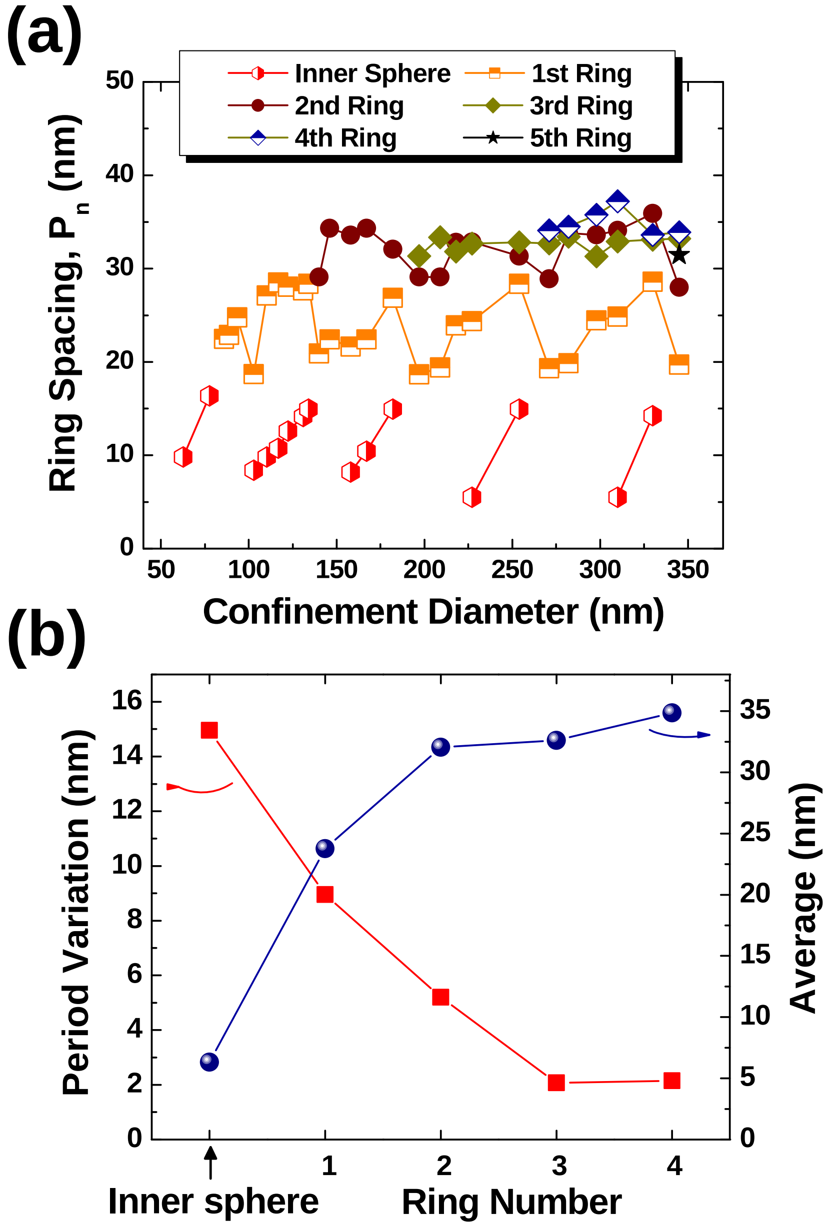

Fig. 5-7 (a) The spacing P_n of each ring as a function of confinement diameter C. For the inner sphere, the radius is plotted. (b) The amplitude of variation ($P_{max}(n)$-$P_{min}(n)$) and the average P_n for each circular ring.

Fig. 5-5 illustrates the definition of the period P_n and outer diameter D_n of the concentric ring patterns, where $P_n = [D_n - D_{n-1}]/2$ and D_n is the outer diameter of ring n. Figure 5-6 and 5-7a respectively show the variation of D_n and P_n with C. The standard deviation of measurements of ring dimensions at a given C are in the range 0.3 – 3 nm. For C=60 or 77 nm, only a PDMS sphere appears, for 86 nm< C < 94 nm, a single PDMS ring is formed without an inner sphere (so the diameter of the inner sphere is not plotted), and for 102 nm < C <134 nm, the inner sphere reappears, which is replaced by a second ring at C=140 nm. These periodic changes in feature size and the presence or absence of the inner sphere occur throughout the whole range of confinement diameter explored here. The appearance and disappearance of the inner sphere suggest that the inner features are formed later than the outer rings, which would be consistent with other reports that the registration of block copolymer domains occurs first at the edges of lithographic patterns.[26] Each ring therefore templates the ring inside it until the final highly frustrated feature forms at the center.

Figure 5-7b shows the amplitude of variation ($P_{max}(n)$-$P_{min}(n)$) and the average of P_n over the entire range of C that was tested. The spacing of the fourth and higher rings (~34-35 nm) is similar to that of unconfined domains, L_{eq}, but the inner elements show more variation in period, and their average period is smaller. This result differs from that reported for frustrated block copolymers in tall cylindrical pores. For example, the period of lamellar-forming polystyrene-polybutadiene in anodic alumina pores was measured to be greater than the equilibrium period.[33] Simulations of lamellae confined in pores indicate that the lamellar spacing can be smaller or larger than the unconfined period and that the spacing of an inner lamella is larger than that of an outer one.[2]

To analyze the results of Fig. 5-7, an Alexander-de Gennes type formalism was used to determine the effect of domain curvature on the period of a block copolymer, assuming that the total free energy per chain is the sum of the interfacial energy and the chain conformational energy. This approach has been widely adopted for understanding lamellar, cylindrical, and spherical microphases in the strong segregation limit.[22, 39-42] The reference state, wherein the free energy is zero, is the macrophase-separated homopolymers without interfaces between the different polymer blocks, or stretching of the chains. This approach gives an expression for the overall free energy ΔG as a function of domain spacing (λ): (see supplemental information for the derivation)

$$\Delta G(\lambda) = \frac{kT}{a^2}\sqrt{\frac{\chi_{AB}}{6}} \cdot 2Na^3 \cdot \frac{1}{\lambda} + \frac{1}{2}kT \cdot [\frac{\lambda^2}{4Na^2} + \frac{4\sqrt{Na^2}}{\lambda} - 3]. \qquad (1)$$

where k, T, a, N, γ, and Σ denote the Boltzmann constant, the temperature, the Kuhn step size, the total number of Kuhn segments, the interfacial energy/unit area, and the contact area per chain between the two blocks, respectively.

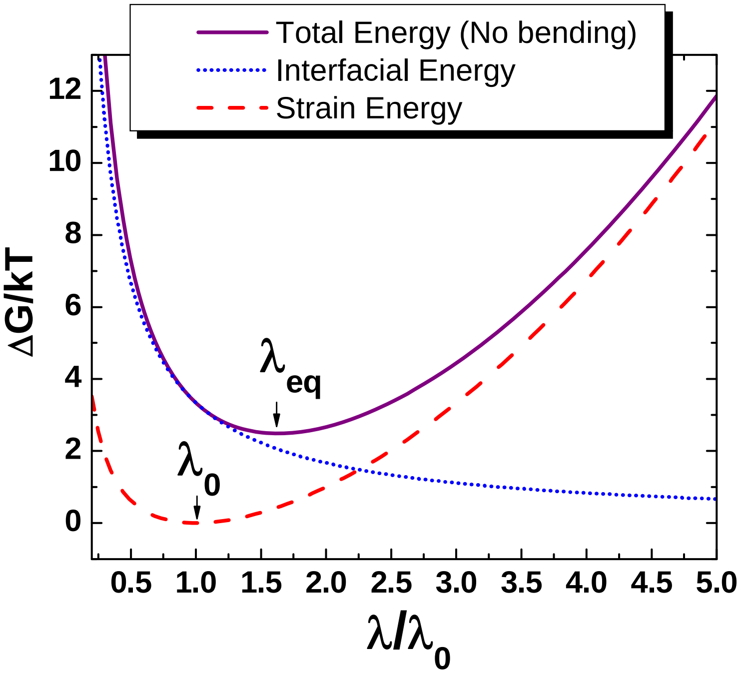

Fig. 5-8 Free energy curves based on eq. (1). Bending energy is not considered here.

Fig. 5-8 plots $\Delta G/kT$ per chain as a function of λ/λ_0, where λ_0 is the domain spacing for relaxed chains, where the strain energy is zero, assuming a=0.59 nm, which is estimated from a weighted mean of the Kuhn step sizes of PS and PDMS reported elsewhere,[43, 44] N=257, and χ=0.26,[37] corresponding to the block copolymer used here. The equilibrium spacing λ_{eq} can be determined by differentiating eq. (3) with respect to λ and equating to zero. The total energy for $\lambda > \lambda_{eq}$ and $\lambda < \lambda_{eq}$ is dominated by the strain energy and interfacial energy components, respectively. λ_{eq} and λ_0 are calculated to be 31.4 and 19.3 nm, respectively. The value for λ_{eq} is in reasonable agreement with the measured unconfined period of L_{eq}=34.2 nm. The results for λ_{eq} and λ_0 are consistent with reports that chains are 10-40% stretched by microphase separation, compared to the relaxed state.[42, 45]

However, bending brings about a significant change in the strain state of the block copolymer chains. Curving a bilayer sheet will place the inner layer in compression and the outer layer in tension, altering the layer thicknesses. For a unit layer of a diblock copolymer, this bending strain can partly be relieved by intermixing of chains, although the relaxation is limited by the connectivity between the blocks. The bending free energy per chain at a radius of curvature R_c was derived by Wang and is slightly modified here as a function of R_c and λ, using the relation $\lambda/2$ = thickness of a diblock copolymer monolayer:[46, 47]

$$\Delta G^{bend}(\lambda, R_c) = \frac{\pi^2}{512}\frac{kT}{Na^2}\lambda^4\frac{1}{R_c^2} \qquad (2)$$

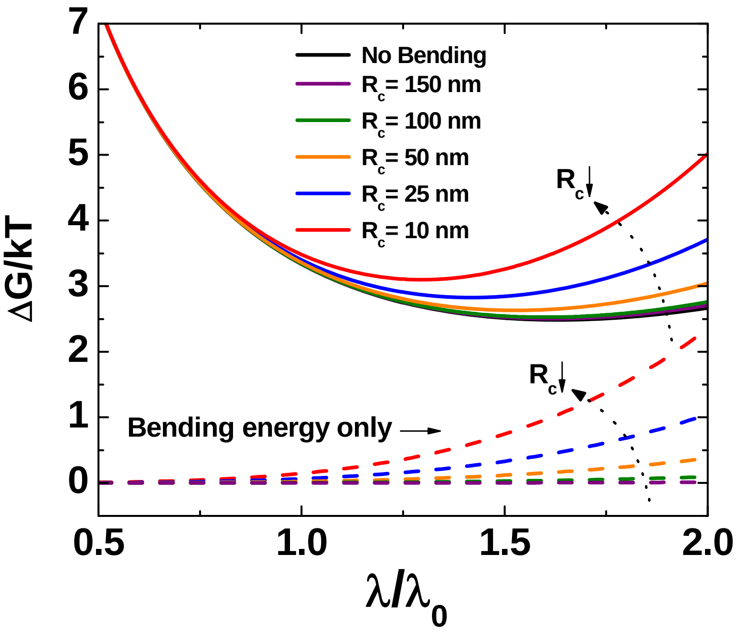

Fig. 5-9 Bending energy and total energy as a function of the radius of curvature (R_c).

As depicted in Fig. 5-9, the bending energy and consequently, the total energy rapidly increase as R_c decreases, especially for large λ since the bending energy scales with λ^4. It should be also noted that the equilibrium spacing $\lambda_{eq}(R_c)$, which corresponds to the minimum of each free energy curve, becomes smaller as R_c decreases. The equilibrium spacing λ_{eq} can be readily obtained as a function of R_c by differentiating the total energy function with respect to λ and setting it to zero. The rapid decrease of λ_{eq} with R_c is plotted in Fig. 5-10, where λ_{eq} has been normalized by the equilibrium spacing for unbent domains. The measured spacings of all the rings in Fig. 5-7a are superposed on this figure, normalized by the period of the unconfined domains (34.2 nm). R_c was taken as the radius at the midpoint of each period, i.e. $R_c = (D_n - P_n)/2$. Despite the approximations of the free energy model, the two data sets share the same trend, in which λ_{eq} increases rapidly with R_c for small R_c, but tends towards the unconfined period for large R_c. The R_c^{-2}

dependence of bending energy can therefore account for the below-equilibrium period at smaller confinement diameters depicted in Fig. 5-7.

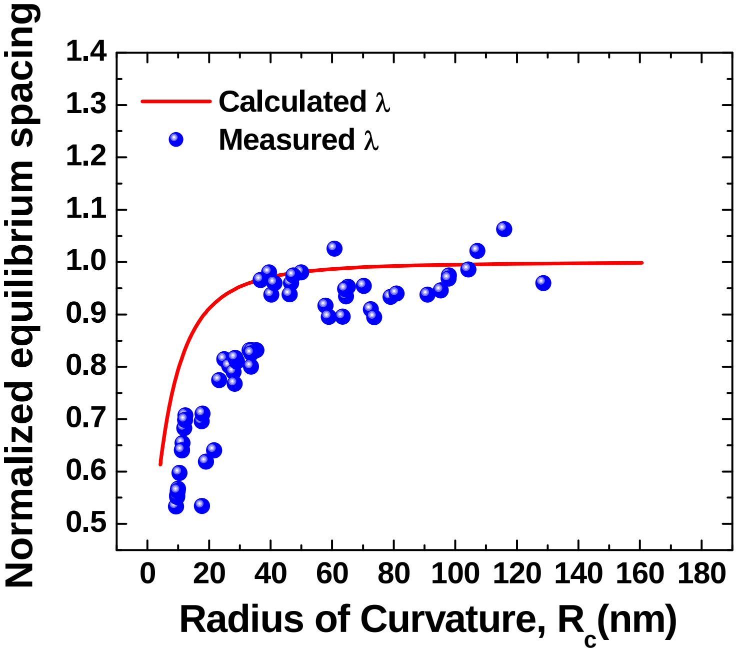

Fig. 5-10 Calculated equilibrium spacing λ_{eq} normalized by its value at large R_c, and measured ring spacing normalized by L_{eq}, as a function of R_c.

5.5 Summary

The formation of well-controlled circular patterns on the nanoscale is important for the fabrication of a range of devices such as sensors, memories, lasers, transistors, and quantum devices. Concentric, smooth ring patterns with tunable dimensions have been formed from a cylinder-forming PS-PDMS diblock copolymer under confinement in shallow circular trenches. The effects of confinement diameter and commensurability on the diameter and period of the concentric rings are analyzed using a free energy model that includes interfacial, strain, and bending energies. This work provides a simple process for the fabrication of nanoscale circular patterns with very narrow linewidth using a much coarser-scale template, and may facilitate the miniaturization of a variety of microelectronic devices.

References

[1] C. T. Black, R. Ruiz, G. Breyta, J. Y. Cheng, M. E. Colburn, K. W. Guarini, H. C. Kim, Y. Zhang, "Polymer self assembly in semiconductor microelectronics", *IBM Journal of Research and Development 51*, p. 605 (2007)

[2] D. Sundrani, S. B. Darling, S. J. Sibener, "Hierarchical assembly and compliance of aligned nanoscale polymer cylinders in confinement", *Langmuir 20*, p. 5091 (2004)

[3] C. T. Black, "Self-aligned self assembly of multi-nanowire silicon field effect transistors", *Applied Physics Letters 87*, p. 163116 (2005)

[4] T. Deng, C. T. Chen, C. Honeker, E. L. Thomas, "Two-dimensional block copolymer photonic crystals", *Polymer 44*, p. 6549 (2003)

[5] V. Gowrishankar, N. Miller, M. D. McGehee, M. J. Misner, D. Y. Ryu, T. P. Russell, E. Drockenmuller, C. J. Hawker, "Fabrication of densely packed, well-ordered, high-aspect-ratio silicon nanopillars over large areas using block copolymer lithography", *Thin Solid Films 513*, p. 289 (2006)

[6] C. Osuji, C. Y. Chao, I. Bita, C. K. Ober, E. L. Thomas, "Temperature-dependent photonic bandgap in a self-assembled hydrogen-bonded liquid-crystalline diblock copolymer", *Advanced Functional Materials 12*, p. 753 (2002)

[7] M. M. Miller, G. A. Prinz, S. F. Cheng, S. Bounnak, "Detection of a micron-sized magnetic sphere using a ring-shaped anisotropic magnetoresistance-based sensor: A model for a magnetoresistance-based biosensor", *Applied Physics Letters 81*, p. 2211 (2002)

[8] J. Llandro, T. J. Hayward, D. Morecroft, J. A. C. Bland, F. J. Castano, I. A. Colin, C. A. Ross, "Quantitative digital detection of magnetic beads using pseudo-spin-valve rings for multiplexed bioassays", *Applied Physics Letters 91*, p. 203904 (2007)

[9] J. G. Zhu, Y. F. Zheng, G. A. Prinz, "Ultrahigh density vertical magnetoresistive random access memory (invited)", *Journal of Applied Physics 87*, p. 6668 (2000)

[10] F. J. Castano, D. Morecroft, W. Jung, C. A. Ross, "Spin-dependent scattering in multilayered magnetic rings", *Physical Review Letters 95*, p. 137201 (2005)

[11] Z. C. Wen, H. X. Wei, X. F. Han, "Patterned nanoring magnetic tunnel junctions", *Applied Physics Letters 91*, p. 122511 (2007)

[12] H. Watanabe, C. Manabe, T. Shigematsu, M. Shimizu, "Dual-probe scanning tunneling microscope: Measuring a carbon nanotube ring transistor", *Applied Physics Letters 78*, p. 2928 (2001)

[13] M. T. Hill, H. J. S. Dorren, T. de Vries, X. J. M. Leijtens, J. H. den Besten, B. Smalbrugge, Y. S. Oei, H. Binsma, G. D. Khoe, M. K. Smit, "A fast low-power optical memory based on coupled micro-ring lasers", *Nature 432*, p. 206 (2004)

[14] P. J. Pauzauskie, D. J. Sirbuly, P. D. Yang, "Semiconductor nanowire ring resonator laser", *Physical Review Letters 96*, p. 4 (2006)

[15] Y. AHARONOV, "Significance of Electromagnetic Potentials in the Quantum Theory", *Physical Review 115*, p. 485 (1959)

[16] L. P. Levy, G. Dolan, J. Dunsmuir, H. Bouchiat, "Magnetization of Mesoscopic Copper Rings - Evidence for Persistent Currents", *Physical Review Letters 64*, p. 2074 (1990)

[17] K. A. Matveev, A. I. Larkin, L. I. Glazman, "Persistent current in superconducting nanorings", *Physical Review Letters 89*, p. 096802 (2002)

[18] A. Fuhrer, S. Luescher, T. Ihn, T. Heinzel, K. Ensslin, W. Wegscheider, M. Bichler, "Energy spectra of quantum rings", *Nature 413*, p. 822 (2001)

[19] R. J. Warburton, C. Schaflein, D. Haft, F. Bickel, A. Lorke, K. Karrai, J. M. Garcia, W. Schoenfeld, P. M. Petroff, "Optical emission from a charge-tunable quantum ring", *Nature 405*, p. 926 (2000)

[20] M. Farhoud, J. Ferrera, A. J. Lochtefeld, T. E. Murphy, M. L. Schattenburg, J. Carter, C. A. Ross, H. I. Smith, "Fabrication of 200 nm period nanomagnet arrays using interference lithography and a negative resist", *Journal of Vacuum Science & Technology B 17*, p. 3182 (1999)

[21] Y. S. Jung, C. A. Ross, "Orientation-controlled self-assembled nanolithography using a polystyrene-polydimethylsiloxane block copolymer", *Nano Letters 7*, p. 2046 (2007)

[22] J. Y. Cheng, A. M. Mayes, C. A. Ross, "Nanostructure engineering by templated self-assembly of block copolymers", *Nature Materials 3*, p. 823 (2004)

[23] R. A. Segalman, H. Yokoyama, E. J. Kramer, "Graphoepitaxy of spherical domain block copolymer films", *Advanced Materials 13*, p. 1152 (2001)

[24] L. Rockford, S. G. J. Mochrie, T. P. Russell, "Propagation of nanopatterned substrate templated ordering of block copolymers in thick films", *Macromolecules 34*, p. 1487 (2001)

[25] M. P. Stoykovich, M. Muller, S. O. Kim, H. H. Solak, E. W. Edwards, J. J. de Pablo, P. F. Nealey, "Directed assembly of block copolymer blends into nonregular device-oriented structures", *Science 308*, p. 1442 (2005)

[26] C. T. Black, O. Bezencenet, "Nanometer-scale pattern registration and alignment by directed diblock copolymer self-assembly", *IEEE Transactions on Nanotechnology 3*, p. 412 (2004)

[27] G. M. Wilmes, D. A. Durkee, N. P. Balsara, J. A. Liddle, "Bending soft block copolymer nanostructures by lithographically directed assembly", *Macromolecules 39*, p. 2435 (2006)

[28] X. H. He, M. Song, H. J. Liang, C. Y. Pan, "Self-assembly of the symmetric diblock copolymer in a confined state: Monte Carlo simulation", *Journal of Chemical Physics 114*, p. 10510 (2001)

[29] B. Yu, P. C. Sun, T. C. Chen, Q. H. Jin, D. T. Ding, B. H. Li, A. C. Shi, "Confinement-induced novel morphologies of block copolymers", *Physical Review Letters 96*, p. 138306 (2006)

[30] K. Shin, H. Q. Xiang, S. I. Moon, T. Kim, T. J. McCarthy, T. P. Russell, "Curving and frustrating flatland", *Science 306*, p. 76 (2004)

[31] Y. Y. Wu, G. S. Cheng, K. Katsov, S. W. Sides, J. F. Wang, J. Tang, G. H. Fredrickson, M. Moskovits, G. D. Stucky, "Composite mesostructures by nano-confinement", *Nature Materials 3*, p. 816 (2004)

[32] Y. Y. Wu, T. Livneh, Y. X. Zhang, G. S. Cheng, J. F. Wang, J. Tang, M. Moskovits, G. D. Stucky, "Templated synthesis of highly ordered mesostructured nanowires and nanowire arrays", *Nano Letters 4*, p. 2337 (2004)

[33] H. Q. Xiang, K. Shin, T. Kim, S. I. Moon, T. J. McCarthy, T. P. Russell, "Block copolymers under cylindrical confinement", *Macromolecules 37*, p. 5660 (2004)

[34] F. Q. Zhu, G. W. Chern, O. Tchernyshyov, X. C. Zhu, J. G. Zhu, C. L. Chien, "Magnetic bistability and controllable reversal of asymmetric ferromagnetic nanorings", *Physical Review Letters 96*, p. 027205 (2006)

[35] D. K. Singh, R. V. Krotkov, H. Xiang, T. Xu, T. P. Russell, M. Tuominen, "Arrays of ultrasmall metal rings", *Nanotechnology 19*, p. 245305 (2008)

[36] T. L. Bucholz, Y. L. Loo, "Phase behavior of near-monodisperse semifluorinated diblock copolymers by atom transfer radical polymerization", *Macromolecules 39*, p. 6075 (2006)

[37] T. Nose, "Coexistence Curves of Polystyrene Poly(Dimethylsiloxane) Blends", *Polymer 36*, p. 2243 (1995)

[38] C. M. Chan, Polymer Surface Modification and characterzation, 1st ed., Hanser Publishers (1994)

[39] S. Alexander, "Polymer Adsorption on Small Spheres - Scaling Approach", *Journal De Physique 38*, p. 977 (1977)

[40] P. G. Degennes, "Conformations of Polymers Attached to an Interface", *Macromolecules 13*, p. 1069 (1980)

[41] A. Frischknecht, G. H. Fredrickson, "Microphase boundaries and chain conformations in multiply branched diblock copolymers", *Macromolecules 32*, p. 6831 (1999)

[42] S. P. Gido, D. W. Schwark, E. L. Thomas, M. D. Goncalves, "Observation of a Nonconstant Mean-Curvature Interface in an Abc Triblock Copolymer", *Macromolecules 26*, p. 2636 (1993)

[43] R. Matsuno, H. Otsuka, A. Takahara, "Polystyrene-grafted titanium oxide nanoparticles prepared through surface-initiated nitroxide-mediated radical polymerization and their application to polymer hybrid thin films", *Soft Matter 2*, p. 415 (2006)

[44] T. J. Senden, J. M. di Meglio, P. Auroy, "Anomalous adhesion in adsorbed polymer layers", *European Physical Journal B 3*, p. 211 (1998)

[45] E. Helfand, Z. R. Wasserman, "Block Co-Polymer Theory .6. Cylindrical Domains", *Macromolecules 13*, p. 994 (1980)

[46] Z. G. Wang, "Response and Instabilities of the Lamellar Phase of Diblock Copolymers under Uniaxial-Stress", *Journal of Chemical Physics 100*, p. 2298 (1994)

[47] Z. G. Wang, S. A. Safran, "Curvature Elasticity of Diblock Copolymer Monolayers", *Journal of Chemical Physics 94*, p. 679 (1991)

[48] S. J. Clarson, J. A. Semlyen, "Siloxane Polymers", *PTR Prentice Hall, Inc.*(1993)

Chapter 6

Self-assembled pattern-generation of dots using a spherical block copolymer

6.1 Introduction

Following Moore's law, the transistor density and hence the computing power of integrated circuits have scaled exponentially with time.[1] However, optical lithography technology, which has sustained Moore's law over the last half century, is reaching a limit in pattern resolution. Unconventional lithography techniques are therefore required to enable the next generations of microelectronic device fabrication. The critical requirements are scalability, high throughput, low cost, and compatibility with existing fabrication techniques.

During the past decade, films of self-assembled diblock copolymers (BCPs) have attracted significant attention for lithography applications because they can generate ordered microdomains with sizes below 30 nm by thermodynamically-driven microphase separation.[2-14] [15] In this application, two-dimensional arrays or monolayers of microdomains are desirable to facilitate pattern transfer.[4, 7, 12, 13, 16] Typically, self-assembled BCP microdomain arrays possess only short range order, and thus to make technologically useful structures with long range order and accurate registration, BCPs may be templated using features formed by another lithography technique.[4, 5, 9, 10, 12-14, 16, 17] The most common templates are chemical[5, 14, 18, 19] or topographic[4, 8, 9, 12, 13, 16] patterns defined by electron beam lithography or optical lithography. Chemical templates can regulate the orientation and position of BCP microdomains to high precision[5, 14, 18, 19] in BCP films consisting of out-of-plane cylinders or lamellae, in which both blocks contact the chemically-patterned substrate. Topographic patterns, with or without substrate surface functionalization, use spatial confinement to impose long range ordering in BCPs of many morphologies including in-plane cylinders and spheres,[4, 8, 9, 12, 13, 16] and can also form three dimensional assemblies, [20-23] including morphologies such as rings, spirals, disks and hollow cylinders that are not found in bulk.[20-22, 24, 25]

This chapter describes the templated self-assembly of 0-dimensional patterns using a sphere-forming block copolymer. As shown in chapter 2, long-range ordering induced by the linear templates patterned with interference lithography will be first presented. This is a very simple and scalable approach since such templates can be readily fabricated with conventional optical lithography tools. However, although the dot patterns have a single-grain structure within a trench, the inter-trench registration of dots is deficient since the ordering of block copolymer spheres in each trench occurs independently. Thus, a novel graphoepitaxy technique, which utilizes sparsely-arranged post arrays as guiding templates, is introduced. This approach can achieve seamless nanostructures over a large area since the lithographically-defined posts are indistinguishable from the self-assembly patterns due to the similarity in chemical compositions.

6.2 Experimental

Self-assembly based on 1D templates and solvent-annealing

Si substrates with 40-nm deep trenches with a periodicity of 1.2 μm were fabricated using a Lloyd's Mirror interference lithography system with a He-Cd laser (λ = 325 nm).[12] The direct and reflected laser beams exposed grating patterns into a 200 nm thick PFI-88 photoresist (Sumitomo Chemical

Co.), which were transferred into the Si substrates through a CF_4 reactive ion etching with a working pressure of 10 mTorr and a power of 200 W. The native oxide surfaces were treated by hydroxy-terminated PDMS homopolymer with molecular weight 5 kg/mol, which was spun-cast on the substrates and annealed at 170 °C for 15 hours, then washed with toluene to remove unreacted polymers, leaving a 3 - 4 nm thick grafted PDMS layer.[12] A sphere-forming PS-PDMS BCP (Polymer Source, Inc.) with total molecular weight of 51.5 kg/mol, minority block volume fraction f_{PDMS}=16.5%, and polydispersity index of 1.04 was used. BCP thin films with a thickness of 30 nm were obtained by spin-casting toluene solutions of 1.5% by weight of the block copolymer on the substrates, then the BCP films were treated with toluene vapor at room temperature for 20 minutes. The annealed film was treated with a 5 sec, 50 W CF_4 plasma followed by a 22 sec, 90 W O_2 plasma to remove the PDMS surface layer and selectively eliminate the PS block, which reveals oxidized PDMS microdomains in the trenches. [12]

Self-assembly based on 0D templates and thermal annealing

To template the BCP, a sparse 2D array of posts was generated by electron-beam lithography of a 40 nm thick hydrogen silsesquioxide (HSQ) resist layer on a Si substrate. HSQ is a electron-beam-sensitive spin-on-glass material that forms a SiO_2-like material by electron-beam exposure. Development discloses the well-defined posts, without requiring further etching or processing. The same sphere-forming block copolymer was used. The block copolymer was spin coated to a thickness of around 50 nm and thermally annealed at 200°C to obtain a monolayer of PDMS spheres with a pitch of 38 nm and a diameter of 20 nm. A similar two-step reactive ion etching was employed to remove the PS block and generate oxidized PDMS dots.

6.3 1D templates to guide 0D self-assembling patterns

Figure 2a-c shows scanning electron microscopy (SEM) images of self-assembled PDMS spheres in the trenches after removing the PS. The average diameter of the structures is 17.9 ± 1.1 nm, and the average center-to-center distance is 35.0 ± 1.5 nm. Each 960 nm wide trench templates 32 rows of hexagonally ordered dots, and figure 2d shows the fast Fourier transform of the image. The height of the dots is around 10 - 11 nm. For each trench the close-packed directions of the array align parallel to the trench walls, which is consistent with previous reports.[8, 17] The close-packed orientation, which has the lowest free energy at the brush-coated wall/BCP interface due to the minimization of chain stretching by maximizing the number of spheres in contact with the brush,[17] first aligns parallel with the trench walls and propagates during self-assembly. However, for narrow trenches with incommensurate widths, different orientations, where the closed-packed direction is rotated from the trench wall, are also observed, probably due to the dominant effect of strain energy in incommensurate templates.

Ordering was achieved within 20 mins solvent annealing time, which is faster than the previously reported solvent annealing times required for sphere-forming BCPs.[26-28] The very low surface energy of the PDMS brush adsorbed on the substrate may enhance the chain mobility, contributing to the fast self-assembly. In general, the throughput of block copolymer nanolithography is believed to be limited by the annealing process, but this result suggests that annealing time may be reduced by employing solvent annealing and a brush treatment.

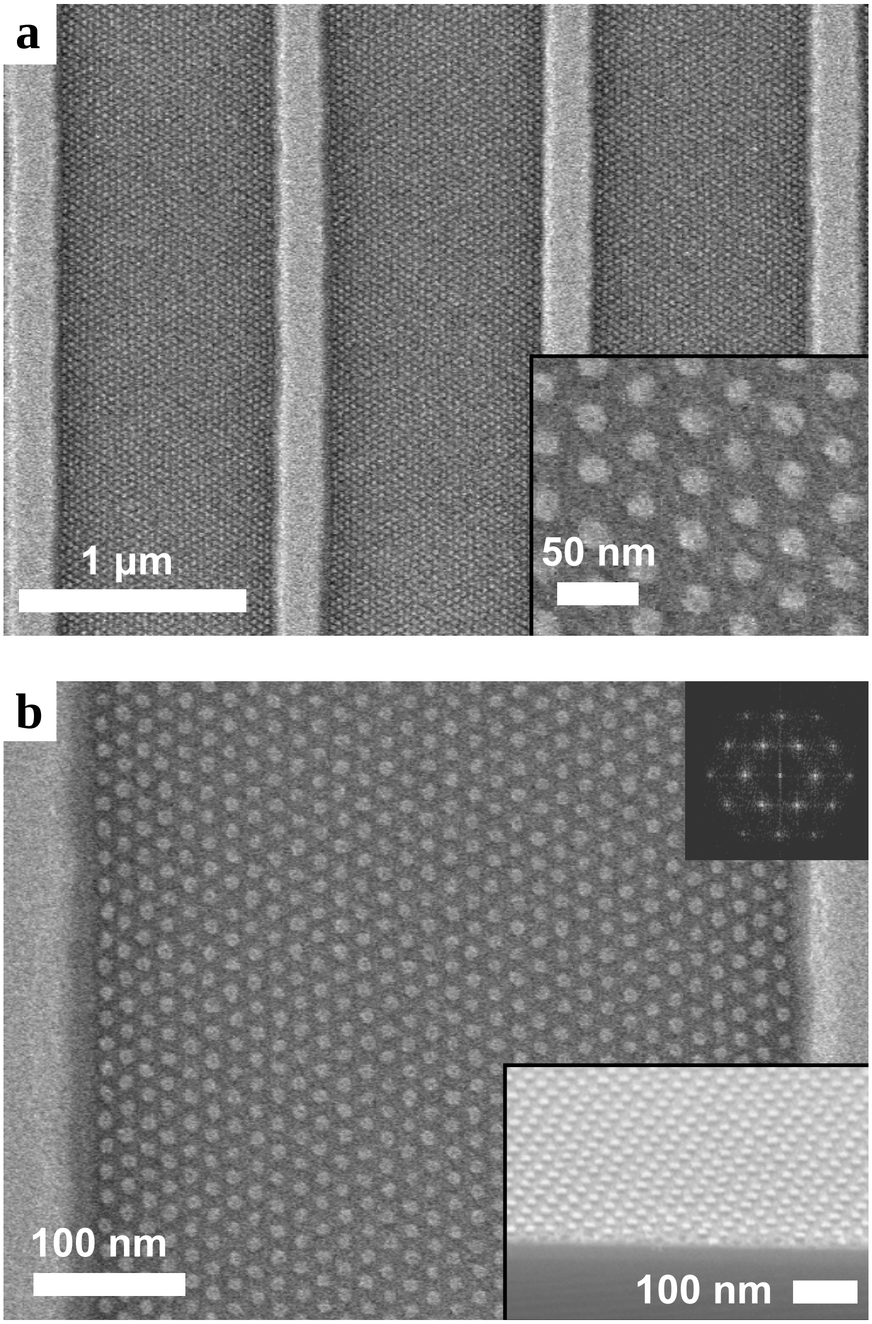

Fig. 6-1 SEM images of self-assembled block copolymer patterns after reactive ion etching. The oxygen plasma selectively removes the PS matrix block and oxidizes the PDMS spheres. The upper inset shows the fast Fourier transform (FFT) of (b)

6.4 Sparse 0D templates to guide 0D self-assembling patterns

Figure 6-2 shows the morphology of self-assembled PDMS dots after O_2 reactive ion etching. It presents hexagonal short-range ordering, which is supported by the FFT pattern. The patterns are composed of ~200 nm-scale domains with different orientations, which are arbitrarily determined.

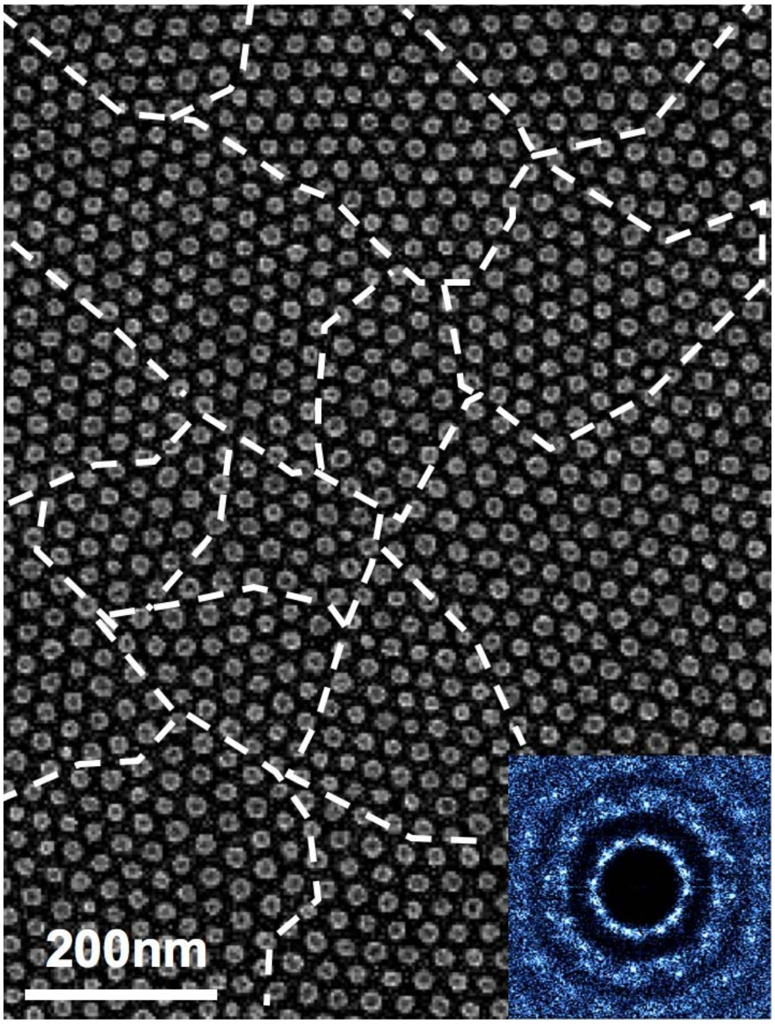

Fig. 6-2 Scanning-electron micrograph (SEM) of a disordered monolayer of BCP spherical domains formed on a flat surface, i.e. without templating. The boundaries between different grain orientations are indicated with dashed lines. The inset is a two-dimensional (2D) Fourier transform of the domain positions which shows the absence of long range order.

Figure 6-3 schematically describes the registration of block copolymer spheres in the 2D arrays of HSQ post arrays patterned with electron beam lithography. An important requirement is for the surface of the posts to show affinity towards one of the blocks of the BCP, which can be easily established by chemical functionalization of the template surface by the dehydration reaction between hydroxy-terminated PS or PDMS and the post arrays. The template was functionalized with short PDMS homopolymer chains, and a post substitutes for a PDMS sphere. In an another design, an array of larger-diameter posts was functionalized with a PS homopolymer brush. PDMS brush treatment is preferred due to better and faster ordering of the microdomain arrays, compared to PS-coated or uncoated substrates since higher diffusivity can be obtained due to lower surface energy of PDMS brush, which minimizes the interaction between the self-assembling polymers and the patterned substrates. [12] The grafting of PDMS brush increases the sizes of the posts and requires fabricating 10-nm-scale nanostructures, which is smaller than those of BCP spheres. High-resolution patterning at this level can be achieved by electron-beam lithography. [29]

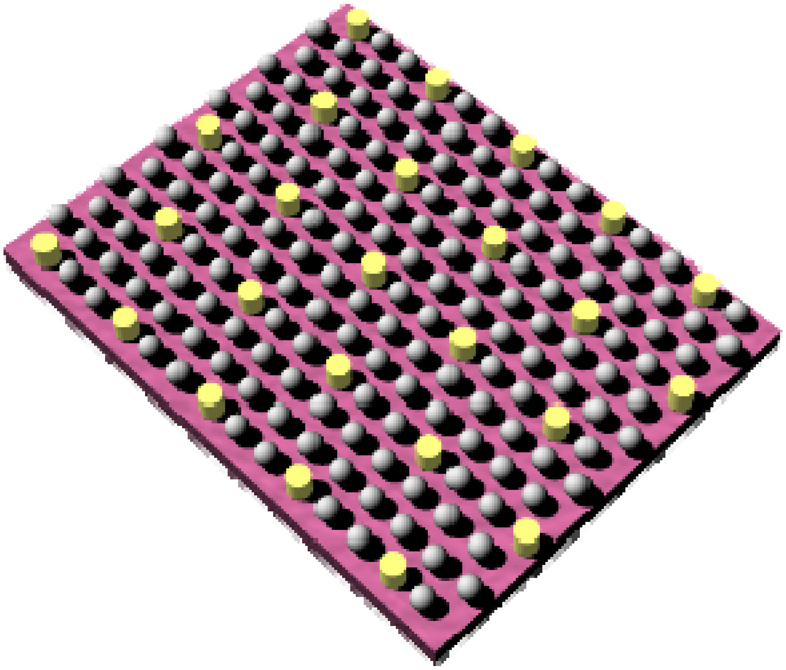

Fig. 6-3 Schematic of the 0D post arrays to guide block copolymer spheres.

Electron beams were employed to pattern a negative electron resist, HSQ. HSQ films were spun coated on silicon substrates, and single-pixel dots with a controlled dose were exposed in a Raith 150 electron-beam lithography facility. The exposed films were developed in a developer, as reported previously.[29] As a result, well-defined template arrays as shown in Fig. 6-4 were obtained. The template substrates were treated in an O_2/He plasma ashing chamber (50 W, 2min) to get rid of possible organic residues.

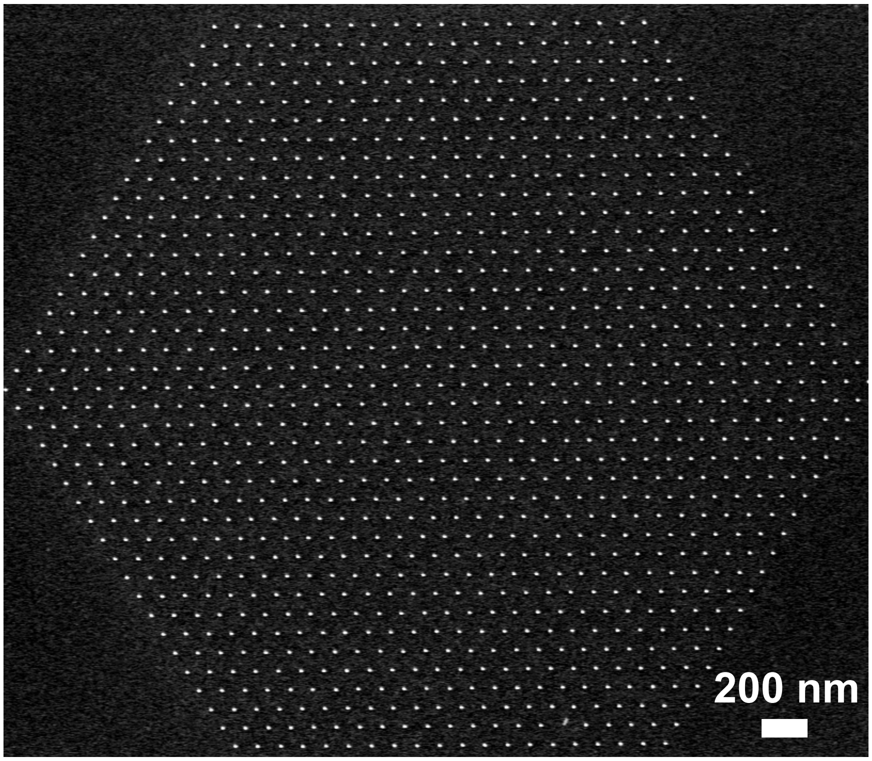

Fig. 6-4 HSQ post arrays patterned with electron beam lithography.

Figure 6-5 shows that functionalized e-beam posts with suitable size can excellently template the self-assembly of a block copolymer lattice. In contrast to the patterns on smooth substrates, long-range ordering was achieved on the template substrate. This demonstration may be significant in that this self-assembly technique can markedly increase the throughput of e-beam lithography by reducing the writing time, which is one of the main obstacles for considering e-beam lithography for a useful nanofabrication method. However, the disadvantage of this approach may be the heterogeneous nature of the patterns due to the slight difference in chemical composition and height between the HSQ posts and the PDMS microdomains. Thus, more optimizations to reduce the gaps may be needed for potential applications.

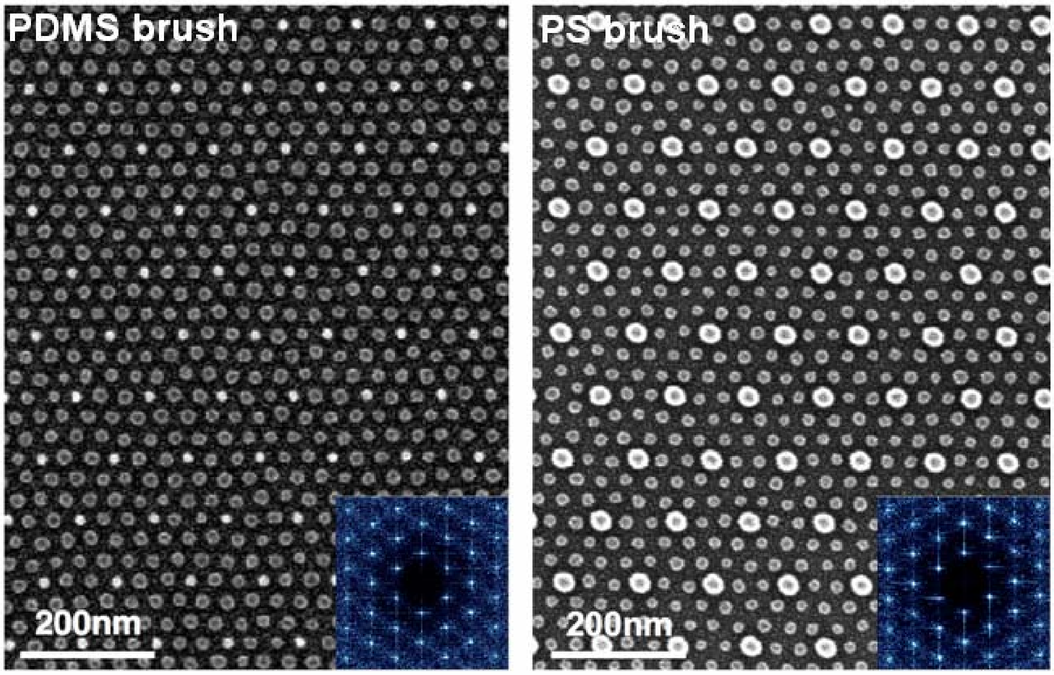

Fig. 6-5 SEM images of ordered BCP spheres formed within a sparse 2D lattice of HSQ posts (brighter dots). The substrate and post surfaces were functionalized with a PDMS brush layer (left), which corresponds to the schematic in Fig. 6-3, and with a PS brush layer (right). The insets show the 2D Fourier transforms in which the high frequency components originate from the post lattice.

6.5 Effects of commensurability on the orientation

It is necessary to consider the best arrangement of templates to ensure the formation of a 'single grain' BCP lattice with controlled period and orientation. For a hexagonally arranged template of period L_{post}, and a hexagonal BCP microdomain array of period $L(< L_{\text{post}},)$, the commensurability between the BCP lattice and the template lattice is a function of the ratio L_{post}/L. If L_{post} is the exact multiple of L, the lattice vectors of the template and the BCP array are parallel with each other, as shown in Fig. 6-5 ($L_{\text{post}}/L=3$), and the angle(θ) between the post lattice basis vector and the

BCP microdomain lattice basis vector is zero. However, for non-integer values of L_{post}/L, various orientational relationships ($\theta \neq 0$) can be obtained. Considering the hexagonal arrangements, L_{post}/L can be calculated by a simple expression

$$L_{post} / L = \sqrt{i^2 + j^2 + ij}$$

where i and j are the two basis vectors in the hexagonal BCP microdomain lattice. The angle θ between the post lattice and BCP microdomain lattice can be expressed as

$$\theta = \arccos\left(\frac{2i + j}{2\sqrt{i^2 + j^2 + ij}}\right)$$

A notation of the bracket form $\langle i\, j\rangle$ is used to specify the arrangement of BCP lattices formed within pre-defined e-beam post lattices. For example, the structures shown in Fig. 6-5 would be labeled as $\langle 3\ 0\rangle$ under this notation, which implies that a BCP microdomain lattice vector is perfectly parallel to the post lattice vector and that the magnitude is 1/3 of that of the post lattice vector. For each of $\langle i\, j\rangle$ orientations, the number of PDMS spheres templated by one post is given by $i^2 + j^2 + ij - 1$. For example, 8 BCP microdomains are templated by one post for the $\langle 3\ 0\rangle$ lattice and 18 for the $\langle 3\ 2\rangle$ lattice.

Figure 6-6 shows the SEM images of BCP spheres templated by e-beam posits with varied spacing. The orientation, θ was investigated within the spacing range of 66 - 184 nm, which corresponds to $L_{\mathrm{post}}/L = 1.65$ to 4.6. At a given L_{post}, BCP microdomains choose the orientation that best satisfies the commensurability condition. Figure 6-7 and Table 6-1 present the calculated commensurate lattice configurations in the range of $1.5 < L_{\mathrm{post}}/L < 5$. For non-zero orientations, +θ and - θ are equivalent to each other. Thus, it is difficult to obtain a single-grain structure with these non-zero orientations.

This phenomenon resembles the rotation in crystallographic orientations between two lattice systems with different lattice parameters. For example, an epitaxial (0001) ZnO film grown on a (0001) Al_2O_3 substrate shows a 30° rotation of ZnO basal planes with respect to the sapphire substrate in order to reduce the strain energy. [30]

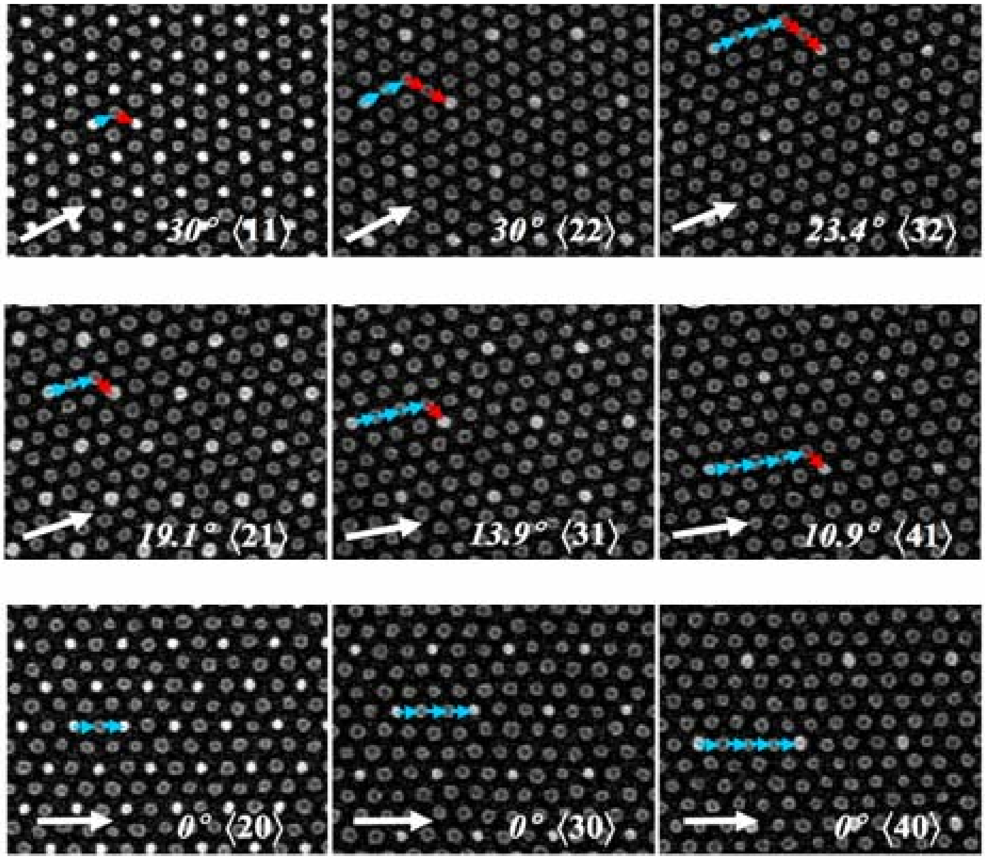

Fig. 6-6 Plan-view SEM images of all the commensurate configurations for the L_{post}/L_o ratio range of 1.65 to 4.6. The white arrows show the orientation angle between the BCP microdomain lattice and the post lattice and are 120-nm long. The brighter dots are the oxidized HSQ posts, while the darker dots correspond to oxidized PDMS spherical domains. The blue and red arrows indicate the basis vectors of the BCP microdomain lattice, and sum to one horizontal basis vector of the post lattice.

6.6 Analyses on the orientational relationship

BCP chains allow some degree of a tensile or compressive strain in order to fit within a given template, which was observed in geometrically confined spherical, cylindrical or lamellar arrays. [8, 31] It was reported that confined BCP arrays are capable of exhibiting significant strain, with tension being easier to accommodate than compression,[32] which may be related with the asymmetry of strain energy for compression and tension. This compliance produces a larger number of arrangements to be observed at a given L_{post}/L than the specific configurations that Fig. 6-7 and Table 6-1 would suggest.

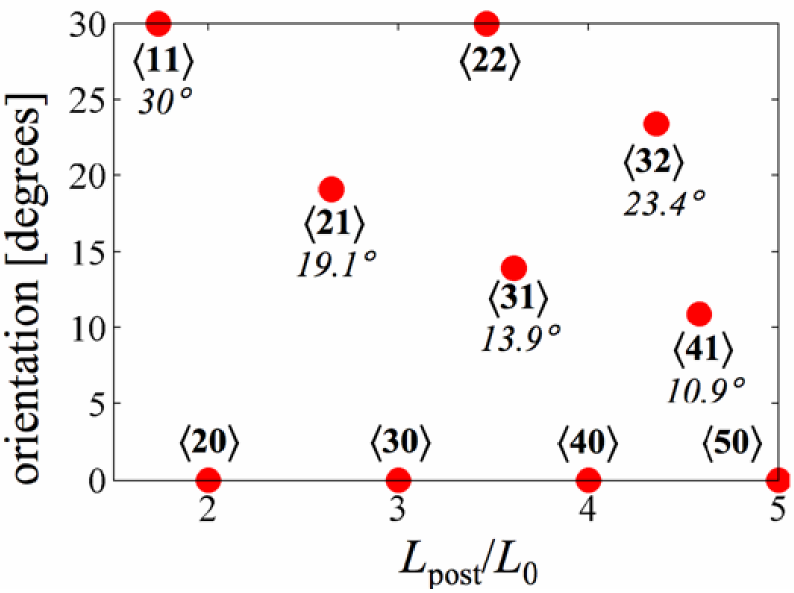

Fig. 6-7 Calculated orientations at which the BCP microdomain lattice is commensurate with the post lattice, as a function of L_{post}/L_o. The BCP lattice is commensurate with the post lattice when the post lattice basis vectors of length L_{post} can be represented as integer multiples, <*i j*>, of the BCP lattice basis vectors of length L_o. Due to the 6-fold symmetry of the BCP lattice, the angular span of 0 to 30° is sufficient to represent all possible non-degenerate orientations.

Lattice	*i*	*j*	L_{post}/L	θ [°]
⟨10⟩	1	0	$\sqrt{1} = 1.00$	0.0
⟨11⟩	1	1	$\sqrt{3} = 1.73$	30.0
⟨21⟩	2	1	$\sqrt{7} = 2.65$	19.1
⟨31⟩	3	1	$\sqrt{13} = 3.61$	13.9
⟨32⟩	3	2	$\sqrt{19} = 4.36$	23.4
⟨41⟩	4	1	$\sqrt{21} = 4.58$	10.9
⟨51⟩	5	1	$\sqrt{31} = 5.57$	9.0
⟨43⟩	4	3	$\sqrt{37} = 6.08$	25.3
⟨52⟩	5	2	$\sqrt{39} = 6.24$	16.1
⟨53⟩	5	3	$\sqrt{49} = 7.00$	21.8
⟨54⟩	5	4	$\sqrt{61} = 7.81$	26.3

Table 6-1 Calculated L_{post}/L and θ for each of <*i j*> vectors.

In order to understand and describe the arrangements that occur, a simple free energy model is introduced for the BCP microdomain lattice as a function of L_{post}/L. Given an ⟨*i j*⟩ configuration and a post spacing such that the commensurate sublattice period L differs from the equilibrium spacing of the BCP on a flat substrate, L_0, the templated BCP may either assume a strained spacing and fit inside the post-lattice, or form local defects and relieve the long-range stress. The free-energy change for straining the BCP lattice can be approximated with an affine deformation model by considering the effect of strain on both the conformational entropy of a polymer chain and the interfacial energy between the BCP domains. The derivation of the free energy expression is described in chapter 3, and leads to

$$\Delta F(\lambda) = \frac{kT}{a^2}\sqrt{\frac{\chi_{eff}}{6}} \cdot 2Ma^3 \cdot \frac{1}{\lambda} + \frac{1}{2}kT \cdot [\frac{\lambda^2}{4Ma^2} + \frac{4\sqrt{Ma^2}}{\lambda} - 3]$$

F_{chain}/kT was then calculated for all the ⟨*i j*⟩ combinations by substituting $L = L_{\mathrm{post}}/\sqrt{i^2 + j^2 + ij}$. These energy curves are plotted in Fig. 6-8A as a function of L_{post}/L_0. The left side of the energy curve is dominated by the interfacial energy and the right side of it follows the strain energy curve. Each $\langle i\ j \rangle$ lattice orientation has an energy-well with a minimum corresponding to the value of L_{post}/L_0 at which the post lattice is the exact multiple of the natural BCP spacing on a flat surface.

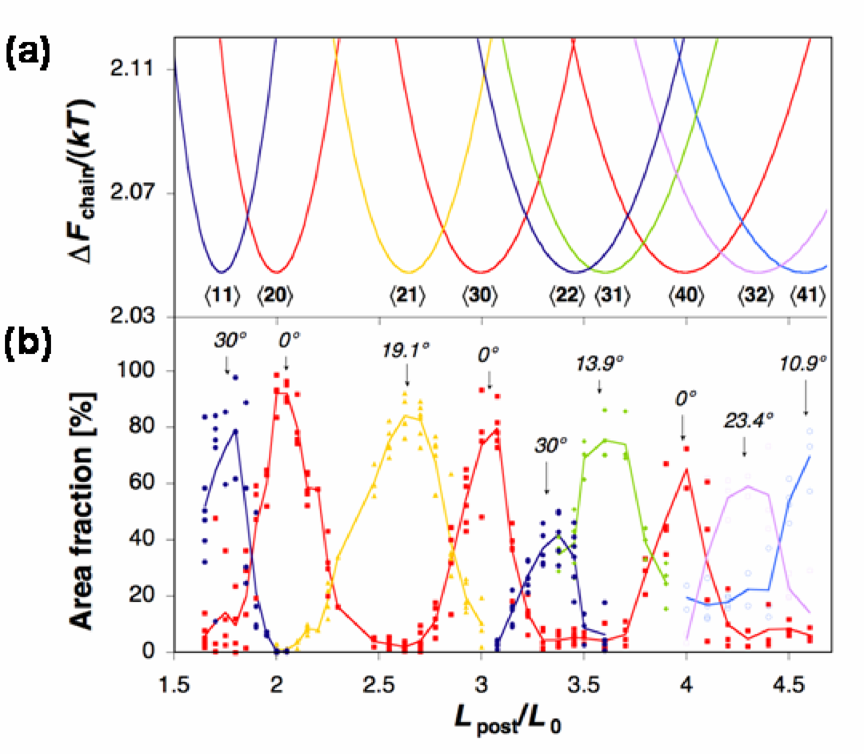

Fig. 6-8 (A) Calculated curves of free energy per BCP chain vs L_{post}/L_0 for each commensurate configuration. Free energy minima occur at L_{post}/L_0 values where the commensurate condition is satisfied without straining the BCP microdomain array. (B) Experimental results showing the area fraction of each $\langle i\ j \rangle$ lattice vs L_{post}/L_0. Each filled circle is a data point obtained by image processing of an SEM image of a 1.3 m by 1.3 m square area of the templated region.

The predictions of this model were compared with the experimental results obtained by preparing templates with a varied post spacing, $L_{\mathrm{post}} = 66$-184 nm ($L_{\mathrm{post}}/L_0 \sim 1.65$-$4.6$) on the same substrate. Having multiple templates on the same substrate ensured the exactly same annealing conditions and a uniform BCP film thickness across all templates with different L_{post} values. The diameter of each template region composed of hexagonally arranged posts was about 4 μm. Scanning electron micrographs often showed more than one BCP microdomain lattice orientation within each post array. Image analysis was used to determine the coordinates and Wigner-Seitz cells for each BCP lattice site, and the area and orientation of each Wigner-Seitz cell was calculated to determine the area fraction of each BCP lattice. Figure 6-8B shows the area fraction of each lattice type as a function of the ratio L_{post}/L_0.

The experimental results and theoretical predictions in Fig. 6-8 were consistent. As the increase of post spacing L_{post}, all the orientations, $\langle 1\ 1\rangle$, $\langle 2\ 0\rangle$, $\langle 2\ 1\rangle$, $\langle 3\ 0\rangle$, $\langle 2\ 2\rangle$, $\langle 3\ 1\rangle$, $\langle 4\ 0\rangle$, $\langle 3\ 2\rangle$ and $\langle 4\ 1\rangle$, which were predicted based on the calculation, were observed. A given lattice type dominated at the L_{post}/L_0 value for which the free energy model predicted a minimum for that lattice type. Two or more orientations are observed if L_{post}/L_0 is higher than 3.5, which can be attribute to decreased slopes of potential wells as the post spacing increases. Thus, the energy barriers separating different BCP orientations became smaller. A similar phenomenon was observed in previous studies with BCP spheres packing in grooves, where n or n+1 rows of spheres were observed to occur degenerately for wider grooves [8]. Even when L_{post}/L_0 is smaller than 3.5, two lattice types also occurred simultaneously if L_{post}/L_0 was intermediate between values corresponding to energy minima, which correspond to commensurate conditions. These results suggest that meeting a commensurability condition is essential to get perfectly ordered dot arrays with precisely controlled orientations and positions.

6.7 Summary

This chapter presented two pathways to provide long-range ordering to sphere-forming block copolymers. The first way utilized micron-scale 1D templates fabricated with optical interference lithography and employed solvent-annealing. The other method applied thermal annealing to the block copolymers templated by hexagonally arranged post arrays patterned with electron beam lithography. Both of the ways include a surface treatment of the templates by end-functionalized homopolymers. The former method can greatly save the cost and time to fabricate the template due to much higher throughput of the optical lithography technique, while the latter approach can provide a better control of the self-assembly and registration of each feature at an exactly desired position at the expense of increased cost for making the templates.

References

[1] G. E. Moore, "Cramming more components onto integrated circuits", *Electronics 38*, p. 114 (1965)

[2] M. Park, C. Harrison, P. M. Chaikin, R. A. Register, D. H. Adamson, "Block copolymer lithography: Periodic arrays of similar to 10(11) holes in 1 square centimeter", *Science 276*, p. 1401 (1997)

[3] T. Thurn-Albrecht, J. Schotter, C. A. Kastle, N. Emley, T. Shibauchi, L. Krusin-Elbaum, K. Guarini, C. T. Black, M. T. Tuominen, T. P. Russell, "Ultrahigh-density nanowire arrays grown in self-assembled diblock copolymer templates", *Science 290*, p. 2126 (2000)

[4] J. Y. Cheng, C. A. Ross, E. L. Thomas, H. I. Smith, G. J. Vancso, "Templated self-assembly of block copolymers: Effect of substrate topography", *Advanced Materials 15*, p. 1599 (2003)

[5] S. O. Kim, H. H. Solak, M. P. Stoykovich, N. J. Ferrier, J. J. de Pablo, P. F. Nealey, "Epitaxial self-assembly of block copolymers on lithographically defined nanopatterned substrates", *Nature 424*, p. 411 (2003)

[6] R. A. Segalman, A. Hexemer, E. J. Kramer, "Edge effects on the order and freezing of a 2D array of block copolymer spheres", *Physical Review Letters 91*, p. 196101 (2003)

[7] C. T. Black, O. Bezencenet, "Nanometer-scale pattern registration and alignment by directed diblock copolymer self-assembly", *IEEE Transactions on Nanotechnology 3*, p. 412 (2004)

[8] J. Y. Cheng, A. M. Mayes, C. A. Ross, "Nanostructure engineering by templated self-assembly of block copolymers", *Nature Materials 3*, p. 823 (2004)

[9] D. Sundrani, S. B. Darling, S. J. Sibener, "Hierarchical assembly and compliance of aligned nanoscale polymer cylinders in confinement", *Langmuir 20*, p. 5091 (2004)

[10] C. T. Black, "Self-aligned self assembly of multi-nanowire silicon field effect transistors", *Applied Physics Letters 87*, p. 163116 (2005)

[11] C. T. Black, R. Ruiz, G. Breyta, J. Y. Cheng, M. E. Colburn, K. W. Guarini, H. C. Kim, Y. Zhang, "Polymer self assembly in semiconductor microelectronics", *IBM Journal of Research and Development 51*, p. 605 (2007)

[12] Y. S. Jung, C. A. Ross, "Orientation-controlled self-assembled nanolithography using a polystyrene-polydimethylsiloxane block copolymer", *Nano Letters 7*, p. 2046 (2007)

[13] I. Bita, J. K. W. Yang, Y. S. Jung, C. A. Ross, E. L. Thomas, K. K. Berggren, "Graphoepitaxy of self-assembled block copolymers on 2D periodic patterned templates", *Science 321*, p. 939 (2008)

[14] R. Ruiz, H. M. Kang, F. A. Detcheverry, E. Dobisz, D. S. Kercher, T. R. Albrecht, J. J. de Pablo, P. F. Nealey, "Density multiplication and improved lithography by directed block copolymer assembly", *Science 321*, p. 936 (2008)
[15] F. S. Bates, G. H. Fredrickson, "Block Copolymer Thermodynamics - Theory and Experiment", *Annual Review of Physical Chemistry 41*, p. 525 (1990)
[16] R. A. Segalman, H. Yokoyama, E. J. Kramer, "Graphoepitaxy of spherical domain block copolymer films", *Advanced Materials 13*, p. 1152 (2001)
[17] R. A. Segalman, A. Hexemer, E. J. Kramer, "Effects of lateral confinement on order in spherical domain block copolymer thin films", *Macromolecules 36*, p. 6831 (2003)
[18] L. Rockford, S. G. J. Mochrie, T. P. Russell, "Propagation of nanopatterned substrate templated ordering of block copolymers in thick films", *Macromolecules 34*, p. 1487 (2001)
[19] M. P. Stoykovich, M. Muller, S. O. Kim, H. H. Solak, E. W. Edwards, J. J. de Pablo, P. F. Nealey, "Directed assembly of block copolymer blends into nonregular device-oriented structures", *Science 308*, p. 1442 (2005)
[20] K. Shin, H. Q. Xiang, S. I. Moon, T. Kim, T. J. McCarthy, T. P. Russell, "Curving and frustrating flatland", *Science 306*, p. 76 (2004)
[21] Y. Y. Wu, G. S. Cheng, K. Katsov, S. W. Sides, J. F. Wang, J. Tang, G. H. Fredrickson, M. Moskovits, G. D. Stucky, "Composite mesostructures by nano-confinement", *Nature Materials 3*, p. 816 (2004)
[22] H. Q. Xiang, K. Shin, T. Kim, S. I. Moon, T. J. McCarthy, T. P. Russell, "Block copolymers under cylindrical confinement", *Macromolecules 37*, p. 5660 (2004)
[23] V. P. Chuang, J. Y. Cheng, T. A. Savas, C. A. Ross, "Three-dimensional self-assembly of spherical block copolymer domains into V-shaped grooves", *Nano Letters 6*, p. 2332 (2006)
[24] B. Yu, P. C. Sun, T. C. Chen, Q. H. Jin, D. T. Ding, B. H. Li, A. C. Shi, "Confinement-induced novel morphologies of block copolymers", *Physical Review Letters 96*, p. 138306 (2006)
[25] Y. S. Jung, W. Jung, C. A. Ross, "Nanofabricated Concentric Ring Structures by Templated Self-Assembly of a Diblock Copolymer", *Nano Lett. 8*, p. 2975 (2008)
[26] S. Park, B. Kim, O. Yavuzcetin, M. T. Tuominen, T. P. Russell, "Ordering of PS-b-P4VP on patterned silicon surfaces", *Acs Nano 2*, p. 1363 (2008)
[27] C. B. Tang, J. Bang, G. E. Stein, G. H. Fredrickson, C. J. Hawker, E. J. Kramer, M. Sprung, J. Wang, "Square packing and structural arrangement of ABC triblock copolymer spheres in thin films", *Macromolecules 41*, p. 4328 (2008)
[28] J. Zhang, B. J. Wang, X. Ju, T. Liu, T. D. Hu, "New observations on the optical properties of PPV/TiO2 nanocomposites", *Polymer 42*, p. 3697 (2001)
[29] J. K. W. Yang, K. K. Berggren, "Using high-contrast salty development of hydrogen silsesquioxane for sub-10-nm half-pitch lithography", *Journal of Vacuum Science & Technology B 25*, p. 2025 (2007)

[30] J. Narayan, K. Dovidenko, A. K. Sharma, S. Oktyabrsky, "Defects and interfaces in epitaxial ZnO/alpha-Al2O3 and AlN/ZnO/alpha-Al2O3, heterostructures", *Journal of Applied Physics 84*, p. 2597 (1998)

[31] G. J. Kellogg, D. G. Walton, A. M. Mayes, P. Lambooy, T. P. Russell, P. D. Gallagher, S. K. Satija, "Observed surface energy effects in confined diblock copolymers", *Physical Review Letters 76*, p. 2503 (1996)

[32] D. J. Kinning, E. L. Thomas, "Hard-Sphere Interactions between Spherical Domains in Diblock Copolymers", *Macromolecules 17*, p. 1712 (1984)

Chapter 7

Fabrication of metallic nanostructures and characterizations

7.1 Introduction

For the last decade, there has been massive interest in inorganic one-dimensional nanostructures,[1-6] and due to their unprecedented properties in the sub-100-nm regime, various kinds of electric, optical, optoelectronic, and biological devices based on nanowires or nanotubes have been demonstrated.[1-3, 5, 7-9] In general, the dimension, composition, and crystallographic orientation of nanowires can be controlled by manipulating the synthetic parameters, such as precursor composition, choice of substrate, temperature, and pressure, during chemical vapor deposition. Highly integrated nanoscale devices demand an effective and reproducible way to orient the one-dimensional building blocks with precise control over orientation and position.[7] For example, electric field or fluidic fluid have been employed to direct nanowires into ordered arrays on substrates.[1, 2, 7, 10, 11] However, these methods generally bring about inherent issues such as broad distributions in the size and properties of synthesized nanowires and incomplete control on the spacing and position after assembly.

Alternatively, templated self-assembly of a block copolymer can generate regular arrays of features with outstanding positional and orientational accuracies. Microphase separation of block copolymers, which is generally driven by thermodynamics, can be induced by the attachment of two or more incompatible blocks in a single polymeric chain. The morphology and length scale of self-assembled patterns usually ranges from 10 to 100 nm and can be controlled by the degree of polymerization and volume fraction. Although typically nonfunctional components remain after a selective removal of one block, the nanoscale features can be extensively used as the templates for fabricating functional nanostructures such as magnetic dots,[12-15] phase-changing chalcogenide dots,[16] or silicon nanowires[17] via reactive ion etching, ion-milling or lift-off processes. However, these methods have challenges such as the requirement of multiple steps of patterning processes[12-15] or the limitation in film deposition method and condition[16] or restrictions to the materials whose plasma etching chemistry is well-known.[17] Recently, several metallic nanowires were fabricated through selective incorporation of metallic elements into a polypyridine block and elimination of organic components by oxygen plasma treatment. Still, this technique cannot be applied to making structures with multicompositions or multilayers and has a possibility of impurity inclusion during metal incorporation and oxygen plasma treatment processes.

This chapter suggests an efficient way to obtain various kinds of one-dimensional metallic patterns using linear templates obtained from self-assembling poly(styrene-b-dimethylsiloxane) (PS-PDMS). The polymer presents an exceptional degree of ordering due to the very large χ parameter of PS-PDMS (χ~0.26 at 300K).[18] The oxidized PDMS patterns were transferred to various kinds of metallic thin films such as Ti, W, Ni, Pt, Au, and Al. This technique may be compatible with various film deposition methods e.g. chemical vapor deposition, sputtering, evaporative deposition, pulsed-laser deposition, or spin-coating.

This chapter also describes a simple route to fabricate thin films with well ordered nanopores (antidot arrays) using self-assembled block copolymer lithography and pattern transfer processes. Long-range ordering of a sphere-forming block copolymer is accomplished using a brush-coated one-dimensional topographic template and solvent annealing, and the spheres are used to make nanoporous patterns through a pattern reversal process. Examples of Ti, Pt, Ta, W, silica and magnetic Co and Ni antidot arrays are presented. A second image reversal process was used to form Ni dot arrays. This general method may be used to make a diverse range of nanopatterned films which can be useful in applications including via formation in integrated circuits, filters, plasmonic and photonic bandgap structures, catalysts, templates, sensors, and solar cells.[19-27].

Another important geometry for device applications is that consisting of single or concentric rings. Several devices based on ring shaped features have been designed, including sensors,[28, 29] magnetic memories,[30-32] transistors,[33] optical memories,[34] ring resonator lasers,[35] and structures used to investigate quantum interference phenomena such as the Aharonov–Bohm effect[36] or persistent currents.[37, 38] As an example, three-dimensionally confined semiconductor quantum rings (or coupled concentric double quantum rings) that behave as artificial atoms have discrete energy levels that can be engineered for performing quantum computations or realizing advanced electronic or optoelectronic devices.[39, 40] Self-assembly of thin films of diblock copolymers typically yields patterns consisting of parallel lines or close-packed arrays of dots or holes, and the formation of 2D ring-shaped patterns suitable for device fabrication is less well explored. A self-assembly-based method for creating ring patterns of controlled geometry may enable the scaling of ring-shape devices, with consequent improvements in speed or power consumption.

This chapter also deals with how these ring patterns can be incorporated into a device fabrication process by forming and characterizing a high-density ($1.1\times10^9/\text{cm}^2$) array of ferromagnetic cobalt rings. This fabrication technique is tolerant to a wide range of processing conditions due to the robustness of the oxidized PDMS patterns, and is applicable to diverse types of materials and deposition techniques.

7.2 Experimental

Block copolymer self-assembly

The self-assembly processes of block copolymers for generating lines, dots, and rings are described in detail in previous chapters.

Metal patterning

Metallic thin films such as Pt, Ti, W, Ta, Co, and Ni with a thickness of 55-70 nm were deposited using an RF sputtering system (base pressure = 1×10^{-8} Torr, working pressure = 2×10^{-3} Torr, and power = 300 W) on top of the block copolymer patterns and etched with a 450 W 10 mTorr CF_4 plasma for 2 - 25 mins depending on the etch rate and film thickness. Initially the metallic films were slowly sputter-etched by ionized CF_x species, but after the buried block copolymer patterns were exposed to the plasma, they were removed much faster than the metallic films by forming by forming volatile SiF_x.[41]. As a result, various metallic nanowires, nanoporous metallic films, and ferromagnetic rings were obtained. A nanoporous Ni pattern was transferred into a 20-nm-thick silica film using a 200 W CF_4 plasma. After the completion of etching, the Ni mask was removed with a sulfuric-acid-based nickel etchant at a temperature of 50 °C. A patterned Ti template was used for making Ni dots by depositing a 70-nm-thick Ni film onto the Ti and performing the pattern-reversal process once more.

Magnetic hysteresis loop measurement and simulations

Magnetic hysteresis loops were obtained from a vibrating sample magnetometer (ADE, model 1660) at room temperature. Micromagnetic modeling was carried out using the two dimensional OOMMF software from NIST, with 2×2 nm^2 cells, 10 nm thick, and saturation magnetization M_s = 1400 emu/cm^3, random anisotropy $K_1 = 5.2\times10^6$ erg/cm^3, exchange constant A = 1×10^{-6} erg/cm, and damping coefficient of $\alpha = 0.5$.

7.3 Fabrication of metallic nanowires and characterization

The process to fabricate metallic nanowires with the PS-PDMS block copolymers is described in Fig. 7-1. Solvent-annealing and reactive ion etching processes were used to generate well-ordered arrays of oxidized PDMS patterns with a width of 14-15 nm, which was previously reported in detail.[18]

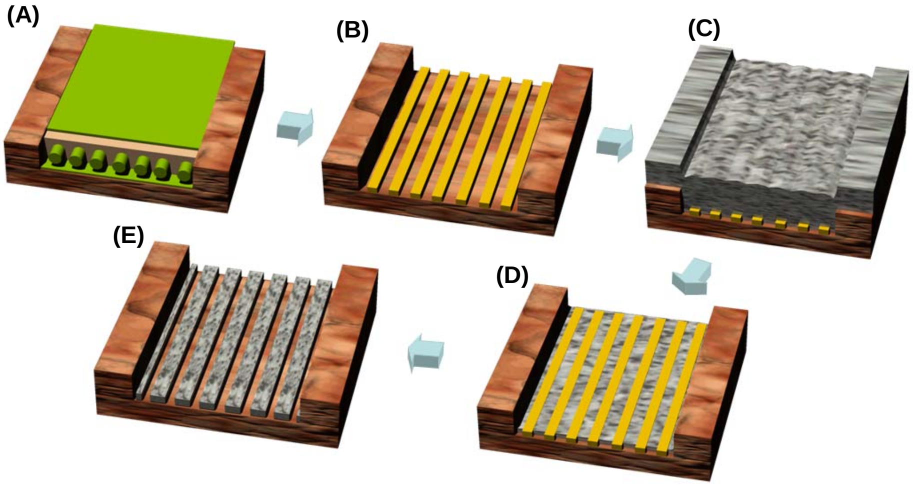

Fig. 7-1 A pattern-reversal process to fabricate metallic nanowires. (A) Self-assembly of a cylinder-forming block copolymer, (B) two-step reactive ion etching to reveal oxidized PDMS line patterns, (C) metal deposition by sputtering, (D) CF_4 plasma etching, and (E) metallic nanowires with the reverse image of the original PDMS patterns.

On top of the well-defined PDMS lines, various kinds of 60-70 nm thick metallic films such as Ti, W, Co, Pt, Ni, Cu, Au, and Al were sputter-deposited. As an example, Fig. 7-2a and b demonstrate a W thin film deposited on the oxidized PDMS patterns. From the images, it can be seen that the surface of the W film shows a small fluctuation of film topography and is smoother than the underlying PDMS patterns presented in Fig. 2-6c. This phenomenon may be caused by adatom diffusion to reduce the surface area of the film. This self-smoothening process is an essential part of the image reversal process depicted in Fig. 7-1. A 450W, CF_4 plasma was applied on the deposited film surface to sputter the material off, which is a purely mechanical etching process since most of the metals used in this study do not form volatile product by fluoridation. The only exception is W, which forms volatile WF_6 with a boiling point of 17.1 °C. The etch rates at the power of 450W range from 2.3 to 25 nm/min depending on metals. The CF_4 plasma etching again smoothens the film surface since the peaks are etched faster than the valleys due to a shadowing effect. In Fig. 7-2c, very little topographic fluctuation remains after etching the thickness of around 30-40 nm. Small dents, which are formed during film deposition, occur with a density of 1-3 /μm^2. Those defective areas can locally change the final line width after patterning and degrade the reliability, although their influence is much reduced during plasma etching due to the plasma-induced smoothening process. This suggests that a larger film thickness would improve the quality of patterns. These automatic self-smoothening effects during film deposition and etching keep the height of nanostructured patterns from being much smaller than that of the original oxidized PDMS patterns. The estimated etch rate for the oxidized PDMS processed under the same condition is around 140 nm/min, and thus once the buried templates are exposed to the CF_4 plasma, they are etched away in six seconds.

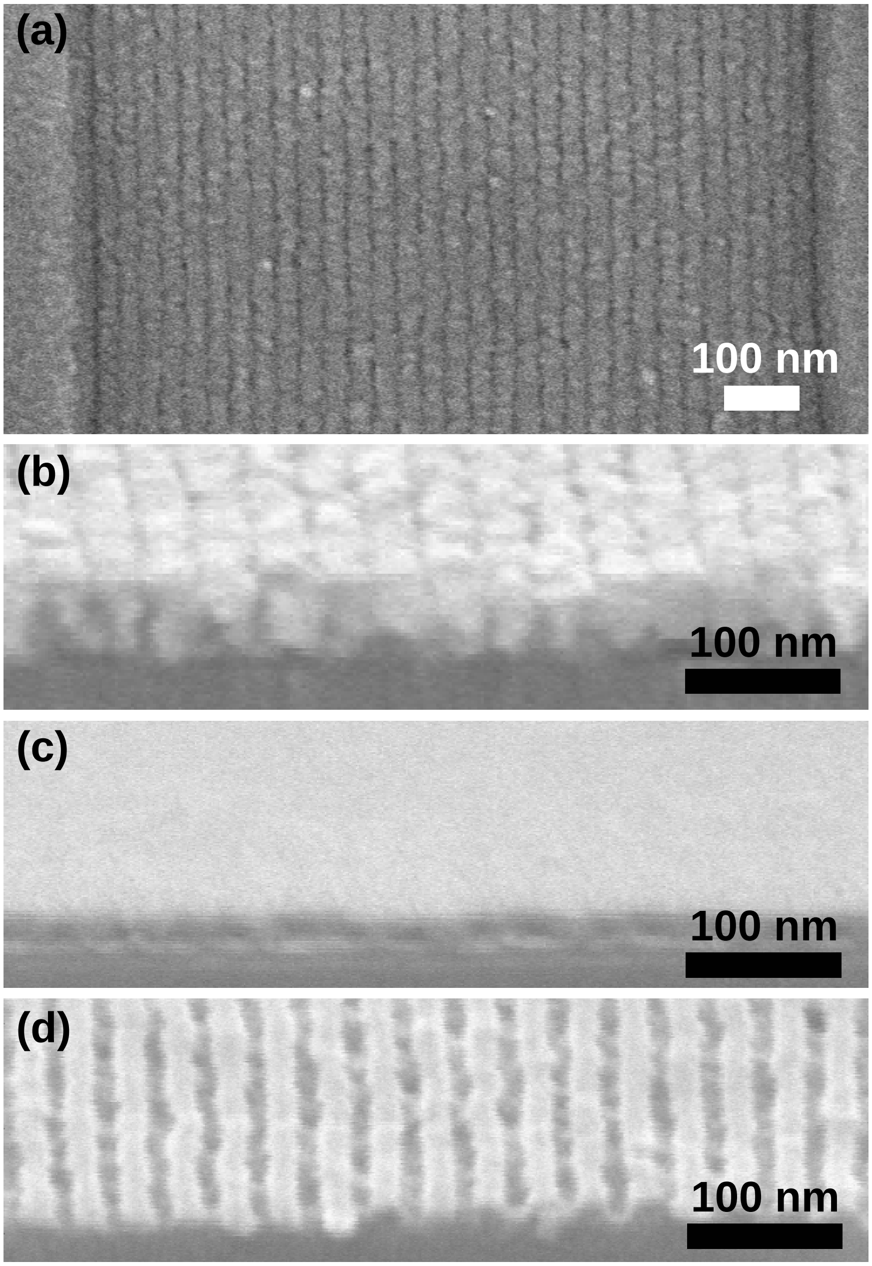

Fig. 7-2 An example of metal patterning. SEM images of (a), (b) W deposited on the oxidized PDMS patterns, (c) smoothened W surface by CF_4 plasma etching, and (d) W nanowires.

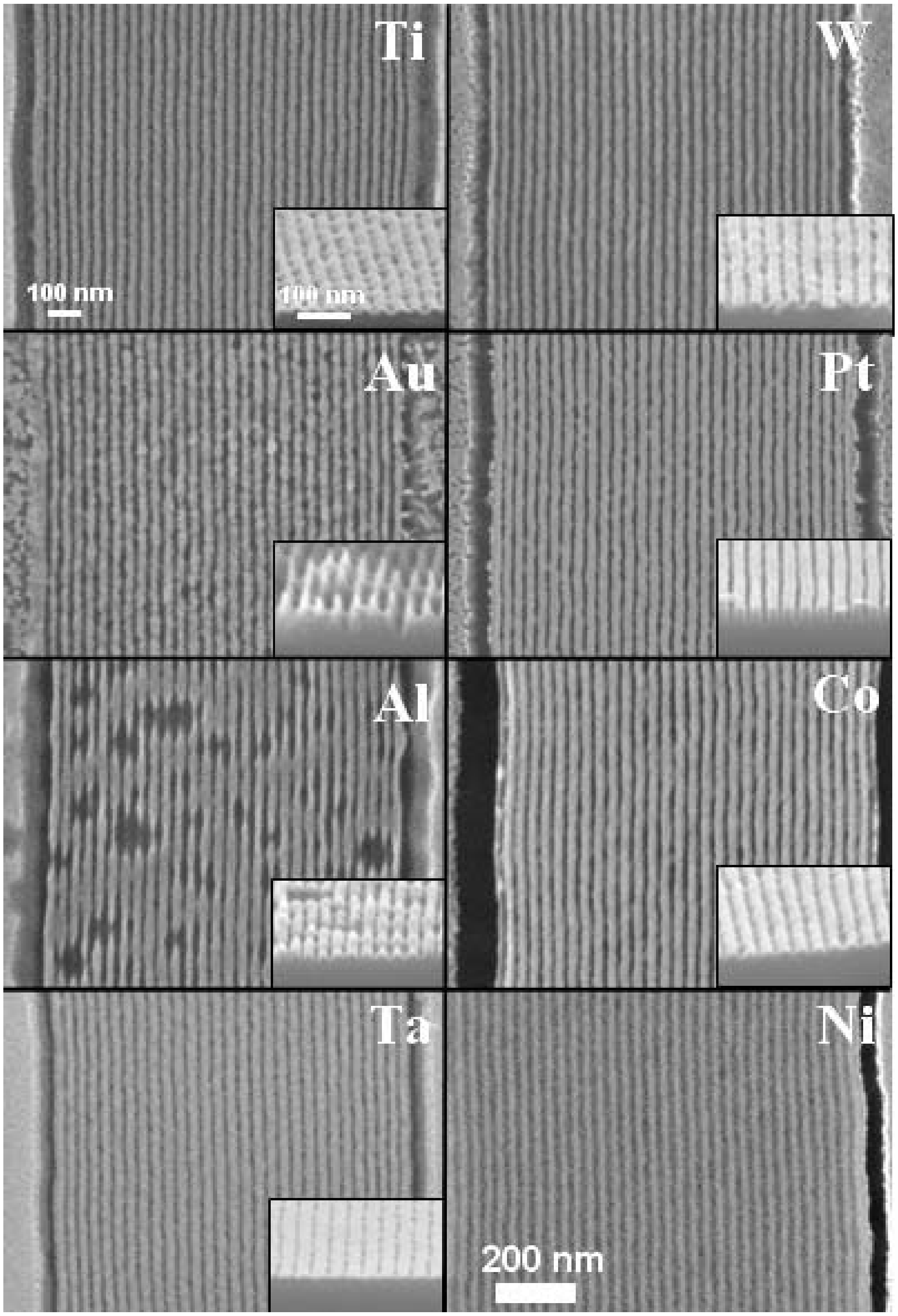

Fig. 7-3 Various metallic nanowires fabricated with the pattern-reversal technique.

Fig. 7-3 demonstrates various kinds of metallic nanowire patterns obtained by the patterning process described so far. After the selective removal of the oxidized PDMS templates, uniformly aligned metallic nanowires with a pattern density of 2.94×10^5 cm^{-1} can be fabricated. Fig. 7-3 also shows superior pattern quality of the metals with relatively higher melting points (Ti, W, Pt, Co, Ni, and Ta) compared to Au or Al. The GISAXS spectrum of the Pt nanowires shown on Fig. 7-4 presents well-defined diffraction patterns with high-order peaks, which implies the uniform formation of Pt nanowires through this pattern-transfer technique. However, the slightly diffuse diffraction pattern of Fig. 7-4 than that of Fig. 2-8 may be due to relatively rough edge of Pt patterns compared to the original self-assembly lines.

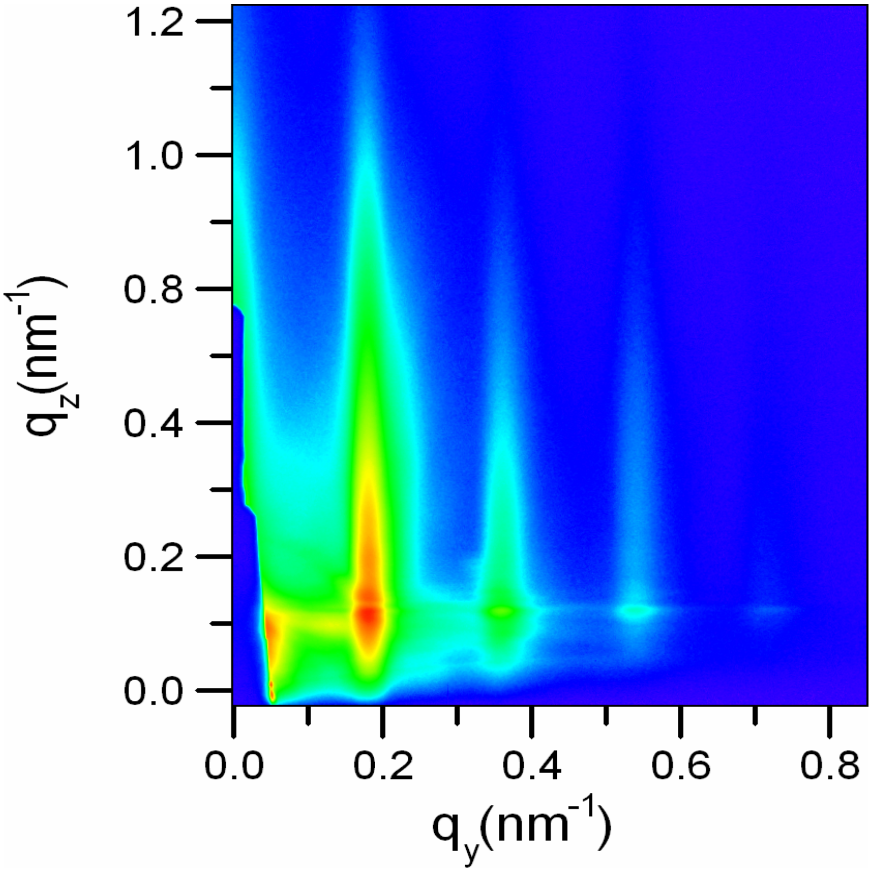

Fig. 7-4 Grazing incidence small-angle X-ray scattering patterns of Pt nanowires

Magnetic nanowires can potentially be used for high-density magnetic memory devices.[42, 43] The Ni nanowires maintained their ferromagnetism after patterning, as shown Fig. 7-5. The coercivity of the Ni nanowires were 470 Oe when the magnetic field was applied in parallel with the nanowires, while that of a Ni film with the same thickness (= 12 nm) was only 17 Oe. The coercivity enhancement can be attributed to the shape anisotropy effect in the Ni nanowires.

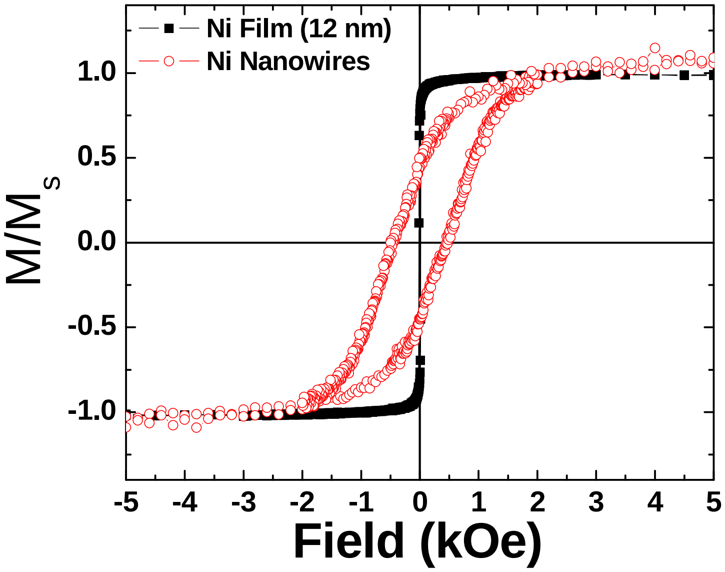

Fig. 7-5 Magnetic hysteresys curves of a flat Ni film and Ni nanowires.

7.4 Fabrication of nanoporous metallic films and characterization

The well-ordered dot patterns in chapter 6 can be converted into a nanoporous metallic thin film via a pattern reversal process as shown in Fig. 7-6.

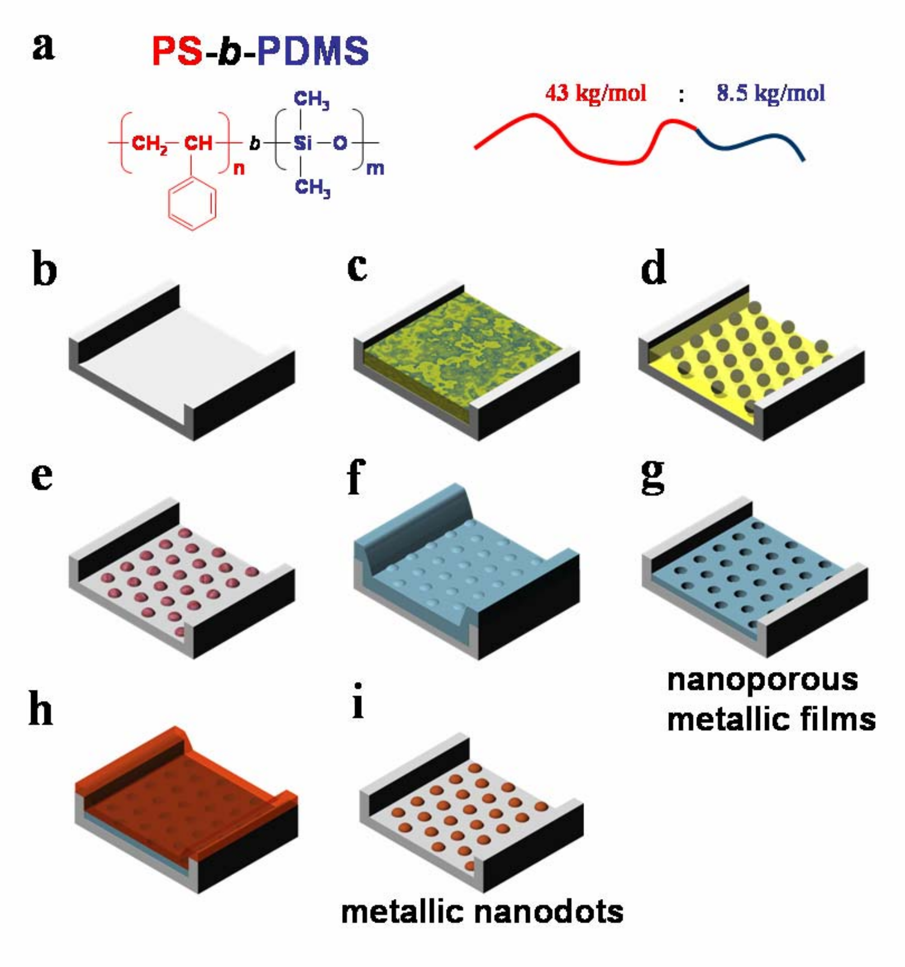

Fig. 7-6 Schematic representation of the fabrication process. (a) The chemical structure of the PS-PDMS block copolymer, (b) a lithographically-patterned trench, (c) a spin-coated block copolymer film in the trench, (d) well-ordered block copolymer microdomain array after solvent-annealing, (e) an array of oxidized PDMS dots after CF_4 and O_2 reactive ion etching processes, (f) a metal film deposited on the dot array, and (g) a porous metallic film after a high power CF_4 plasma etching. The porous film can be used for Ni dot fabrication by employing a second pattern-reversal step. (h) Ni film deposition and (g) a high power CF_4 plasma etching reveals the Ni dot array.

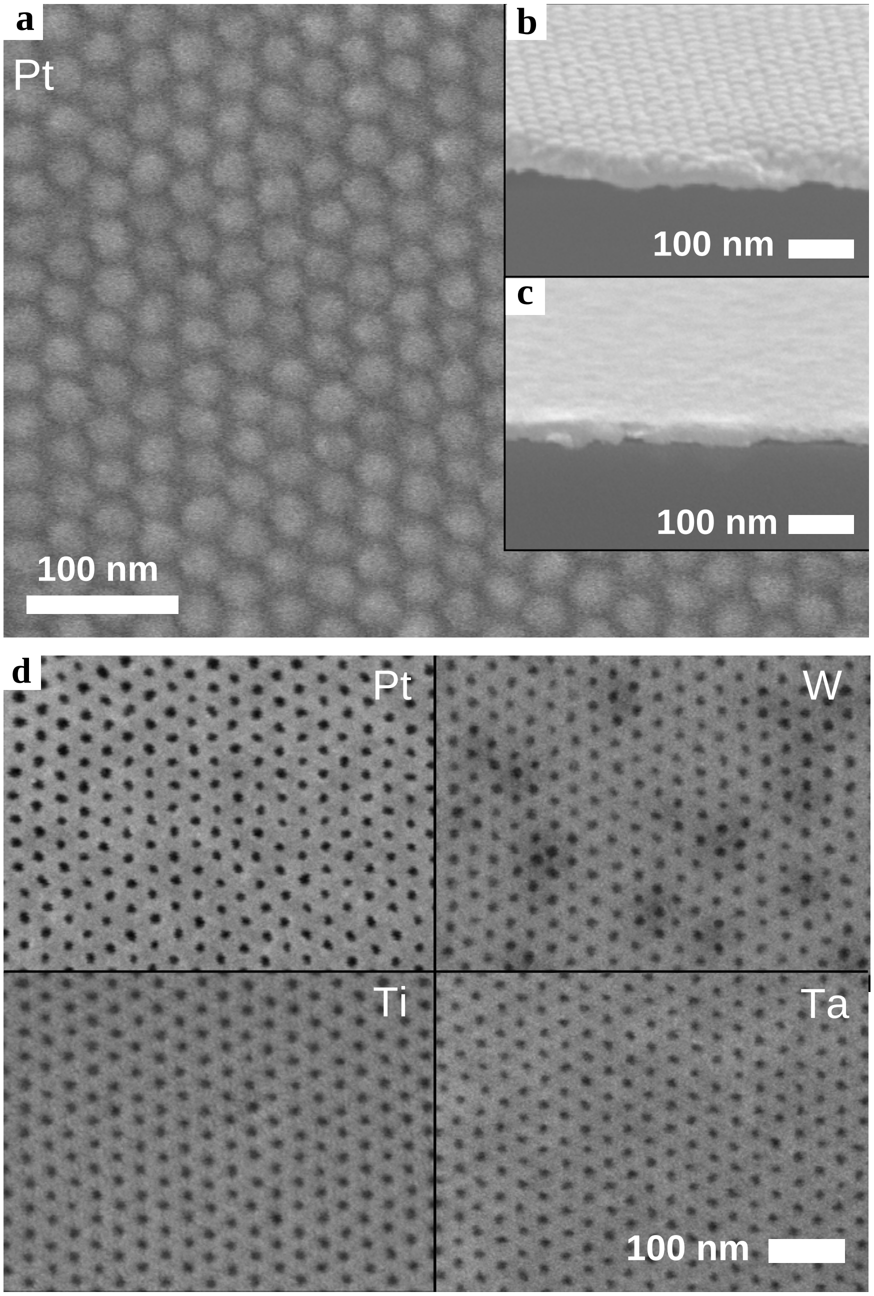

Fig. 7-7 SEM images of (a), (b) a Pt thin film sputter-deposited on oxidized PDMS spheres, (c) smoothed surface of the Pt after a high power CF_4 plasma treatment, (d) various metallic thin films with nanopores after the selective removal of the PDMS template, (e) Ti nanowire patterns, (f) a nanoporous Ni film on SiO_2, (g) patterned SiO_2 via CF_4 reactive ion etching and Ni wet-etching, and (h) a Ni dot array.

Figures 7-7a and b show images of a 55 nm thick Pt thin film deposited on the oxidized PDMS patterns, with a topography indicative of the buried BCP patterns. A similar pattern-reversal technique using 450W CF_4 plasma was employed as described in the previous section. The etch rates for W, Ti, Ta, Pt, Ni, and Co were approximately 25, 11.4, 10, 3.5, 2.5, and 2.3 nm/min, respectively. When the thickness of the remaining thin film is around 10 nm, the oxidized PDMS patterns are exposed to the reactive plasma and are rapidly etched away by forming volatile SF_x species. As a result, a nanoporous metallic film ~ 8 – 10 nm thick with the reverse image of the original block copolymer pattern was obtained. Figure 7-7d shows Pt, W, Ti, and Ta films with hexagonally arranged nanopores.

The histograms in Fig. 7-11 show the comparison between the dimensions of the original BCP pattern and the pores formed in the Ti film. The average pore size is 16.8 ± 1.4 nm, which is 6 % smaller than that of the BCP template. The formation of metal oxides, which are not chemically etchable with F ions, at the boundary between the deposited metal and oxidized PDMS template from the BCP may contribute to pore shrinkage.

The ferromagnetism of porous Co films with ~15 nm diameter pores is discussed here. Figure 7-8 shows the magnetic hysteresis loops of the antidot array compared to that of an unpatterned film of the same thickness made by CF_4-etching a film on a smooth substrate. The inset presents the morphology of Co antidots. The significant increase in coercivity of the antidot film (220 Oe) compared to that of the unpatterned film (8 Oe) is a result of pinning of domain walls by the pores[45-48], as observed in other magnetic antidot arrays made by ion-milling[46] or by deposition onto porous structures such as anodized alumina or block copolymer films.[47, 48] These observations are consistent with uniform pattern transfer over the sample area of several sq. mm.

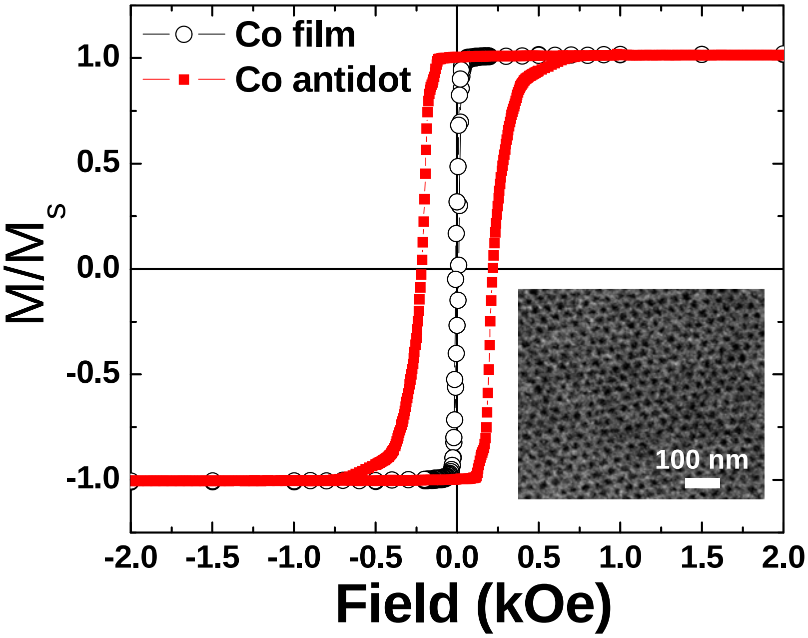

Fig. 7-8 The magnetic hysteresis loops of a Co antidot pattern.

The etch rate of SiO_2 is comparable with that of the oxidized PDMS, and thus the pattern-reversal technique cannot be used to make a porous silica film. Instead, nanoporous metallic films can be used as a robust etch mask to make holes in an underlying 20 nm thick SiO_2 film. A patterned Ni film with pore diameter 15.7 ± 1.8 nm (Figure 7-9a) was used as a mask to etch the SiO_2 film using a CF_4 plasma at a power of 180W, then the remaining Ni mask pattern was removed with a nickel wet etchant. Figure 7-9b shows the top and cross-sectional views of the porous SiO_2 pattern, in which the average hole size was 14.2 ± 2.1 nm (see the histogram in Fig. 7-11.). Materials such as porous silica can be useful as a low-k interlayer dielectric. This simple technique may be extended to the generation of well-controlled pores in other oxide materials such as TiO_2, which can be used for dye-sensitized solar cell devices.

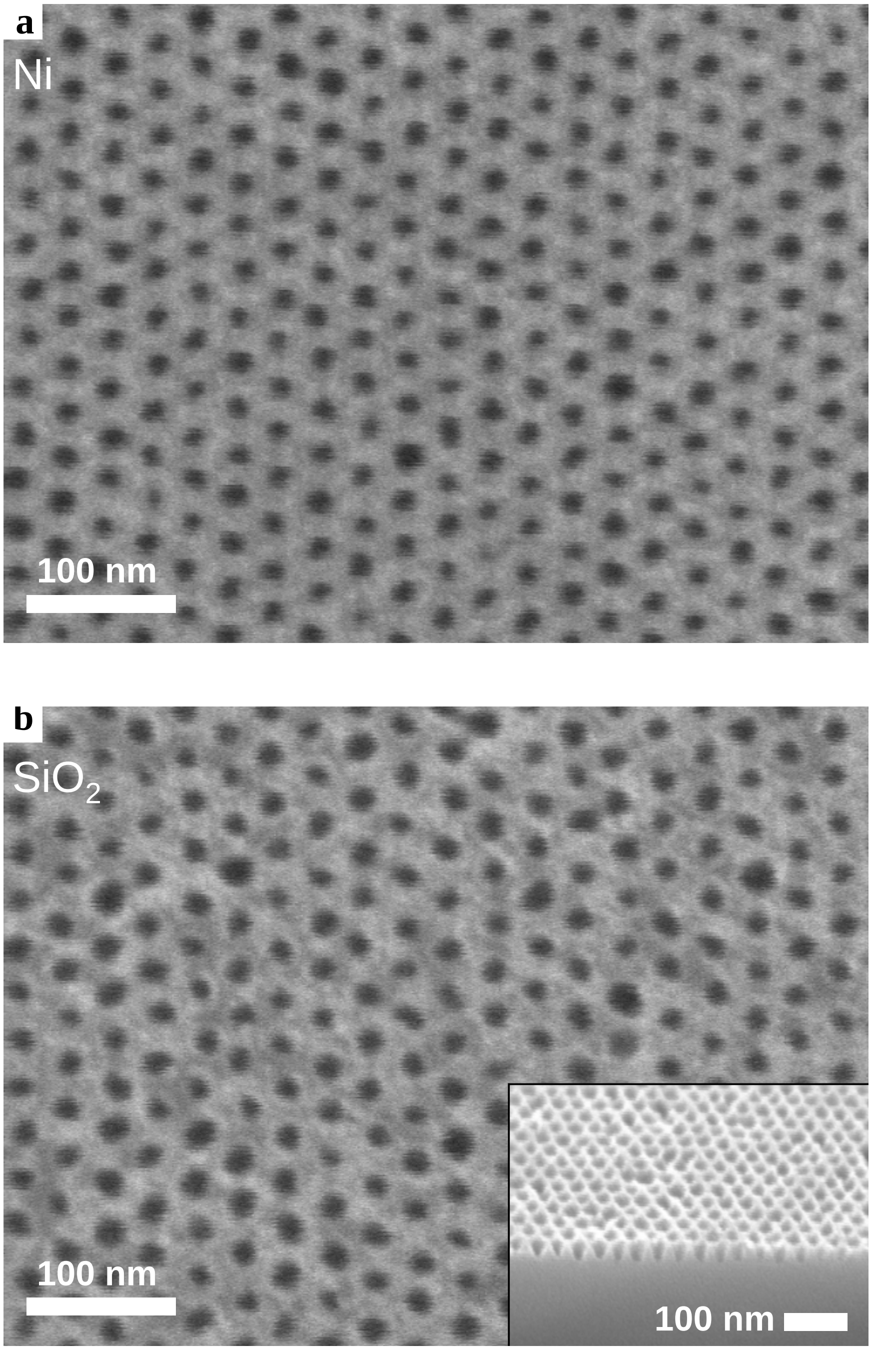

Fig. 7-9 SEM images of (a) a nanoporous Ni film on SiO2 and (b) patterned SiO2 via CF4 reactive ion etching and Ni wet-etching.

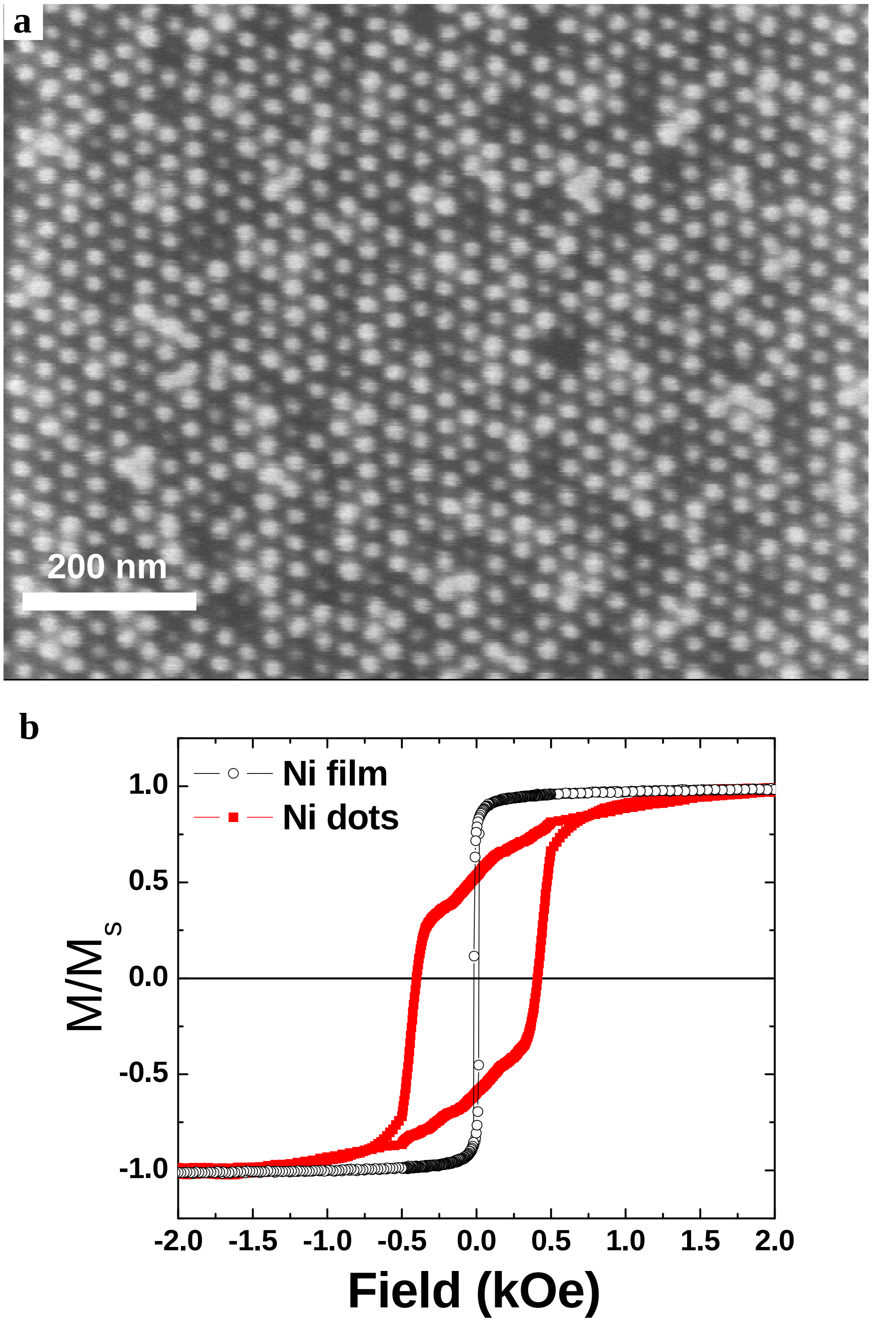

Fig. 7-10 (a) An SEM image and (b) the magnetic hysteresis loops of Ni dots

Finally, metallic Ni dot patterns were formed by a double pattern-reversal process. Nanoporous Ti films were first prepared as described in Fig. 7-6b-g. Ti was chosen since it has a higher etch rate than Ni. A 70 nm thick Ni film was then sputter-deposited onto the Ti, filling the pores, and a subsequent 450 W CF_4 plasma treatment was used to form the Ni dot array. As the Ni is eroded, the Ti antidot array is revealed, which is then rapidly removed due to its 4.5 times greater etch rate compared to Ni. Figure 7-10a demonstrates the Ni dots which have an average diameter of 17.3 ± 4.9 nm. The increase in size distribution compared to both the original BCP patterns and the pores in the Ti template may result from the inhomogeneity of the polycrystalline film microstructure. The magnetic hysteresis loop shown in Fig. 7-10b shows a coercivity of 417 Oe for the dot array, compared to 17 Oe for the continuous thin film, consistent with single domain reversal. This method may be used to generate nanoparticle arrays for patterned media.[49, 50]

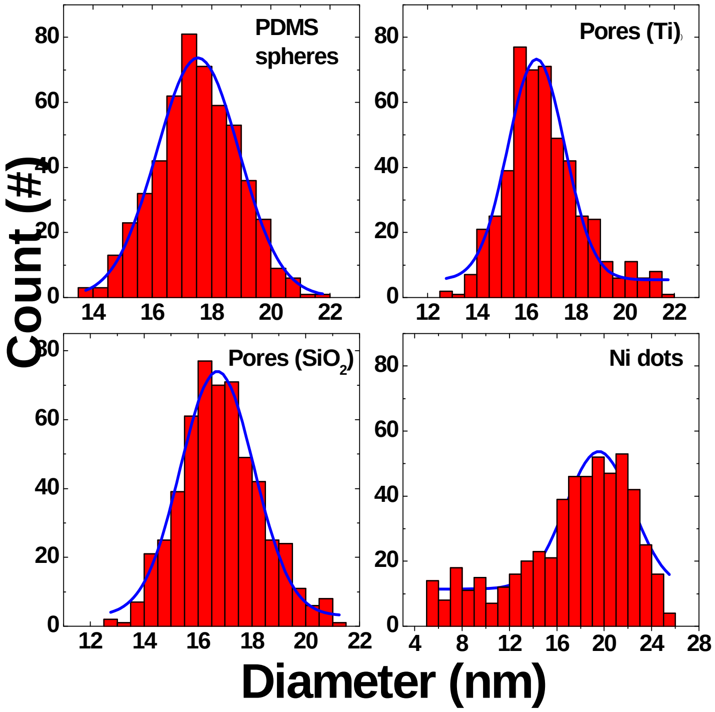

Fig. 7-11 Size histograms of PDMS dots, pores formed in Ti and SiO_2, and Ni dots.

7.5 Fabrication of magnetic ring patterns and characterization

This section demonstrates pattern transfer from concentric ring structures into a functional material, in this case a ferromagnetic thin film. Nanoscale ferromagnetic rings have attracted much interest due to their complex behavior and possible applications in magnetic memory, logic devices and bio-sensors,[28-32, 51] in addition to their use for studying domain behavior and current-induced domain wall motion.[52]

Fig. 7-12 illustrates the fabrication of concentric rings of cobalt using a pattern reversal process employing a CF_4 plasma. Interference lithography and etching were first employed to define a large-area array of 137 nm-wide and 30 nm-deep circular trenches, and the PS-PDMS block copolymer was self-assembled inside the trench patterns and etched to form patterns consisting of a PDMS ring and a central PDMS sphere. A 70 nm-thick Co thin film was deposited by radio-frequency sputtering over the block copolymer patterns, which partly planarized the surface. A 450W CF_4 plasma was used to sputter-etch the Co film slowly at a rate of 2.3 nm/min. However, as soon as the etch breaks through the Co film, the underlying oxidized PDMS patterns are rapidly removed by forming volatile SiF_x species. Stopping the etch at this point yielded a large array of pairs of concentric rings. The film thickness was 10 nm, the inner ring of each structure had an average outer diameter of 68 nm and a width of 16 nm, while the outer ring had an outer diameter of 133 nm and a width of 19.5 nm. The spacing between the rings was 13 nm, which is slightly smaller than the original 16 nm linewidth of the PDMS patterns.

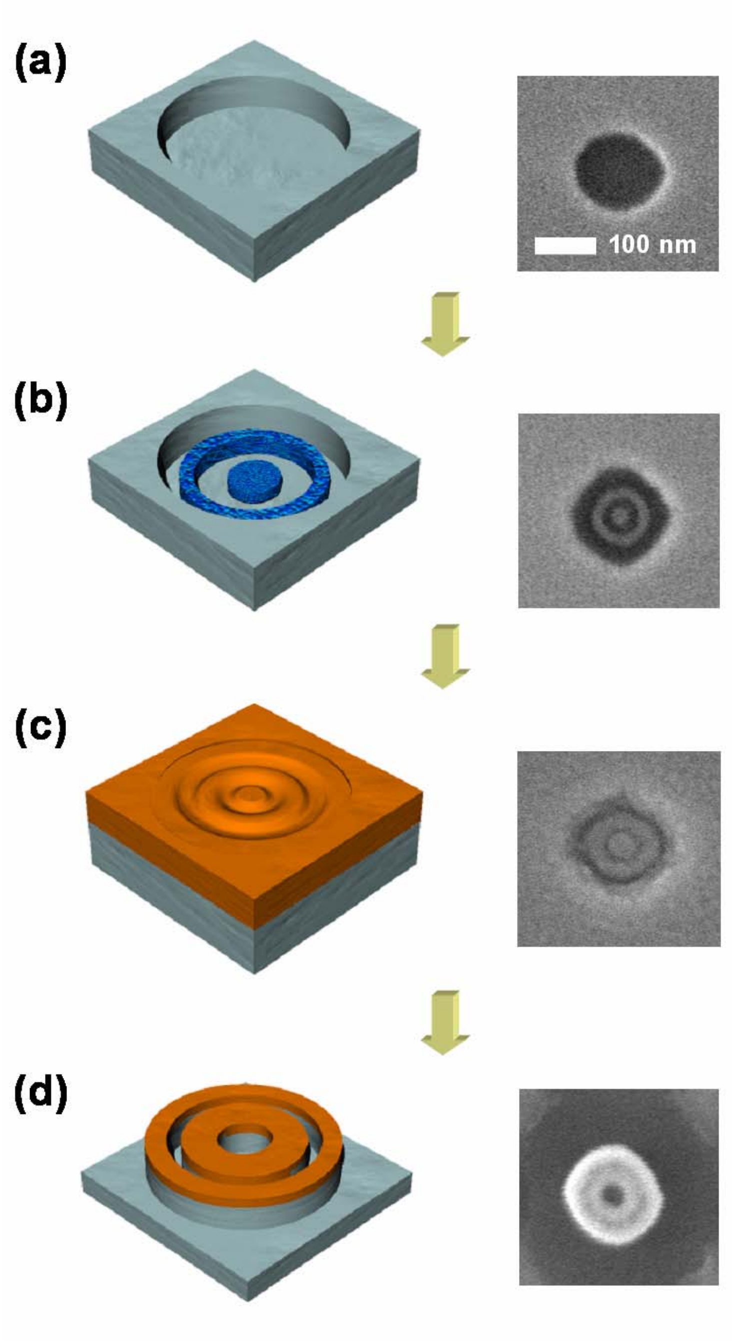

Fig. 7-12 Cobalt double ring fabrication process (a) Fabrication of circular trench templates using interference lithography. (b) Self-assembly of ring patterns in the trenches and reactive ion etching to generate oxidized PDMS ring arrays. (c Sputter deposition of a Co thin film (thickness = 70nm). (d) Dry etching with 450W CF4 plasma. Initially the Co film is sputter-etched slowly by incident CF_x^+ ions, then the exposed oxidized PDMS patterns are rapidly removed through a chemical etching process. Consequently, the Co ring features form a reverse image of the original PDMS patterns.

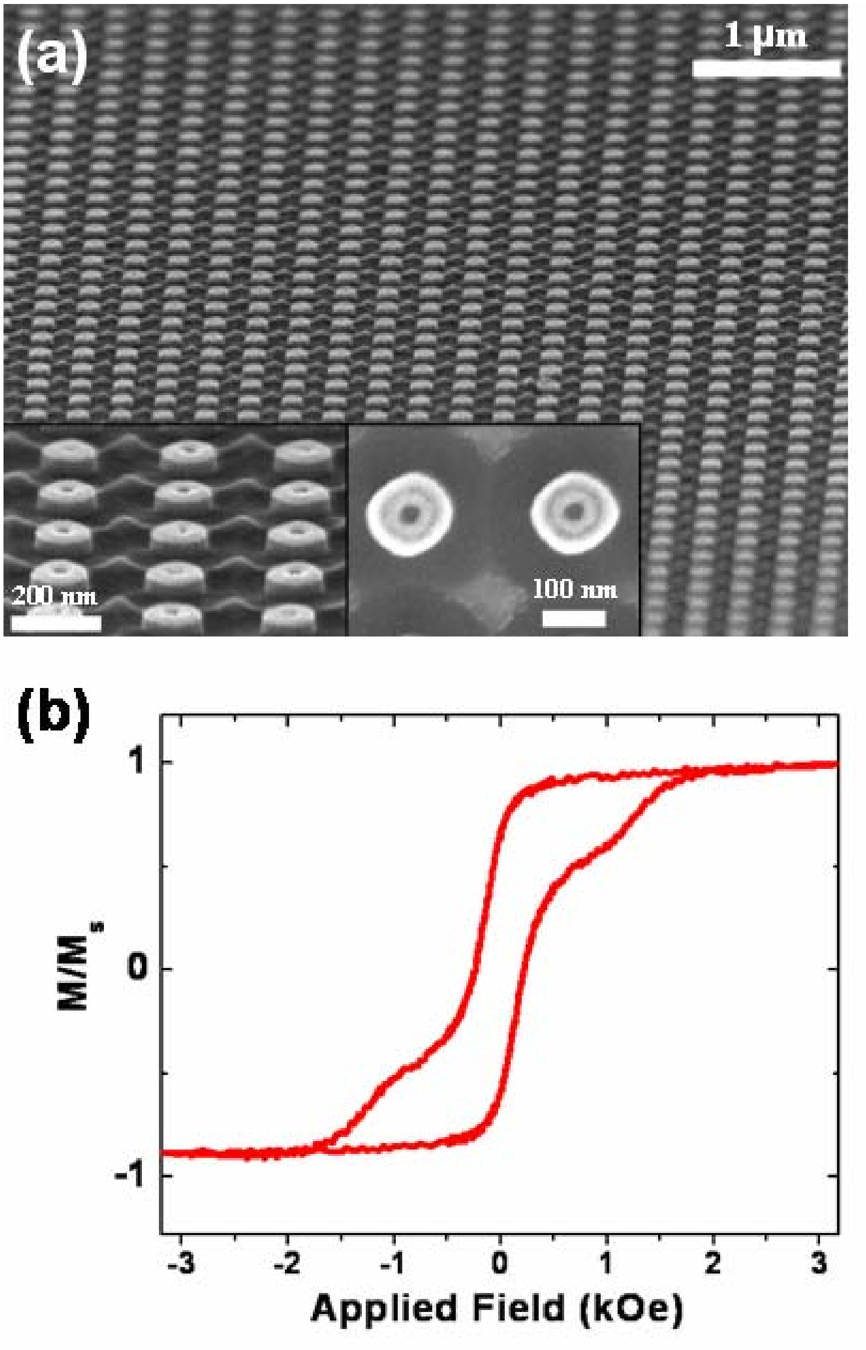

Fig. 7-13 Pattern transfer into a ferromagnetic film. (a) SEM image of an array of Co double rings. (b) measured and (c) simulated normalized magnetic hysteresis loops (M/Ms) of the double rings. The two rings in each structure are magnetostatically coupled, and the slanted plateau results from the formation of a distorted 'vortex' state.

Fig. 7-13 illustrates the Co double concentric ring array. Magnetic hysteresis loops of the ring array and a half-loop derived from micromagnetic simulation are shown in Figs. 7-13b and 7-14, respectively. The experimental hysteresis loop is characterized by two-step switching with a slanted plateau between approximately 500 and 850 Oe. This switching behavior is reproduced qualitatively by the simulation, which shows that the two rings switch together as a result of magnetostatic interactions. As the field is reduced, the first step corresponds to a correlated onion-to-vortex transition of the rings. The nonzero moment of the correlated vortex state occurs because the vortex is off-center so that the majority of the ring material is magnetized in the direction of the reverse field. At higher reverse fields, the rings switch, again collectively, into a reverse onion state.

In order to determine the effects of magnetic coupling between the inner and outer rings, three different geometries, i.e. a double ring and two separate single rings having the same size as the outer and inner ring, were investigated. Although the single rings have different reversal fields, the double ring shows a correlated reversal due to strong magnetostatic coupling between the inner and outer ring. Thus, the hysteresis loop of the double ring is not a superposition of that of its two component rings. The outer ring has lower reversal fields than the inner ring, with the onion-to-vortex transition occuring around remanence. The onion-to-vortex switching field of the double ring falls in between the switching fields of the individual rings, while the vortex-to-reverse onion switching field of the double ring is very similar to that of the outer ring. The vortex-to-reverse onion switching takes place by the nucleation of a reverse domain, and this occurs first in the outer ring. During the onion-to-vortex switching the domain walls move in the same direction, which results in the same chirality in both rings. The vortex states of the rings are asymmetrical and have a non-zero remanence, unlike those seen in simulations of larger diameter rings.

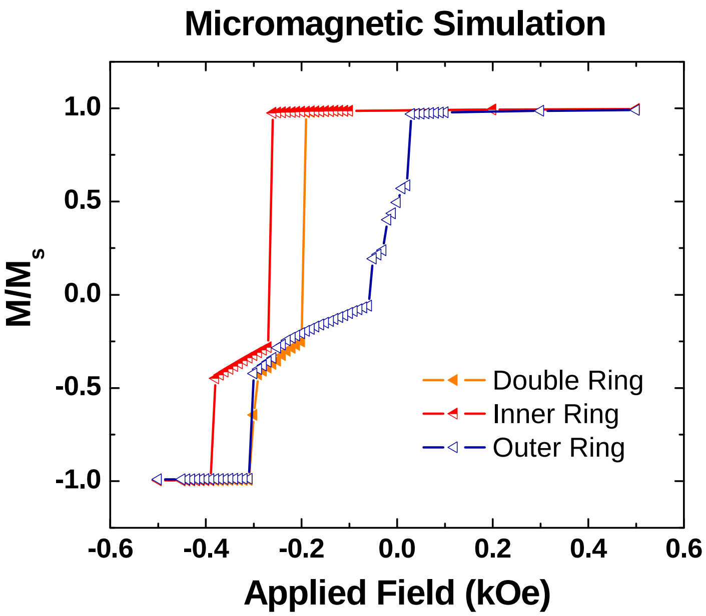

Double Ring

Inner Ring (Separate simulation)

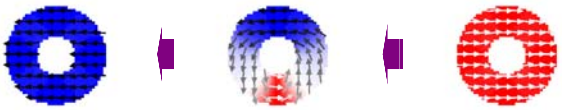

Outer Ring (Separate Simulation)

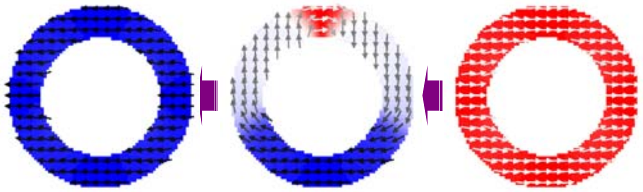

Fig. 7-14 Micromagnetic simulation results for double ring and two separate single rings with different sizes. The rings in the right, middle, and left correspond to three different magnetization states achieved by varying the magnetic field from +0.5 kOe to -0.5 kOe. Asymmetric vortex states (illustrated by the rings in the middle) are formed as intermediate states between the onion and reverse onion states.

The magnetic coupling strength between the individual rings in the multiple concentric ring configurations can be tailored by modifying the dimensions or materials of the rings, and this can control the switching field and number of stable remanent states of the structure.

This demonstration illustrates pattern transfer into a functional material from self-assembled 16 nm linewidth features in a large area, cost-effective and scalable manner. Since the pattern transfer technique may be applied to other materials, the resulting well-defined circular features may be also useful in a wide range of high-performance and highly integrated devices that incorporate nanoscale rings, including transistors,[33] memories,[30-32] sensors,[28, 29] quantum devices[36], [37, 38] and lasers.[35] Scaling-down of those ring devices using templated block copolymer self-assembly to generate nanoscale ring patterns may provide a path towards higher information storage density, a faster switching time, or a lower power consumption.

7.6 Summary

This chapter suggested a universal method to transfer the self-assembled structures into metallic films using a simple pattern reversal technique. This method is versatile and has been used to form well-ordered lines, pores, and rings in a variety of metals including Ti, Pt, W, Ta, Co, and Ni. This technique may be compatible with various film deposition methods e.g. chemical vapor deposition, sputtering, evaporative deposition, pulsed-laser deposition, or spin-casting. Generated self-assembly structures are, in general, non-functional, and thus this pattern-transfer technique is crucial for applications such as memories, sensors, or quantum devices.

References

[1] Y. Cui, C. M. Lieber, "Functional nanoscale electronic devices assembled using silicon nanowire building blocks", *Science 291*, p. 851 (2001)

[2] X. F. Duan, Y. Huang, Y. Cui, J. F. Wang, C. M. Lieber, "Indium phosphide nanowires as building blocks for nanoscale electronic and optoelectronic devices", *Nature 409*, p. 66 (2001)

[3] M. H. Huang, S. Mao, H. Feick, H. Q. Yan, Y. Y. Wu, H. Kind, E. Weber, R. Russo, P. D. Yang, "Room-temperature ultraviolet nanowire nanolasers", *Science 292*, p. 1897 (2001)

[4] Y. C. Kong, D. P. Yu, B. Zhang, W. Fang, S. Q. Feng, "Ultraviolet-emitting ZnO nanowires synthesized by a physical vapor deposition approach", *Applied Physics Letters 78*, p. 407 (2001)

[5] F. Patolsky, G. F. Zheng, C. M. Lieber, "Nanowire-based biosensors", *Analytical Chemistry 78*, p. 4260 (2006)

[6] J. K. W. Yang, K. K. Berggren, "Using high-contrast salty development of hydrogen silsesquioxane for sub-10-nm half-pitch lithography", *Journal of Vacuum Science & Technology B 25*, p. 2025 (2007)

[7] C. Harrison, P. M. Chaikin, D. A. Huse, R. A. Register, D. H. Adamson, A. Daniel, E. Huang, P. Mansky, T. P. Russell, C. J. Hawker, D. A. Egolf, I. V. Melnikov, E. Bodenschatz, "Reducing substrate pinning of block copolymer microdomains with a buffer layer of polymer brushes", *Macromolecules 33*, p. 857 (2000)

[8] M. S. Gudiksen, L. J. Lauhon, J. Wang, D. C. Smith, C. M. Lieber, "Growth of nanowire superlattice structures for nanoscale photonics and electronics", *Nature 415*, p. 617 (2002)

[9] J. Hahm, C. M. Lieber, "Direct ultrasensitive electrical detection of DNA and DNA sequence variations using nanowire nanosensors", *Nano Letters 4*, p. 51 (2004)

[10] P. A. Smith, C. D. Nordquist, T. N. Jackson, T. S. Mayer, B. R. Martin, J. Mbindyo, T. E. Mallouk, "Electric-field assisted assembly and alignment of metallic nanowires", *Applied Physics Letters 77*, p. 1399 (2000)

[11] W. R. Small, V. N. Paunov, "Fabrication of electrically anisotropic agarose gels by dielectrophoretic assembly and encapsulation of silver nanowires", *Journal of Materials Chemistry 18*, p. 2082 (2008)

[12] J. Y. Cheng, C. A. Ross, V. Z. H. Chan, E. L. Thomas, R. G. H. Lammertink, G. J. Vancso, "Formation of a cobalt magnetic dot array via block copolymer lithography", *Advanced Materials 13*, p. 1174 (2001)

[13] J. Y. Cheng, W. Jung, C. A. Ross, "Magnetic nanostructures from block copolymer lithography: Hysteresis, thermal stability, and magnetoresistance", *Physical Review B 70*, p. 064417 (2004)

[14] D. G. Choi, J. R. Jeong, K. Y. Kwon, H. T. Jung, S. C. Shin, S. M. Yang, "Magnetic nanodot arrays patterned by selective ion etching using block copolymer templates", *Nanotechnology 15*, p. 970 (2004)

[15] F. Ilievski, C. A. Ross, G. J. Vancso, "Magnetic reversal phenomena of perpendicular magnetic islands fabricated by block copolymer lithography", *Journal of Applied Physics 103*, p. 07C520 (2008)

[16] D. J. Milliron, S. Raoux, R. Shelby, J. Jordan-Sweet, "Solution-phase deposition and nanopatterning of GeSbSe phase-change materials", *Nature Materials 6*, p. 352 (2007)

[17] C. T. Black, "Self-aligned self assembly of multi-nanowire silicon field effect transistors", *Applied Physics Letters 87*, p. 163116 (2005)

[18] Y. S. Jung, C. A. Ross, "Orientation-controlled self-assembled nanolithography using a polystyrene-polydimethylsiloxane block copolymer", *Nano Letters 7*, p. 2046 (2007)

[19] N. K. Raman, M. T. Anderson, C. J. Brinker, "Template-based approaches to the preparation of amorphous, nanoporous silicas", *Chemistry of Materials 8*, p. 1682 (1996)

[20] D. Sundrani, S. B. Darling, S. J. Sibener, "Hierarchical assembly and compliance of aligned nanoscale polymer cylinders in confinement", *Langmuir 20*, p. 5091 (2004)

[21] K. P. S. Dancil, D. P. Greiner, M. J. Sailor, "A porous silicon optical biosensor: Detection of reversible binding of IgG to a protein A-modified surface", *Journal of the American Chemical Society 121*, p. 7925 (1999)

[22] J. Y. Ying, C. P. Mehnert, M. S. Wong, "Synthesis and applications of supramolecular-templated mesoporous materials", *Angewandte Chemie-International Edition 38*, p. 56 (1999)

[23] K. Hara, T. Horiguchi, T. Kinoshita, K. Sayama, H. Sugihara, H. Arakawa, "Highly efficient photon-to-electron conversion with mercurochrome-sensitized nanoporous oxide semiconductor solar cells", *Solar Energy Materials and Solar Cells 64*, p. 115 (2000)

[24] J. S. Seo, D. Whang, H. Lee, S. I. Jun, J. Oh, Y. J. Jeon, K. Kim, "A homochiral metal-organic porous material for enantioselective separation and catalysis", *Nature 404*, p. 982 (2000)

[25] P. Jiang, J. F. Bertone, V. L. Colvin, "A lost-wax approach to monodisperse colloids and their crystals", *Science 291*, p. 453 (2001)

[26] Z. S. Wang, C. H. Huang, Y. Y. Huang, Y. J. Hou, P. H. Xie, B. W. Zhang, H. M. Cheng, "A highly efficient solar cell made from a dye-modified ZnO-covered TiO_2 nanoporous electrode", *Chemistry of Materials 13*, p. 678 (2001)

[27] S. Niwa, M. Eswaramoorthy, J. Nair, A. Raj, N. Itoh, H. Shoji, T. Namba, F. Mizukami, "A one-step conversion of benzene to phenol with a palladium membrane", *Science 295*, p. 105 (2002)

[28] M. M. Miller, G. A. Prinz, S. F. Cheng, S. Bounnak, "Detection of a micron-sized magnetic sphere using a ring-shaped anisotropic magnetoresistance-based sensor: A model for a magnetoresistance-based biosensor", *Applied Physics Letters 81*, p. 2211 (2002)

[29] J. Llandro, T. J. Hayward, D. Morecroft, J. A. C. Bland, F. J. Castano, I. A. Colin, C. A. Ross, "Quantitative digital detection of magnetic beads using pseudo-spin-valve rings for multiplexed bioassays", *Applied Physics Letters 91*, p. 203904 (2007)

[30] J. G. Zhu, Y. F. Zheng, G. A. Prinz, "Ultrahigh density vertical magnetoresistive random access memory (invited)", *Journal of Applied Physics 87*, p. 6668 (2000)

[31] F. J. Castano, D. Morecroft, W. Jung, C. A. Ross, "Spin-dependent scattering in multilayered magnetic rings", *Physical Review Letters 95*, p. 137201 (2005)

[32] Z. C. Wen, H. X. Wei, X. F. Han, "Patterned nanoring magnetic tunnel junctions", *Applied Physics Letters 91*, p. 122511 (2007)

[33] H. Watanabe, C. Manabe, T. Shigematsu, M. Shimizu, "Dual-probe scanning tunneling microscope: Measuring a carbon nanotube ring transistor", *Applied Physics Letters 78*, p. 2928 (2001)

[34] M. T. Hill, H. J. S. Dorren, T. de Vries, X. J. M. Leijtens, J. H. den Besten, B. Smalbrugge, Y. S. Oei, H. Binsma, G. D. Khoe, M. K. Smit, "A fast low-power optical memory based on coupled micro-ring lasers", *Nature 432*, p. 206 (2004)

[35] P. J. Pauzauskie, D. J. Sirbuly, P. D. Yang, "Semiconductor nanowire ring resonator laser", *Physical Review Letters 96*, p. 4 (2006)

[36] Y. Aharonov, "Significance of Electromagnetic Potentials in the Quantum Theory", *Physical Review 115*, p. 485 (1959)

[37] L. P. Levy, G. Dolan, J. Dunsmuir, H. Bouchiat, "Magnetization of Mesoscopic Copper Rings - Evidence for Persistent Currents", *Physical Review Letters 64*, p. 2074 (1990)

[38] K. A. Matveev, A. I. Larkin, L. I. Glazman, "Persistent current in superconducting nanorings", *Physical Review Letters 89*, p. 096802 (2002)

[39] A. Fuhrer, S. Luescher, T. Ihn, T. Heinzel, K. Ensslin, W. Wegscheider, M. Bichler, "Energy spectra of quantum rings", *Nature 413*, p. 822 (2001)

[40] R. J. Warburton, C. Schaflein, D. Haft, F. Bickel, A. Lorke, K. Karrai, J. M. Garcia, W. Schoenfeld, P. M. Petroff, "Optical emission from a charge-tunable quantum ring", *Nature 405*, p. 926 (2000)

[41] Y. S. Jung, W. Jung, C. A. Ross, "Nanofabricated Concentric Ring Structures by Templated Self-Assembly of a Diblock Copolymer", *Nano Lett. 8*, p. 2975 (2008)

[42] M. Hayashi, L. Thomas, R. Moriya, C. Rettner, S. S. P. Parkin, "Current-controlled magnetic domain-wall nanowire shift register", *Science 320*, p. 209 (2008)

[43] S. S. P. Parkin, M. Hayashi, L. Thomas, "Magnetic domain-wall racetrack memory", *Science 320*, p. 190 (2008)

[44] D. R. Lide, ed., *CRC Handbook of Chemistry and Physics, 88th Edition(Internet Version 2008)*, CRC Press/Taylor and Francis, Boca Raton, FL, 2008.

[45] J. A. Barnard, A. Butera, H. Fujiwara, V. R. Inturi, J. D. Jarratt, T. J. Klemmer, T. W. Scharr, J. L. Weston, "High coercivity nanostructured networks", *Journal of Applied Physics 81*, p. 5467 (1997)

[46] T. Kubo, J. S. Parker, M. A. Hillmyer, C. Leighton, "Characterization of pattern transfer in the fabrication of magnetic nanostructure arrays by block copolymer lithography", *Applied Physics Letters 90*, p. 233113 (2007)

[47] V. P. Chuang, W. Jung, C. A. Ross, J. Y. Cheng, P. Oun-Ho, K. Ho-Cheol, "Multilayer magnetic antidot arrays from block copolymer templates", *Journal of Applied Physics 103*, p. 074307 (2008)

[48] N. P. Nguyen, S. L. Lim, F. Xu, Y. G. Ma, C. K. Ong, "Enhancement of exchange bias and ferromagnetic resonance frequency by using multilayer antidot arrays", *Journal of Applied Physics 104*, p. 093708 (2008)

[49] C. Ross, "Patterned magnetic recording media", *Annual Review of Materials Research 31*, p. 203 (2001)

[50] C. A. Ross, J. Y. Cheng, "Patterned magnetic media made by self-assembled block-copolymer lithography", *Mrs Bulletin 33*, p. 838 (2008)

[51] F. J. Castano, B. G. Ng, A. Colin, D. Morecroft, W. Jung, C. A. Ross, "Magnetoresistance of submicrometre multilayer Wheatstone bridges as a probe of magnetic reversal mechanism", *Journal of Physics D: Applied Physics 41*, p. 132005 (2008)

[52] M. Klaui, C. A. F. Vaz, J. A. C. Bland, W. Wernsdorfer, G. Faini, E. Cambril, L. J. Heyderman, "Domain wall motion induced by spin polarized currents in ferromagnetic ring structures", *Applied Physics Letters 83*, p. 105 (2003)

Chapter 8

Conclusions and future work

8.1 Conclusions

This thesis investigated PS-PDMS block copolymers for applications in self-assembled nanolithography. These block copolymers combine the advantages of a high interaction parameter, leading to well-ordered structures, with low edge roughness, and a high etch selectivity between the two blocks, providing highly etch-resistant masks for pattern transfer. Topographical PDMS-grafted patterns were used to template block copolymer microdomain arrays with long range order. A brush treatment was critical because it can facilitate the kinetics of self-assembly through surface diffusion. Micron-scale linear templates fabricated with optical interference lithography and nano-scale post arrays patterned with electron beam lithography were used to provide perfect ordering of cylinder and sphere morphologies. In equilibrium, the long axis of cylinders and the close-packed direction of spheres are parallel to the linear wall, providing long-range ordering. It was also found that commensurability between the post-spacing and the natural period of spheres greatly influences the pattern registration and the orientational relationship between the two lattice systems.

Extensive tunability of the self-assembly patterns was demonstrated in two ways. First, control of two solvent-annealing parameters, the solvent mixing ratio and the vapor pressure, affects the period and linewidth of parallel cylinder arrays, and can even lead to different morphologies, such as a perforated lamellar structure. The demonstration of independent control over the period and linewidth is useful for BCP-based fabrication of device structures. Second, spatial confinement of block copolymers can change the pattern geometry. For example, concentric ring patterns can be obtained from a cylinder-forming diblock copolymer under circular confinement. The number of rings and the existence of a central dot can be controlled by the confinement diameter.

A simple de Gennes-type free energy model composed of the strain energy of polymer chains and the interfacial energy between two microdomains was used to explain the change of pattern period by confinement or vapor treatment and to predict the orientational relationship between the arrays of hexagonally-packed posts and block copolymer spheres

The patterns generated can be transferred to functional materials such as metals or conducting polymers, the functional nanostructures can be used as device elements. Conducting polymer nanowires were obtained through a series of reactive ion etching steps using the self-assembled line patterns as an etch mask. The nanowires showed a higher and more linear resistance response than an unpatterned film with the same thickness, which is attributed to its high surface area to volume ratio and to its short diffusion length. Very well-ordered lines, pores, and rings in a variety of metals including Ti, Pt, W, Ta, Co, and Ni were fabricated through a pattern reversal process. Coercivity enhancements were observed for the fabricated ferromagnetic nanostructures such as wires, rings, dots, and antidots. These functional nanostructures can be utilized for a variety of devices such as high-density and high performance sensors, information-storage devices, nanochannels, interconnects, and so on.

8.2 Future work

The developed self-assembly patterns can be used for the fabrication of other devices. A few examples are suggested in this section. Additionally, remaining issues in BCP nanolithography that needed to be resolved for being used as a manufacturing process are discussed.

8.2.1 Cross-point memory devices

Cross-point (or crossbar) memory usually refers to two terminal devices where storage materials are sandwiched between two sets of electrode arrays that are perpendicular to each other. Every bit-cell is defined at the junction of two electrodes which can be independently addressed. The geometry is tolerant of the formation of defective elements, whose density rapidly increases as the feature size shrinks, since the architecture can be reconfigured to avoid the failure from the defects unavoidably generated during fabrication. [1] Moreover, the simple structure may contribute for potentially inexpensive manufacturing by reducing the number of steps. A nonvolatile memory device should have at least two different metastable states which can be switched by an application of an electric field.[2] Many organic electronic devices have demonstrated switching behaviors, and two-terminal resistive random access memory can be made based on the electrical switching of such devices. Organic electronic devices have potential advantages such as low manufacturing cost, low temperature process, and good mechanical flexibility.

Programmable electrical bistability of a polymer film containing a conjugated organic compound and metal nanoparticles capped with an alkanethiol can be used for making a high-density crosspoint memory device by inserting the polymer composite between two metal electrodes.[3, 4] Au nanoparticles (Au-NP) surrounded by dodecanethiol, and 8-hydroxyquinonine (8-HQ) can be considered. Polystyrene has a role as an inert matrix and can be replaced by other non-conducting polymers such as PMMA.[3, 4] Memory structures with a capacity of over 70 giga bits per cm^2 can be achieved.

8.2.2 Nanochannel structures

Nanochannels can be defined as small scale channel structures with at least one dimension in the nanometer range.[5] The nanometer scale of the channels may facilitate the discovery of new phenomena since the channel size is close to the order of the dimension of the molecules comprising the fluid. Hence, fundamental investigations on phenomena such as fluid transport and molecular behavior at extraordinarily small dimensions can be possible. Nanochannels can also be applied to lab-on-a-chip (LOC), which is desirable for small-scale biological analysis with a high throughput. The small dimensions of the LOC can markedly shorten processing times and the amount of reagents, which may contribute to a significant cost reduction.

Commercialization of the device may require cost-effective fabrication techniques which can precisely control nanoscale features made on large scale substrates. Block copolymer lithography satisfies those requirements. Usually, nanochannels need to be transparent for optical measurements such as florescence microscopy. Transparent substrates such as glass would be needed for a complete transparency. Although this thesis does not include the fabrication results, well-defined nanochannels were obtained by a simple film deposition on a polymer nanopatterns generated by the self-assembly and pattern-transfer. SiO_2 deposition may be a desirable due to its high optical transparency.

8.2.3 Metal oxide nanowire sensors

ZnO is a II-VI direct bandgap (E_g=3.3 eV) semiconductor with numerous applications ranging from optoelectronics to chemical sensors because of its distinctive optical, electronic and chemical properties.[6-10] There have been many reports about gas sensor applications based on various nanostructures of ZnO such as nanowires, nanorods, nanobelts and nanotetrapods.[8-11] These devices usually require chemical synthesis steps and post-assembly of nanostructured materials.[12, 13] One type of these devices is based on a configured single nanowire on Pt electrodes patterned by e-beam lithography. Although excellent sensitivity has been reported, the disadvantages of this method are that it is difficult to control the number of nanowires connecting the gaps between electrodes and that individual nanowires usually have large distributions in their electrical properties, diameter and length, which may lower device-to-device reproducibility.

The utilization of block copolymer lithography is promising as a way of fabricating highly ordered ZnO nanowire patterns. Block copolymer self-assembly is a parallel process that can make around 0.3 million linear patterns on a 1cm^2 substrate. The advantage is that the carrier path in the nanopatterns can be well-defined without using expensive facilities, and the collective and averaged signals from numerous nanopatterns would be conducive to a better reproducibility.

8.2.4 Patterned magnetic media

The areal density of state-of-the-art magnetic media disk drives approaches to one terabit per square inch, which have relied on the developments in GMR heads and thin-film perpendicular media. However, alternative methods should be developed in order to keep increasing the storage density further, which is expected to be limited by the superparamagnetic effect in thin film media.[14] If a grain size becomes too small, thermal energy can overcome the magnetic energy and spontaneously flip the magnetization. One promising approach is to use exchange-coupled nanostructures called patterned media. If a bit is stored in a small island, the storage density can increase up to 10 terabits per square inch until superparamagnetic effects eventually prevent a further increase. BCP techniques can potentially be used for the fabrication of uniform and perfectly ordered magnetic islands. The feasibility of this concept was demonstrated by previous works.[7, 15] However, remaining issues include reductions in pitch, feature size variation, and edge roughness below around 20 nm, 2 nm, and 2nm, respectively. The solutions may require a new design of BCPs, which can simultaneously provide size reduction as well as a very tight distribution in microdomain sizes, and new annealing methods for increasing the throughput of the process. Pattern-transferring into magnetic materials is another issue due to the chemical and mechanical durability of transition metals.

8.2.5 Remaining challenges in block copolymer pattern formation

Ability of sub-10-nm pattern generation is quite important for the continued increase in information storage density. In the strong-segregation limit, the natural domain spacing (L_0 = pitch) of BCPs scales with $N^{2/3}\chi^{1/6}$, and thus N (degree of polymerization) should be small enough for decreasing L_0 further. However, from calculations based on the mean-field theory, it turns out that χN should be larger than 10.5 for inducing the phase separation of two different polymer blocks.[16] Consequently, BCPs with a larger χ are thermodynamically more advantageous for reducing L_0 and for obtaining well-defined structures. For PS-PMMA, which has a small χ, the minimum feature size was found to be around 14 nm half-pitch for lamellar microdomains. However, recent results from this thesis research showed that

PS-PDMS with a relatively large χ can generate perfectly ordered 8 nm-wide lines made from a cylindrical BCP. The pattern size can be further reduced by using a lamellar BCP and decreasing the molecular weight. Simple calculations suggest that the minimum microdomain spacing (L_0 = pitch) would be around 5.5 nm assuming a lamellar morphology. However, the minimum dimension that can be experimentally achievable may be larger than the calculated value due to a diffuse interface resulting from an entropic effect for short-chain polymers. The diffuse interface, which is related to line edge roughness, can occupy a more substantial fraction of the total domain width as the decrease of chain length. BCPs with a larger χ are again helpful to reduce the interfacial width and line edge roughness. The use of a lamellar morphology requires a perpendicular alignment through neutralizations of surface and interfaces using appropriate brush and solvent treatments. Instability of BCP thin films with a very small thickness could be another potential difficulty.

Having more freedom in pattern geometries is also important since traditionally there have been almost no restrictions in device layout. Thus, the highly regular nature of BCP patterns is not very suitable for a current chip design. There could be two different solutions. One is to redesign chip layouts to have much higher regularity. With the introduction of resolution enhancement technologies recently, which restrict the choices in pitch and geometry, there have been attempts to optimize layouts for regular lithography.[17] An extremely simplified chip design may be a cross-point architecture composed of only crossed lines. Another approach is to develop BCP techniques that can generate arbitrarily shaped patterns. T, Y junctions and jog patterns were already demonstrated using a BCP assembly on electron-beam patterned brushes, although the 1:1 pattern registration seriously limits practicability. Overall, a compromise between the two solutions as the most practical way is expected. However, an ultimate vision of the researchers in this field would be a fully self assembled circuit (Fig. 8-1) fabricated with aperiodic BCP patterns and the sparsest template.

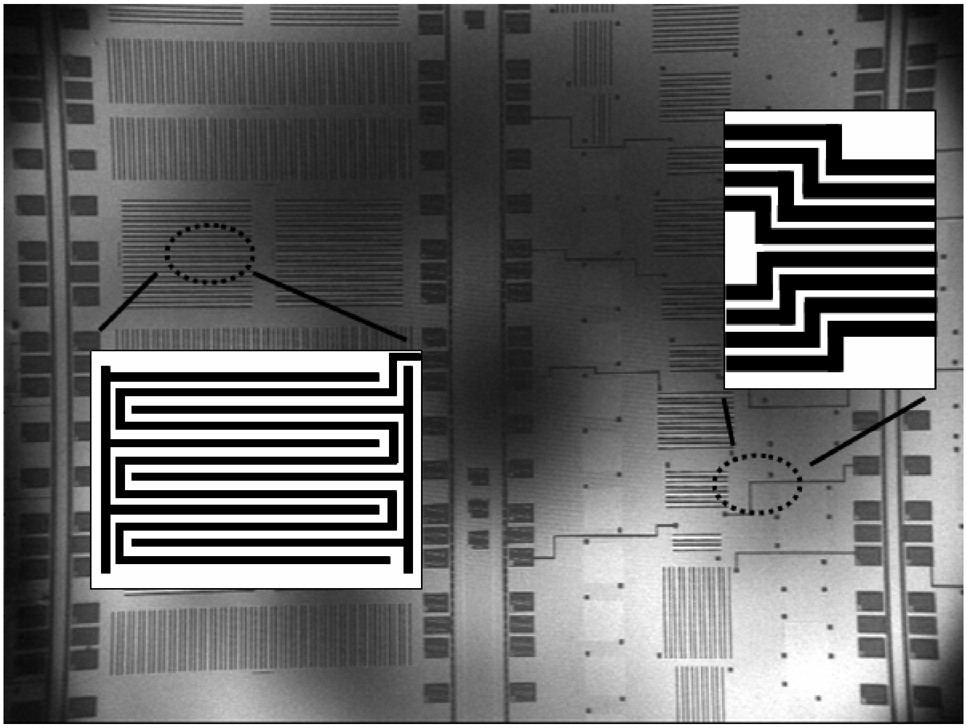

Fig. 8-1 An imaginary circuit layout composed of self-assembled BCP patterns

More processing issues that have not been known can be identified during the process developments of the nanoscale devices listed above. Moreover, for better practicability of BCP nanolithography, the techniques developed by academic investigators should be verified and standardized by engineers in industries.

References

[1] C. A. Ross, Y. S. Jung, V. P. Chuang, F. Ilievski, J. K. W. Yang, I. Bita, E. L. Thomas, H. I. Smith, K. K. Berggren, G. J. Vancso, J. Y. Cheng, "Si-containing block copolymers for self-assembled nanolithography", *Journal of Vacuum Science & Technology B 26*, p. 2489 (2008)

[2] J. C. Scott, L. D. Bozano, "Nonvolatile memory elements based on organic materials", *Advanced Materials 19*, p. 1452 (2007)

[3] J. Y. Ouyang, C. W. Chu, C. R. Szmanda, L. P. Ma, Y. Yang, "Programmable polymer thin film and non-volatile memory device", *Nature Materials 3*, p. 918 (2004)

[4] J. Y. Ouyang, C. W. Chu, R. J. H. Tseng, A. Prakash, Y. Yang, "Organic memory device fabricated through solution processing", *Proceedings of the Ieee 93*, p. 1287 (2005)

[5] D. Mijatovic, J. C. T. Eijkel, A. van den Berg, "Technologies for nanofluidic systems: top-down vs. bottom-up - a review", *Lab on a Chip 5*, p. 492 (2005)

[6] S. Hayamizu, H. Tabata, H. Tanaka, T. Kawai, "Preparation of crystallized zinc oxide films on amorphous glass substrates by pulsed laser deposition", *Journal of Applied Physics 80*, p. 787 (1996)

[7] J. Y. Cheng, W. Jung, C. A. Ross, "Magnetic nanostructures from block copolymer lithography: Hysteresis, thermal stability, and magnetoresistance", *Physical Review B 70*, p. 064417 (2004)

[8] X. H. Kong, X. M. Sun, X. L. Li, Y. D. Li, "Catalytic growth of ZnO nanotubes", *Materials Chemistry and Physics 82*, p. 997 (2003)

[9] Y. B. Li, Y. Bando, T. Sato, K. Kurashima, "ZnO nanobelts grown on Si substrate", *Applied Physics Letters 81*, p. 144 (2002)

[10] E. Verploegen, T. Zhang, Y. S. Jung, C. Ross, P. T. Hammond, "Controlling the Morphology of Side Chain Liquid Crystalline Block Copolymer Thin Films through Variations in Liquid Crystalline Content", *Nano Letters 8*, p. 3434 (2008)

[11] H. W. Suh, G. Y. Kim, Y. S. Jung, W. K. Choi, D. Byun, "Growth and properties of ZnO nanoblade and nanoflower prepared by ultrasonic pyrolysis", *Journal of Applied Physics 97*, p. 044305 (2005)

[12] F. Hernandez-Ramirez, A. Tarancon, O. Casals, J. Arbiol, A. Romano-Rodriguez, J. R. Morante, "High response and stability in CO and humidity measures using a single SnO_2 nanowire", *Sensors and Actuators B-Chemical 121*, p. 3 (2007)

[13] M. Law, H. Kind, B. Messer, F. Kim, P. D. Yang, "Photochemical sensing of NO2 with SnO_2 nanoribbon nanosensors at room temperature", *Angewandte Chemie-International Edition 41*, p. 2405 (2002)

[14] H. J. Richter, "The transition from longitudinal to perpendicular recording", *Journal of Physics D-Applied Physics 40*, p. R149 (2007)

[15] Y. Kamata, A. Kikitsu, H. Hieda, M. Sakurai, K. Naito, J. M. Bai, S. Ishio, "Microscopic magnetic characteristics of CoCrPt-patterned media made by artificially aligned self-organized mask", *Japanese Journal of Applied Physics Part 1-Regular Papers Brief Communications & Review Papers 46*, p. 999 (2007)

[16] L. Leibler, "Theory of Microphase Separation in Block Co-Polymers", *Macromolecules 13*, p. 1602 (1980)

[17] T. Jhaveri, V. Rovner, L. Pileggi, A. J. Strojwas, D. Motiani, V. Kheterpal, K. Y. Tong, T. Hersan, D. Pandini, "Maximization of layout printability/manufacturability by extreme layout regularity", *Journal of Micro-Nanolithography Mems and Moems 6*, p. 031011 (2007)

Publications

[1] J. K. W. Yang*, **Y. S. Jung***, J. B. Chang, C. A. Ross, K. K. Berggren, "Programmable Self-assembly of Complex Nanopatterns", (2009, in preparation) *: Contributed equally

[2] **Y. S. Jung**, E. Verploegen, J. B. Chang, P. T. Hammond, K. K. Berggren, C. A. Ross, "Perfectly Ordered Sub-10 nm Stripes from Self-assembly", (2009, in preparation)

[3] **Y. S. Jung**, C. A. Ross, "Well-ordered thin film nanopore arrays formed using a block copolymer template", ***Small*** (2009, in press)

[4] **Y. S. Jung**, C. A. Ross, "Solvent vapor induced tunability of self-assembled block copolymer patterns", ***Advanced Materials*** (2009, in press)

[5] Y. J. Oh, C. A. Ross, **Y. S. Jung**, Y. Wang, C. V. Thompson, "Cobalt Nanoparticle Arrays made by Templated Solid-State Dewetting", ***Small*** *5*, p.860 (2009)

[6] E. Verploegen, T. Zhang, **Y. S. Jung**, C. Ross, P. T. Hammond, "Controlling the Morphology of Side Chain Liquid Crystalline Block Copolymer Thin Films through Variations in Liquid Crystalline Content", ***Nano Letters*** *8*, p. 3434 (2008)

[7] C. A. Ross, **Y. S. Jung**, V. P. Chuang, F. Ilievski, J. K. W. Yang, I. Bita, E. L. Thomas, H. I. Smith, K. K. Berggren, G. J. Vancso, J. Y. Cheng, "Si-containing block copolymers for self-assembled nanolithography", ***Journal of Vacuum Science & Technology B*** *26*, p. 2489 (2008)

[8] **Y. S. Jung***, W. Jung*, H. L. Tuller, C. A. Ross, "Nanowire Conductive Polymer Gas Sensor Patterned Using Self-Assembled Block Copolymer Lithography", ***Nano Letters*** *8*, p. 3776 (2008) *: Contributed equally

[9] **Y. S. Jung**, W. Jung, C. A. Ross, "Nanofabricated concentric ring structures by templated self-assembly of a diblock copolymer", ***Nano Letters*** *8*, p. 2975 (2008)

[10] I. Bita*, J. K. W. Yang*, **Y. S. Jung***, C. A. Ross, E. L. Thomas, K. K. Berggren, "Graphoepitaxy of self-assembled block copolymers on two-dimensional periodic patterned templates", ***Science*** *321*, p. 939 (2008) *: Contributed equally

[11] **Y. S. Jung**, C. A. Ross, "Orientation-controlled self-assembled nanolithography using a polystyrene-polydimethylsiloxane block copolymer", ***Nano Letters*** *7*, p. 2046 (2007)

[12] H. C. Park, D. Byun, B. Angadi, D. H. Park, W. K. Choi, J. W. Choi, **Y. S. Jung**, "Photoluminescence of Ga-doped ZnO film grown on c-Al2O3 (0001) by plasma-assisted molecular beam epitaxy", ***Journal of Applied Physics*** *102*, p. 073114 (2007)

[13] J. Y. Park, **Y. S. Jung**, J. Cho, W. K. Choi, "Chemical reaction of sputtered Cu film with PI modified by low energy reactive atomic beam", *Applied Surface* ***Science*** *252*, p. 5877 (2006)

[14] Y. S. No, O. Kononenko, **Y. S. Jung**, W. K. Choi, T. W. Kima, "Enhancement of the surface and structural properties of ZnO epitaxial films grown on Al2O3 substrates utilizing annealed ZnO buffer layers", ***Journal of Electroceramics*** *17*, p. 283 (2006)

[15] Y. S. No, T. W. Kim, **Y. S. Jung**, W. K. Choi, "Dependences of the surface and the optical properties on the O-2/O-2+Ar flow-rate ratios for ZnO thin films grown on ZnO buffer layers", ***Applied Surface Science*** *252*, p. 8121 (2006)

[16] **Y. S. Jung**, O. V. Kononenko, W. K. Choi, "Electron transport in high quality undoped ZnO film grown by plasma-assisted molecular beam epitaxy", ***Solid State Communications*** *137*, p. 474 (2006)

[17] **Y. S. Jung**, W. K. Choi, O. V. Kononenko, G. N. Panin, "Luminescence of bound excitons in epitaxial ZnO thin films grown by plasma-assisted molecular beam epitaxy", ***Journal of Applied Physics*** *99*, p. 013502 (2006)

[18] B. Angadi, **Y. S. Jung**, W. K. Choi, R. Kumar, K. Jeong, S. W. Shin, J. H. Lee, J. H. Song, M. W. Khan, J. P. Srivastava, "Ferromagnetism in 200-MeV Ag^{+15}-ion-irradiated Co-implanted ZnO thin films", ***Applied Physics Letters*** *88*, p.142502 (2006)

[19] H. W. Suh, G. Y. Kim, **Y. S. Jung**, W. K. Choi, D. Byun, "Growth and properties of ZnO nanoblade and nanoflower prepared by ultrasonic pyrolysis", ***Journal of Applied Physics*** *97*, p. 044305 (2005)

[20] J. Y. Park, **Y. S. Jung**, Y. A. Ermakov, W. K. Choi, "A stationary plasma thruster for modification of polymer and ceramic surfaces", ***Nuclear Instruments & Methods in Physics Research Section B-Beam Interactions with Materials and Atoms*** *239*, p. 440 (2005)

[21] **Y. S. Jung**, O. Kononenko, J. S. Kim, W. K. Choi, "Two-dimensional growth of ZnO epitaxial films on c-Al2O3(0001) substrates with optimized growth temperature and low-temperature buffer layer by plasma-assisted molecular beam epitaxy", ***Journal of Crystal Growth*** *274*, p. 418 (2005)

[22] **Y. S. Jung**, Y. S. No, J. S. Kim, W. K. Choi, "The effect of ZnO homo-buffer layer on ZnO thin films grown on c-Al2O3(0001) by plasma assisted molecular beam epitaxy", ***Journal of Crystal Growth*** *267*, p. 85 (2004)

[23] **Y. S. Jung**, D. W. Lee, D. Y. Jeon, "Influence of dc magnetron sputtering parameters on surface morphology of indium tin oxide thin films", ***Applied Surface Science*** *221*, p. 136 (2004)

[24] **Y. S. Jung**, "Study on texture evolution and properties of silver thin films prepared by sputtering deposition", ***Applied Surface Science*** *221*, p. 281 (2004)

[25] **Y. S. Jung**, "A spectroscopic ellipsometry study on the variation of the optical constants of tin-doped indium oxide thin films during crystallization", ***Solid State Communications*** *129*, p. 491 (2004)

[26] **Y. S. Jung**, "Spectroscopic ellipsometry studies on the optical constants of indium tin oxide films deposited under various sputtering conditions", ***Thin Solid Films*** *467*, p. 36 (2004)

[27] **Y. S. Jung**, H. Y. Seo, D. W. Lee, D. Y. Jeon, "Influence of DC magnetron sputtering parameters on the properties of amorphous indium zinc oxide thin film", ***Thin Solid Films*** *445*, p. 63 (2003)

[28] **Y. S. Jung**, S. S. Lee, "Development of indium tin oxide film texture during DC magnetron sputtering deposition", ***Journal of Crystal Growth*** *259*, p. 343 (2003)

[29] **Y. S. Jung**, Y. W. Choi, H. C. Lee, D. W. Lee, "Effects of thermal treatment on the electrical and optical properties of silver-based indium tin oxide/metal/indium tin oxide structures", ***Thin Solid Films*** *440*, p. 278 (2003)

[30] **Y. S. Jung**, D. Y. Jeon, "Surface structure and field emission property of carbon nanotubes grown by radio-frequency plasma-enhanced chemical vapor deposition", ***Applied Surface Science*** *193*, p. PII S0169 (2002)